COMPRESSIVE IMAGING AND DUAL MOIRÉ LASER INTERFEROMETER AS METROLOGY TOOLS

by

Mehrdad Abolbashari

A dissertation submitted to the faculty of
The University of North Carolina at Charlotte
in partial fulfillment of the requirements
for the degree of Doctor of Philosophy in
Optical Science and Engineering

Charlotte

2013

Approved by:

_____
Dr. Faramarz Farahi

_____
Dr. Angela D. Davies

_____
Dr. Michael A. Fiddy

_____
Dr. Awad S. Gerges

_____
Dr. Robert J. Hocken

_____
Dr. Jonathan Bird

ABSTRACT

MEHRDAD ABOLBASHARI. Compressive imaging and dual moiré laser interferometer as metrology tools. (Under the direction of DR. FARAMARZ FARAHI)

Metrology is the science of measurement and deals with measuring different physical aspects of objects. In this research the focus has been on two basic problems that metrologists encounter. The first problem is the trade-off between the range of measurement and the corresponding resolution; measurement of physical parameters of a large object or scene accompanies by losing detailed information about small regions of the object. Indeed, instruments and techniques that perform coarse measurements are different from those that make fine measurements. This problem persists in the field of surface metrology, which deals with accurate measurement and detailed analysis of surfaces. For example, laser interferometry is used for fine measurement (in nanometer scale) while to measure the form of in object, which lies in the field of coarse measurement, a different technique like moiré technique is used. We introduced a new technique to combine measurement from instruments with better resolution and smaller measurement range with those with coarser resolution and larger measurement range. We first measure the form of the object with coarse measurement techniques and then make some fine measurement for features in regions of interest. The second problem is the measurement conditions that lead to difficulties in measurement. These conditions include low light condition, large range of intensity variation, hyperspectral measurement, etc. Under low light condition there is not enough light for detector to detect light from object, which results in poor measurements. Large range of intensity variation results in a measurement with some saturated regions on the camera as well as

some dark regions. We use compressive sampling based imaging systems to address these problems. Single pixel compressive imaging uses a single detector instead of array of detectors and reconstructs a complete image after several measurements. In this research we examined compressive imaging for different applications including low light imaging, high dynamic range imaging and hyperspectral imaging.

TABLE OF CONTENTS

CHAPTER 1: INTRODUCTION 1

CHAPTER 2: MOIRÉ TECHNIQUE AND LASER INTERFEROMTRY 8

2.1. Moiré Technique 8

2.1.1. Moiré Formation 8

2.1.2. Moiré Methods 11

2.1.2.1. Shadow Moiré 12

2.1.2.2. Projection Moiré 12

2.1.2.4. Fringe Projection 14

2.2. Interferometry 17

2.2.1. Interference 18

2.2.2. Coherence 22

2.2.3. Interferometers 23

2.2.3.1. Michelson Interferometer 23

2.2.3.2. Rayleigh Interferometer 25

2.2.3.3. Mach-Zehnder Interferometer 26

2.2.3.4. Sagnac Interferometer 26

2.2.3.5. Fiber Interferometer 27

2.3. Fringe Pattern Analysis 28

2.3.1. Intensity Methods 29

2.3.2. Phase Measuring Methods 30

2.3.3. Phase Unwrapping 31

CHAPTER 3: DUAL MOIRÉ LASER INTERFEROMETER 36

3.1. System Design 36

3.2. Simulation 57
3.3. Data Stitching 60
3.3.1. Image Registration 61
3.3.2. Data Stitching Algorithm 66
3.4. Fringe Pattern Analysis Software 69
3.5. Experiment 73
3.6. Uncertainty Analysis 92
3.5.1. Lateral Resolution 93
3.7. Conclusion 94
CHAPTER 4: COMPRESSIVE SAMPLING AND COMPRESSIVE IMAGING 96
4.1. Compressive Sampling 97
4.1.1. Sampling 98
4.1.2. Sparsity 99
4.1.3. Incoherence 102
4.1.4. Signal Recovery 103
4.1.5. Some Theorems of Compressive Sampling 105
4.1.6. Measurement Matrix 107
4.2. Compressive Imaging 109
CHAPTER 5: COMPRESSIVE IMAGING SYSTEMS 117
5.1. Low Light Compressive Imaging 117
5.1.1. Experiment 119
5.1.2. Results 121
5.2. Transmissive Compressive Imaging 123
5.2.1. Experiment 124
5.2.2. Results 125

5.3. High Dynamic Range Compressive Imaging 127
5.3.1. High Dynamic Range Imaging 127
5.3.2. High Dynamic Range Compressive Imaging (HDRCI): First Method 135
5.3.2.1. Experiment and Results 140
5.3.3. High Dynamic Range Compressive Imaging: Second Method 144
5.3.3.1. Experiment and Results 148
5.4. Hyperspectral Compressive Imaging 150
5.4.1. Experiment 153
5.4.2. Results 155
5.5. Conclusion 157
CHAPTER 6: CONCLUSION AND FUTURE WORK 159
REFERENCES 164

LIST OF FIGURES

FIGURE 1: Different formations of moiré patterns from linear gratings. (a) is grating, (b) is a grating which is rotated with respect to the grating (a) with the same period, (c) is the resultant moiré pattern.,(d) is a grating with a period slightly different from the grating (a), and (e) shows the moiré pattern of superposition of gratings (a) and (d). (g) shows the moiré pattern which is the results of superposition of grating (a) and grating (f) with slightly different period and tilted with respect to the grating (a). 9

FIGURE 2: Schematic of moiré techniques. (a): shadow moiré, (b): projection moiré , (c): reflection moiré and (d): fringe projection 13

FIGURE 3: Schematic for fringe projection 16

FIGURE 4: Young experiment 18

FIGURE 5: Visibility of interferogram in terms of the relative intensity of two interfering waves 21

FIGURE 6: Michelson interferometer 24

FIGURE 7: Schematic of Rayleigh interferometer 25

FIGURE 8: Mach-Zehnder interferometer 26

FIGURE 9: Sagnac interferometer 27

FIGURE 10: Schematic of a fiber Michelson interferometer 28

FIGURE 11: Schematic of the dual moiré laser interferometer 37

FIGURE 12: First prototype of dual moiré laser interferometer using a stereoscope microscope 38

FIGURE 13: Fringe pattern of moiré part from first prototype. The area is approximately $1mm^2$ 39

FIGURE 14: The second prototype; the stereoscope was replaced by two zoom lenses in order to decouple the projector arm and the camera arm. 40

FIGURE 15: Test setup for partial fiber – partial free space laser interferometer. F1, F2, F3 and F4 are four ends of fiber coupler/divider 41

FIGURE 16: The schematic of laser interferometer with digital feedback system 42

FIGURE 17: The flowchart of digital feedback software 43

FIGURE 18: Analog circuit for applying voltage to the PZT 44

FIGURE 19: The circuit for acquiring the output of the detector 45

FIGURE 20: The voltage applied to PZT (orange signal) and the detector output (blue signal) when (a): digital feedback is turned off and (b) digital feedback is turned on. 46

FIGURE 21: Interferogram from the laser interferometer 47

FIGURE 22: Adding a rotating ground glass to reduce the spatial coherence of laser beam in which results in speckle reduction 47

FIGURE 23: Interferogram after adding ground glass 48

FIGURE 24: Setup to produce a uniform laser beam in order to decrease the speckle pattern 48

FIGURE 25: Intensity profile of the laser beam using the proposed laser beam delivery system: (a) output of a multimode fiber (b): output of the proposed mode scrambling system when a high frequency random voltage applied to the PZT. 49

FIGURE 26: ZEMAX simulation to minimize the projected pattern of the projector using two lenses: (a) the schematic of the lens system with object (projected pattern) and image (image of projected pattern) and (b): the spot diagram of the optimized system. 50

FIGURE 27: ZEMAX simulation to optimize the resolution of the final image on the camera arm: (a) the schematic of two lenses with object (image of zoom lens) and image (image on the camera) and (b) the spot diagram of optimized system. 50

FIGURE 28: Setup with 3M MPro 110 micro projector 51

FIGURE 29: Interferogram from Solder bump. (a): Moiré interferogram at zoom level 4x and (b): Laser interferogram at zoom level 12x 52

FIGURE 30: Schematic of the dual moiré laser interferometer 53

FIGURE 31: Dual moiré laser interferometer 54

FIGURE 32: Laser interferometer 56

FIGURE 33: The coordinate and geometrical parameters for simulation of dual moiré laser interferometer 57

FIGURE 34: Simulated object at different levels of zoom (a): zoom 1x, (b): zoom 2x, (c):zoom 4x, (d):zoom 8x, (e):zoom 16x, (f):zoom 32x, (g):zoom 64x, (g):zoom 128x, (h):zoom 256x, (i):zoom 512x, (j):zoom 1024x, (k):zoom 2048x and (l):zoom 4096x. 59

FIGURE 35: Simulated object and the resultant interferogram from fringe projection and laser interferometer at different levels of zoom: (a1): object at zoom 4x, (a2): laser interferogram at zoom 4x, (a3): moiré pattern at zoom 4x, (b1): object at zoom 32x, (b2): laser interferogram at zoom 32x, (b3): moiré pattern at zoom 32x, (c1): object at zoom 2048x, (c2): laser interferogram at zoom 2048x, (c3): moiré pattern at zoom 2048x. 60

FIGURE 36: Stitching algorithm 67

FIGURE 37: Results of image registration to determine the shift and scale in both x and y directions at different levels of zoom. Images (a) and (b) are simulated moiré fringe patterns from the fringe projection moiré system at zoom levels of 2 and 1, and without any shift of the center of the images. Image (c) is the scaled and translated version of (a) and it is located with respect to the coordinate system of image (b). 67

FIGURE 38: Results of image registration to determine the shift and scale in both x and y directions at different levels of zoom. Images (a) and (b) are simulated laser interferograms from the laser interferometer system at zoom levels of 512 and 256, and without any shift of the center of the images. Image (c) is the scaled and translated version of (a) and it is located with respect to the coordinate system of image (b). 69

FIGURE 39: Inputs and outputs of the fringe analysis. (a): interferogram, (b): Hanning filter in which the central frequency is the same as the carrier frequency of the interferogram, (c): wrapped phase map, (d): unwrapped phase map, (e): unwrapped phase with removed tilt, and (f): the normalized profile of the object 71

FIGURE 40: Fringe analysis software 72

FIGURE 41: Fringe analysis for moiré and laser interferograms. (a): laser interferogram for a microlens (b): corresponding reference interferogram, (c): calculated profile by fringe analysis software, (d): moiré interferogram from a bump artifact, and (e): calculated profile by fringe analysis software. 73

FIGURE 42: The change of intensity for a typical pixel of the captured fringe pattern in terms of the flat object displacement. 74

FIGURE 43: Equivalent wavelength map for moiré system at zoom level one for both projector arm and camera arm. 75

FIGURE 44: Bump artifact as the object 76

FIGURE 45: Deformed and reference fringe patterns from a bump artifact. The first row shows the deformed fringe patterns from a bump artifact at zoom levels of 1x, 1.5x, 2x, 2.5x and 3x. The second row is the reference fringe patterns at the corresponding zoom levels. The third row is the profile of the artifact at the corresponding zoom levels. 77

FIGURE 46: Finding the location of fringe pattern at zoom level 2x (a) with respect to fringe pattern with zoom level 1x (b). (c) shows the scaled and transferred fringe pattern at zoom level 2x at the coordinate of fringe pattern with zoom level 1x. 78

FIGURE 47: Finding the location of fringe pattern at zoom level 3x (a) with respect to fringe pattern with zoom level 2x (b). (c) shows the scaled and transferred fringe pattern at zoom level 3x at the coordinate of fringe pattern with zoom level 2x. 79

FIGURE 48: Moiré fringe patterns from a solder bump flip chip at zoom levels (a): 1x, (b): 1.5x, (c): 2.5x and (d): 3.5x 81

FIGURE 49: Finding the location of fringe pattern with zoom level 3.5x (g) with respect to fringe pattern with zoom level 1x (b). This is done in three steps. First the fringe pattern with zoom level 1.5x (a) is located in the coordinate of the fringe pattern with zoom level 1x (b). (c) shows the scaled and transferred fringe pattern with zoom level 1.5x at the coordinate of fringe pattern with zoom level 1x. The same is performed for moiré fringe patterns with zoom levels 2.5x (d) and 1.5x (e) pair and moiré fringe pattern with zoom levels 3.5x (g) and 2.5x (h). (f) shows the scaled and transferred fringe pattern with zoom level 2.5x at the coordinate of fringe pattern with zoom level 1.5x and (i) shows the scaled and transferred fringe pattern with zoom level 3.5x at the coordinate of fringe pattern with zoom level 2.5x. 82

FIGURE 50: (a): Moiré fringe patterns at zoom levels 1x to 48x. (b): laser interferograms at zoom levels 1x to 48x. 84

FIGURE 51: Results of image registration for moiré and laser interferograms. At each image, the first image is the image in the higher zoom level, the second image is the in eat lower zoom level, and the third image is the scale and shifted image at higher zoom level in the coordinate of the image with lower zoom level. The parameters for each registration are given in Table 10. (a): moiré interferograms at zoom levels 1x and 2x. (b): moiré interferograms at zoom levels 2x and 4x. (c): moiré interferograms at zoom levels 4x and 8x. (d): laser interferograms at zoom levels 8x and 16x. (e): laser interferograms at zoom levels 16x and 24x. (f): laser interferograms at zoom levels 24x and 48x. 85

FIGURE 52: Stitched image of moiré and laser interferograms at the coordinate of the image at zoom level 1x. 86

FIGURE 53: The unwrapped phase of laser interferogram at zoom level 24x with different parameters. The rows show the unwrapped phase with different window size (5, 10, 15, 20 and 25 pixels) of short time Fourier transform and the columns show the unwrapped phase from wrapped phase map with different noise with different DC noise reduction (using high pass filter with cutoff frequency of 6, 12, 18, 24 and 30). 88

FIGURE 54: Result of phase unwrapping for the laser interferogram at zoom level 24x with IntelliWave 88

FIGURE 55: The object: a mirror surface covered with paper tape, except for a small aperture. 89

FIGURE 56: Interferograms from a mirror surface covered with paper tape except for an aperture. (a): Moiré fringe patterns at zoom levels 1x, 1.5x, 2x and 3x. (b): laser interferograms at zoom levels 2x, 3x, 4x, 6x, 8x, 10x, 12x and 13x 90

FIGURE 57: Results of image registration for moiré and laser interferograms. At each image, the first image is the image in the higher zoom level, the second image is the in eat lower zoom level, and the third image is the scale and shifted image at higher zoom level in the coordinate of the image with lower zoom level. (a) Moiré interferograms at zoom levels 1x and 1.5x. (b) moiré interferograms at zoom levels 1.5x and 2x, (c) moiré interferograms at zoom levels 2x and 3x, (d) laser interferograms at zoom levels 3x and 6x, (e) laser interferograms at zoom levels 6x and 12x, and (f) laser interferograms at zoom levels 12x and 13x. 91

FIGURE 58: Profile of object in Figure 55 at different zoom levels 92

FIGURE 59: Image compression using wavelet packet. The original images (a) and (c) were compressed using wavelet packet tree at level 5 and Symlet wavelet of order 8. (b) is the compressed image of (a) when 99% of wavelet coefficients are set to zero; the compressed image preserves about 99% of energy. (d) is the compressed image of (c) when 96% of wavelet coefficients are set to zero; the remaining coefficients keep 99.86% of original image energy. (e) is the compressed image of (c) when 99.43% of coefficients are set to zero; the nonzero coefficients retain 99.43% of original image energy. 101

FIGURE 60: Compressive imaging hardware setup introduced by Wakin et.al. [156]. 110

FIGURE 61: The results of compressive imaging system depicted in Figure 60 [156]. 111

FIGURE 62: The reconstructed image using scrambled Fourier ensemble (SFE) and scrambled block Hadamard ensemble (SBHE) using block size of 32 [131]: (a): The reconstructed boat image of size 512x512 compressively sampled using SFE. (b): The reconstructed boat image of size 512x512 compressively sampled using SBHE. (c): The reconstructed Man image of size 1024x1024 compressively sampled using SFE. (a): The reconstructed Man image of size 1024x1024 compressively sampled using SBHE. 112

FIGURE 63: The results of compressive imaging using mixed Hadamard codes and TV minimization for boats image of resolution 1024x1024 [159]: (a): sample rate: 10%, noise: 10%,PSNR: 25dB. (b): sample rate: 6%, noise: 10%,PSNR: 23dB. 113

FIGURE 64: Reconstruction of image of a man (1024x1024): (a):original image approximated with 25,000 Haar wavelet coefficient; (b): reconstruction from 430x430 sample (PSNR =244 dB) and (c): reconstruction from 350x350 samples (PSNR =27 dB) [160] 114

FIGURE 65: (a): Virtual Bayer Filter structure on the DMD; (b): color CS camera structure [161]. 114

FIGURE 66: Block diagram of the separable-transform imager chip [163]. 115

FIGURE 67: Reconstruction results with different compression ratio and bases for the separable-transform imager chip [163]. 116

FIGURE 68: Setup for low light level compressive imaging 121

FIGURE 69: Results of low light compressive imaging 123

FIGURE 70: Schematic of a transmissive compressive imaging system 124

FIGURE 71: Transmissive compressive imaging system 125

FIGURE 72: Object is a printed “on” letters. The region inside the box is the part that is sampled and reconstructed using transmissive compressive imaging system. 126

FIGURE 73: Reconstruction of image with the resolusion of 64×64 pixels with (a): compression ratio of 4 ($64 \times 644 = 1024$ samples) and PSNR = 20.27 dB, (b): compression ratio of 2 ($64 \times 6424 = 2048$ samples) and PSNR = 22.63 dB, (c): compression ratio of 1.33 ($64 \times 64 \times 34 = 3072$ samples)) and PSNR = 32.44 dB, and (d): compression ratio of 1 ($64 \times 64 = 4096$ samples). All PSNR are calculated with respect to (d). 126

FIGURE 74: High dynamic range imaging technique; (a): Images taken at different exposure time and (b): Composite image [169]. 129

FIGURE 75: HDR imaging system developed by Yamada et.al. [170]. (a): Block diagram of developed vision sensor system, (b): image of tunnel exit taken with a conventional camera and (c): the same scene taken with the developed HDR imaging system. 130

FIGURE 76: images taken from a church with different exposure time (from 1 ms to 30 sec.) [164]. 131

FIGURE 77: Response curve calculated for the imaging system that has taken images in Figure 76; (a): red channel response curve, (b): green channel response curve, (b): blue channel response curve, (b): all three curves in a single diagram [164]. 131

FIGURE 78: (a): Photograph taken with conventional camera and (b): Tone mapped high dynamic range image [164]. 132

FIGURE 79: Results of spatially varying pixel exposure imaging system: (a)-(d) are images taken at exposure time 1T, 4T, 16T and 64T, correspondingly; (e): image taken with spatially varying pixel exposure imaging system and (f): computed image from image taken with spatially varying pixel exposure imaging system [166]. 133

FIGURE 80: Results of HDR imaging system using LCoS proposed by Mannami [173]; (a): Schematic of the proposed imaging system, (b): image before controlling the radiance of light and (c): image after controlling the radiance using LCoS. 134

FIGURE 81: HDR imaging system using DMD; (a): Schematic of the HDR imaging system, (b): First captured image shows saturation in regions 1-4. (c): After adjusting the DMD, the image shows that the saturation in region 1 is no longer exist, but still there is saturation in regions 2-4. (d): captured image after second adjustment with saturations in region 4. (e): Fourth captured image with saturation in region 4 removed and (f): The last captured image [174]. 134

FIGURE 82: Schematic of HDRCI system as (a) block diagram (b) transmissive and (c) reflective configurations. 136

FIGURE 83: Flowchart of high dynamic range compressive imaging algorithm 138

FIGURE 84: Experimental setup for HDRCI: first method 140

FIGURE 85: Images acquired with different exposure times demonstrating the difficulty of simultaneously acquiring both halves of the image in a perceptible manner. (a) Left half with black characters on a dark gray background, and (b) right half with black characters on a white background. 141

FIGURE 86: Results of HDRCI: (a) first reconstructed image; (b) second reconstructed image after applying the algorithm. 142

FIGURE 87: The HDR image obtained by the proposed algorithm : (a) final image (second reconstructed image); (b) mask; (c) HDR image; both bright and dark regions are visible in HDR image. 143

FIGURE 88: Normalized projected intensity captured by the detector versus the image with pixel values varies from 1 to 255. 144

FIGURE 89: Flowchart of high dynamic range compressive imaging (HDRCI) procedure 146

FIGURE 90: Schematic of the high dynamic range compressive imaging 147

FIGURE 91: Experimental setup for high dynamic range compressive imaging 147

FIGURE 92: Image of the object with (a) low exposure time and (b) high exposure time 148

FIGURE 93: HDRCI results (a): reconstructed image without any mask. (b): second reconstructed image with a mask on top of the image and increased equivalent exposure time. (c): final image by combining images (a) and (b) 149

FIGURE 94: Schematic of dual disperser single shot compressive spectral imager [183] 151

FIGURE 95: Schematic of single disperser snapshot compressive spectral imager [184] 151

FIGURE 96: Results of spectral compressive imaging with the of single disperser snapshot compressive spectral imager (a): scene consisting of a Ping-Pong ball illuminated by a 543 nm green laser and a white light source filtered by a 560 nm narrowband filter; and a red Ping-Pong ball illuminated by a white light source and (b): Spectral images at 28 channels between 540 nm and 640 nm. The green ball appears in the channels with lower wavelengths (3-8) while the red ball appears in the channels with higher wavelengths (23-25) Wagadarikar, John, Willett, & Brady, 2008). 152

FIGURE 97: Results of hyperspectral compressive imager; (a): object and (b): spectral images at wavelength range of 445-640nm. 153

FIGURE 98: Schematic of Hyperspectral compressive imaging 154

FIGURE 99: Spectral compressive imaging system. The light source of Infocus LP120 projector was removed and the spectrometer is placed in front of light source. The light enters the spectrometer through a tapered glass, objective lens and an optical fiber. 154

FIGURE 100: Hyperspectral compressive imaging system with 10x objective lens. 155

FIGURE 101: Spectral images of a at wavelength (a): 632.80nm and (b): 632.79nm 156

FIGURE 102: Spectrum of a red HeNe laser (632.8 nm) from the spectrometer (red line) and reconstructed from data cube (black line) 156

FIGURE 103: Hyperspecral compressive imaging of 15 red LEDs with cental wavelength of 628.1 nm and bandwidth of 20 nm. The spatial resolution is 512x512. (a): The scene taken with a conventional camera, (b): the reconstructed spectral image with the compression ratio of 80% and (c): the reconstructed spectral image with the compression ratio of 60% both at 628.10 nm. 157

LIST OF TABLES

TABLE 1: Specification of VZM 450 Zoom Imaging lens 55

TABLE 2: Specification of 1x compact telecentric lens 55

TABLE 3: Specification of 5X Mitutoyo Plan Apo Infinity-Corrected Long WD objective 56

TABLE 4: Specification of 12.5x Precision Zoom Lens 56

TABLE 5: Scale (change of zoom level in X and Y directions) and translation (shift in X and Y directions) values for moiré fringe patterns at zoom levels 1x and 2x (Figure 37). 68

TABLE 6: Scale (change of zoom level in X and Y directions) and translation (shift in X and Y directions) values for laser interferograms at zoom levels 1x and 2x (Figure 38) 69

TABLE 7: Scale (change of zoom level in X and Y directions) and translation (shift in X and Y directions) values for fringe patterns at zoom levels 1x and 2x (Figure 46). 78

TABLE 8: Scale (change of zoom level in X and Y directions) and translation (shift in X and Y directions) values for fringe patterns at zoom levels 1x and 2x (Figure 47). 79

TABLE 9: Scale (change of zoom level in X and Y directions) and translation (shift in X and Y directions) values for moiré fringe patterns for a solder bump flip chip (Figure 49). 82

TABLE 10: Results of image registration for moiré interferograms at zoom levels 1x, 2x, 4x, and 8x; and for laser interferograms at zoom levels 8x, 16x, 24x, and 48x. 86

TABLE 11: Results of image registration for moiré interferograms at zoom levels 1x, 1.5x, 2x, and 3x; and for laser interferograms at zoom levels 3x, 6x, 12x, and 13x. 91

TABLE 12: Error percentage at different zoom levels for fringe projection and laser interferometer 93

CHAPTER 1: INTRODUCTION

Scenes in the nature usually have broad range of intensity and also broad range of colors. A camera with the ability to obtain images without saturation and/or underexposed areas is needed to record photograph those scenes with no loss of information. For example, a camera that stores the value of each pixel with sixteen bits gives better range of intensity than a camera in which the value of each pixel stores as an 8-bit data. However cameras with higher bit depth are more expensive and by going to the wider range of intensities we might not find a camera with enough bit depth to truly capture and store the intensity pattern of a particular scene. There are different approaches that can be taken to solve this problem. One solution is using high dynamic range techniques which uses a camera with low bit depth and reconstruct an image with higher bit depth. We explore this approach in chapter 5 where we combine those techniques with compressive imaging technique to benefit from advantages that both methods offer.

Another approach to solve this problem is to divide the scene into smaller regions. It is very probable that in smaller regions the range of intensity is less than the range of the intensity of whole scene. Therefore, we can capture image of each sub-region with a camera with lower bit depth and then combine all sub-regions to construct a complete picture of the scene. We can look at this approach as a trade-off between the bit depth and the area of interest in that scene; with smaller area, the required number of bits to

represent the intensity of the scene is smaller and it gets greater when the area becomes larger. This means that if we fix the number of bits (a camera with a specific number of bits) to represent the scene, we lose the resolution as we make the scene larger and larger. In other words, there is a tradeoff between the area of captured scene and the resolution of intensity pattern. This tradeoff can be generalized as a tradeoff between the range of measurement and the corresponding resolution which is intrinsic in many situations.

As another example, assume that in the same scenario we want to capture the spectral content of the scene. Considering our spectrometer has an array of 1000 detectors, the resolution of the acquired spectrum depends on the range of spectrum we are interested. This means that if the range of interest is visible part of the spectrum, about 400 nm to 700 nm, then the resolution will be 0.3 nm; if the range of spectrum expands to cover part of UV and IR spectrum (e.g. 200 nm to 2000 nm) then the resolution will be 1.8 nm. We can see that there is a degradation of the resolution by increasing the range of measurement. On the other hand, if we select only a part of the visible spectrum (e.g. 400 nm to 500 nm), this decrease in range results in an increase in resolution (0.1 nm).

In metrology, which is the science of measurement and deals with measuring different aspects of objects, we encounter with these situations. In this research effort, two problems in the field of metrology are tackled; the first problem is the problems associated with the trade-off between the range of measurement and the corresponding resolution. The second problem that is being addressed in this dissertation is the measurement conditions that lead to difficulties in measurement such as low signal to noise ratio. This will be described in the later part of this chapter.

The trade-off between measurement range and resolution can be between field of view and spatial (lateral) resolution or between the vertical range and vertical resolution. For example, assume the trade-off between the field of view and spatial resolution. These parameters are defined as the following [1].

Field of view: The field of view is the diameter of the circle of illumination on the object. In an instrument without scanning, the measurable lateral area is determined by the field of view.

Spatial Resolution: The spatial resolution determines the minimum distance between two lateral features on a surface that can be distinguished. For a perfect optical system with a filled objective pupil, the resolution is given by the Rayleigh criterion $r = .61\frac{\lambda}{A_N}$ where λ is the wavelength of the incident radiation and A_N is the numerical aperture.

The resolution of system is limited either by the Rayleigh criterion, resolution of optical elements or the number of the pixels of the camera.

For example, suppose that the camera has 1024×1024 pixels and a red HeNe laser is used as the light source. Therefore, with the use of a lens with numerical aperture of 0.3, the Rayleigh criterion results in spatial resolution of $r_1 = 1.29\ \mu m$. Assume that the resolution of lens system is $0.9\mu m$ for field of view of $1mm \times 1mm$, $1.9\mu m$ for field of view of $2mm \times 2mm$ and $4\mu m$ for field of view of $4mm \times 4mm$.

With the field of view of $1mm \times 1mm$, the resolution limited by camera is $r_2 = 1000/1024 = .98\ \mu m$. The resolution of system is limited by Rayleigh criterion which is $r_s = r_1 = 1.29\ \mu m$. If the field of view is $2mm \times 2mm$ then the resolution limited by the camera is $r_2 = 2000/1024 = 1.95\ \mu m$ and the resolution limited by the lens system is $r_3 = 1.9\mu m$. Therefore the resolution of the system is limited by the camera and is

$r_s = r_2 = 1.95\,\mu m$. By changing the field of view to $4mm \times 4mm$, the resolution limited by the camera is $r_2 = 4000/1024 = 3.91\,\mu m$ and the resolution limited by the lens system is $r_3 = 4\mu m$ which results in system resolution of $r_s = r_2 = 4\,\mu m$. As it is seen, the spatial resolution is changed by change in field of view and greater field of view results in worsening spatial resolution.

Similar to trade-off between field of view and lateral resolution, there is a trade-off between the vertical range (maximum measurable height) and the vertical resolution. Assume that within the field of view, the maximum measurable height is ten times of the wavelength. On the other hand, the height resolution is also a ratio of wavelength, say $\frac{\lambda}{20}$. This means that with higher wavelength, the range of the height that can be measured is higher; however the height resolution is lower. Thus there is also a trade-off between the range of the height and vertical resolution that should be taken into consideration.

We introduce a technique that combines the coarse measurement with large field of view and extended vertical range, with fine measurement over a small field of view and shorter vertical range. This combined technique is applicable for the metrology of large objects with small features.

For measuring large objects, different measurements are taken at different locations on the object and stitched together to form one image, which typically requires large overlap regions among the measurements. Information such as height, stress, strain, etc. can be obtained from this large stitched image without discontinuity. In cases where regions of interest (ROI) are small and discrete areas of the object, different strategies might be chosen. One strategy is based on scanning the whole object with the highest resolution followed by processing and stitching the acquired data. In this case, processed

data outside the ROIs are discarded, wasting measurement time and effort. For example, suppose the part to be measured is an array of solder bumps deposited on a chip pad, and the solder bumps have to be carefully inspected. If there is a defect on one of the solder bumps, the location and details of the defect need to be identified. With this strategy, the profiles of all solder bumps have to be acquired with the highest resolution, part by part, and then profiles stitched together from different parts to get one continuous profile. This approach is very time consuming and not efficient.

The other strategy is to take the high resolution measurements only from the ROIs. The difficulty here is that ROIs, have to be identified first and second the relative location of the ROIs with respect to a reference point on the object are unknown, in general (if there is no overlap between ROIs).

To address these issues, a combination of multiscale measurement and stitching is proposed, namely a measurement with low resolution is taken (coarse measurement), ROIs identified, and then measurements with high resolution are taken from the ROIs (fine measurement). The coarse measurement is realized with a moiré technique (fringe projection) and a Michelson interferometer is implemented as the fine measurement instrument. Since we have two different instruments and two different data sets, it requires a strategy for interrelating locations and magnification scales. An algorithm is proposed to offer measurements at different levels of zoom while stitches data at all zoom levels. Stitching means that the exact coordinates of all measurements at different magnifications are established relative to a common reference point.

Chapter 2 starts with a discussion on moiré techniques. Moiré techniques are usually used for form measurement (coarse measurement). Then the principles of interferometry

and interferometers are explained. Laser interferometers are instruments for precision metrology (fine measurement). The outputs of both moiré system and laser interferometer are a fringe patterns distorted by the distribution of the parameter of interest (e.g. surface topography of the object). Fringe analysis extracts the parameter of interest from the distorted fringe patterns. Different methods for fringe analysis are explained at the end of that chapter.

Chapter 3 is the implementation of the dual moiré laser interferometer. The chapter starts with different prototypes that were implemented and the problems and issues that lead from one prototype to another. An algorithm and the required software for stitching the data from moiré system and laser interferometer and also from different levels of the zoom are developed. Image registration, which is the core of the algorithm, is also explored. The results of simulation of the system with MATLAB and optimization of some optical parts of the system with Zemax are presented. The experimental results are shown and an error analysis to evaluate the performance of the system is provided.

The second issue that was addressed in this work is the measurement conditions that lead to difficulties in the measurement. As an example, low light level is one condition that makes the measurement noisier. One way to resolve this problem is to increase the gain of the detector to amplify the signal, although increasing the gain of detector results in the amplification of the noise too, which results in low signal to noise ratio and poor measurements. If we do not increase the gain we deal with measurements that are close or below the noise level of measurement system, which again results in poor measurements.

Another example of such conditions is the wide range of intensity; the measurement of a signal (one or multi dimensional) with wide range requires a measurement

instrument with the capability of the same or greater range of measurement. For example if an object/scene has the range of the intensity from 1 to 1000 units of intensity[1] (ratio of 1000/1=1000), the instrument that measures/images the object has to have the dynamic range of at least 1000. An instrument with lower dynamic range results in a measurement with some saturated measurements/pixels and/or some noise like measurement/pixels.

Our approach to these problems is using compressive sampling. Compressive sampling is a new approach that has been finding applications in many areas including communication, imaging, coding, etc. One branch of compressive sampling is compressive imaging. Compressive imaging uses a single detector instead of array of detectors and reconstructs a complete image after several measurements. Using single detector instead of an array of detectors has several benefits including higher signal to noise ratio and capability of imaging in wavelength ranges that there is no camera or array detector; but single detectors are available.

In this field we examined compressive imaging for different situations including low light imaging, high dynamic range imaging and hyperspectral imaging.

Chapter 4 includes some basic concepts of compressive sampling and a review of different compressive imaging systems.

Chapter 5 is devoted to demonstration of different compressive imaging systems implemented. This includes low light compressive imaging, different high dynamic range compressive imaging and hyperspectral compressive imaging.

The work is concluded in the last chapter and some suggestions for the future work on the path to further improve the measurements in the field of the metrology are provided.

[1] What is important in high dynamic range measurement is the ratio of the maximum to the minimum of the measurand and therefore the absolute value of the maximum and minimum are not essential.

CHAPTER 2: MOIRÉ TECHNIQUE AND LASER INTERFEROMTRY

Moiré and laser interferometry are metrology techniques that can be used to measure form and features of an object, respectively. Moiré techniques are based on summation or multiplication of light intensity. Moiré systems are used to measure the form of the object and their range of measurement can be relatively large. On the other hand, the laser interferometry methods are based on interference between light fields and usually have relatively high precision accompanies with a small range of measurement. In this chapter the principles and basics of both techniques are explained briefly. More detailed discussion of moiré and laser interferometry can be found in [2], [3], [4], [5], [6]. After a brief description of moiré techniques and laser interferometry, different techniques for fringe pattern analysis, which is the output of moiré systems and laser interferometers, are discussed. The fringe analysis process includes pre-processing (e.g. filtering and smoothing), phase wrapping, and phase unwrapping and post-processing of phase map. The emphasis of the fringe pattern analysis section is on the different phase wrapping and phase unwrapping methods.

2.1. Moiré Technique

2.1.1. Moiré Formation

Moiré is a French word which means “an irregular wavy finish on a fabric; a fabric having a wavy watered appearance; and an independent usually shimmering pattern seen when two geometrically regular patterns (as two sets of parallel lines or two halftone

screens) are superimposed especially at an acute angle" [7]. Moiré patterns in optics can be seen as two gratings are superimposed. The gratings might have slightly different periods (Figure 1.a-c), rotated relative to each other (Figure 1.a,d-e) or have different periods and relative rotation (Figure 1.a,f-g).

Suppose that the grating can be represented by the following Fourier series [4]:

$$f_1(x,y) = a_1 + \sum_{n=1}^{\infty} b_{1n} cos[n\varphi_1(x,y)] \tag{2.1}$$

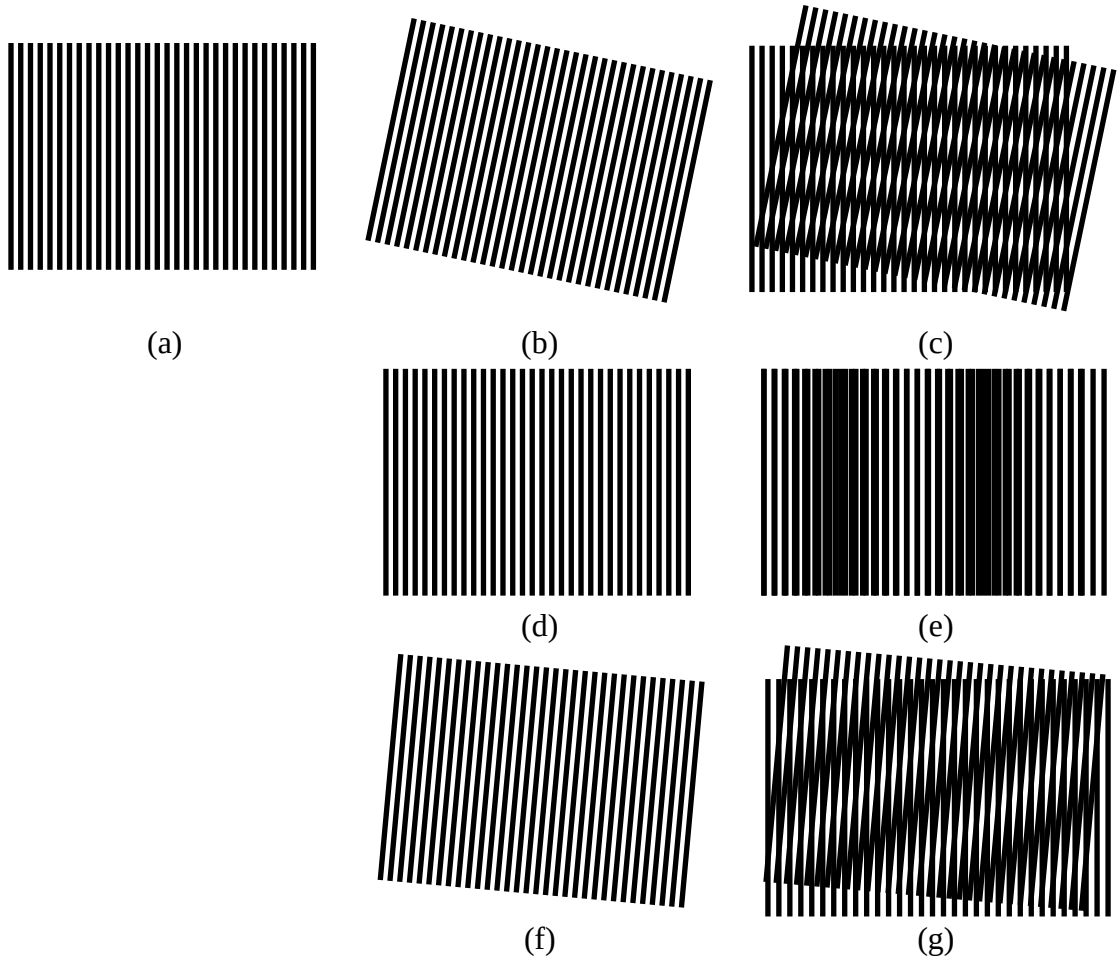

Figure 1: Different formations of moiré patterns from linear gratings. (a) is grating, (b) is a grating which is rotated with respect to the grating (a) with the same period, (c) is the resultant moiré pattern.,(d) is a grating with a period slightly different from the grating (a), and (e) shows the moiré pattern of superposition of gratings (a) and (d). (g) shows the moiré pattern which is the results of superposition of grating (a) and grating (f) with slightly different period and tilted with respect to the grating (a).

$$f_2(x,y) = a_2 + \sum_{m=1}^{\infty} b_{2m} cos[m\varphi_2(x,y)] \tag{2.2}$$

where $\varphi_1(x,y)$ and $\varphi_2(x,y)$ are representative of the basic shape of the gratings. Superposition of these two gratings equals to multiplication of $f_1(x,y)$ and $f_2(x,y)$:

$$\begin{aligned} f_1(x,y)f_2(x,y) \\ &= a_1a_2 + a_1 \sum_{m=1}^{\infty} b_{2m} cos[m\varphi_2(x,y)] \\ &+ a_2 \sum_{n=1}^{\infty} b_{1n} cos[n\varphi_1(x,y)] \\ &+ \sum_{m=1}^{\infty}\sum_{n=1}^{\infty} b_{1n}b_{2m} cos[n\varphi_1(x,y)]cos[m\varphi_2(x,y)] \end{aligned} \tag{2.3}$$

The last term of this multiplication can be rewritten as

$$\begin{aligned} \sum_{m=1}^{\infty}\sum_{n=1}^{\infty} b_{1n}b_{2m} cos[n\varphi_1(x,y)]cos[m\varphi_2(x,y)] \\ &= \frac{1}{2} b_{11}b_{21} cos[\varphi_1(x,y) - \varphi_2(x,y)] \\ &+ \frac{1}{2}\sum_{m=1}^{\infty}\sum_{n=1}^{\infty} b_{1n}b_{2m} cos[n\varphi_1(x,y) - m\varphi_2(x,y)]; n,m \neq 1 \\ &+ \frac{1}{2}\sum_{m=1}^{\infty}\sum_{n=1}^{\infty} b_{1n}b_{2m} cos[n\varphi_1(x,y) + m\varphi_2(x,y)]; n,m \neq 1 \end{aligned} \tag{2.4}$$

This means that by superimposing two gratings, one can obtain difference and sum of the two gratings (both fundamentals and harmonics). For example, consider two linear gratings with periods λ_1 and λ_2, and the relative rotation of 2α between them. Therefore $\varphi_1(x,y)$ and $\varphi_2(x,y)$ can be written as:

$$\varphi_1(x,y) = \frac{2\pi}{\lambda_1}[xcos(\alpha) + ysin(\alpha)] \tag{2.5}$$

$$\varphi_2(x,y) = \frac{2\pi}{\lambda_2}[xcos(\alpha) - ysin(\alpha)] \tag{2.6}$$

and the difference of $\varphi_1(x,y)$ and $\varphi_2(x,y)$ is:

$$\varphi_1(x,y) - \varphi_2(x,y) = \frac{2\pi}{\lambda_{beat}}xcos(\alpha) + \frac{4\pi}{\bar{\lambda}}ysin(\alpha) \tag{2.7}$$

where $\lambda_{beat} = \frac{\lambda_1\lambda_2}{\lambda_2-\lambda_1}$ and $\bar{\lambda} = \frac{\lambda_1+\lambda_2}{2}$.

The situations that are demonstrated in Figure 1 are equivalent to different λ_i and angle α, namely different periods means $\lambda_1 \neq \lambda_2$ and rotation means $\alpha \neq 0$. When $\lambda_1 \neq \lambda_2$ and $\alpha = 0$, the fringe spacing is λ_{beat} and when $\lambda_1 = \lambda_2$ and $\alpha \neq 0$, the fringe spacing is $\lambda/2sin(\alpha)$.

Moiré patterns can be seen as interference in the sense that each linear grating can be seen as a snapshot of a plane wave (although since gratings are binary they cannot represent the sinusoidal intensity patterns, and sinusoidal patterns can be extracted by filtering the harmonics of binary moiré patterns). When two linear gratings are superimposed, it is equal to interference between two plane waves. Different periods mean different wavelengths and different angle between gratings equals to different direction of propagation. Therefore moiré patterns can be related to interferometry in that sense. Other waves other than plane waves can also be represented by gratings. For example, spherical waves can be represented by circular gratings.

2.1.2. Moiré Methods

Moiré method is an optical technique for form and surface measurement and characterization [3], [4], [8], [9]. It can be used to measure in-plane deformation and

strain [10] as well as out-of-plane deformation and profilometry [11][12]. In-plane measurements are usually performed by attaching a grating to the object and then measuring the deformation of the grating. Out-of-plane measurements are based on illuminating the object by a structured light, which is usually a straight line grating, and measuring the deformation of reflected light from the object. In both cases, the reflected light can be summed or multiplied by another grating to form a moiré fringe pattern or the deformation can be directly measured. There are four main moiré techniques, namely shadow moiré, projection moiré, reflection moiré and fringe projection that are described below.

2.1.2.1. Shadow Moiré

Figure 2.a shows schematic of a shadow moiré. Shadow moiré uses a grating in front of the object. The light passes through the grating and makes the shadow of grating on the object. This shadow is captured from different angle through the grating which produces moiré pattern. The moiré pattern changes wherever the form of the object is not planar. The shadow moiré technique can be used in strain and stress analysis and vibration measurements [13], [14], [15], [16].

2.1.2.2. Projection Moiré

Projection moiré uses two different gratings, instead of one; one in front of the light source and the other one in front of the camera. The profile of the object is calculated from the moiré pattern and the parameters of the projection moiré setup. Figure 2.b shows a projection moiré setup. The projection moiré has the ability to measure larger objects compare to the shadow moiré and also the fringe pattern analysis is easier than the

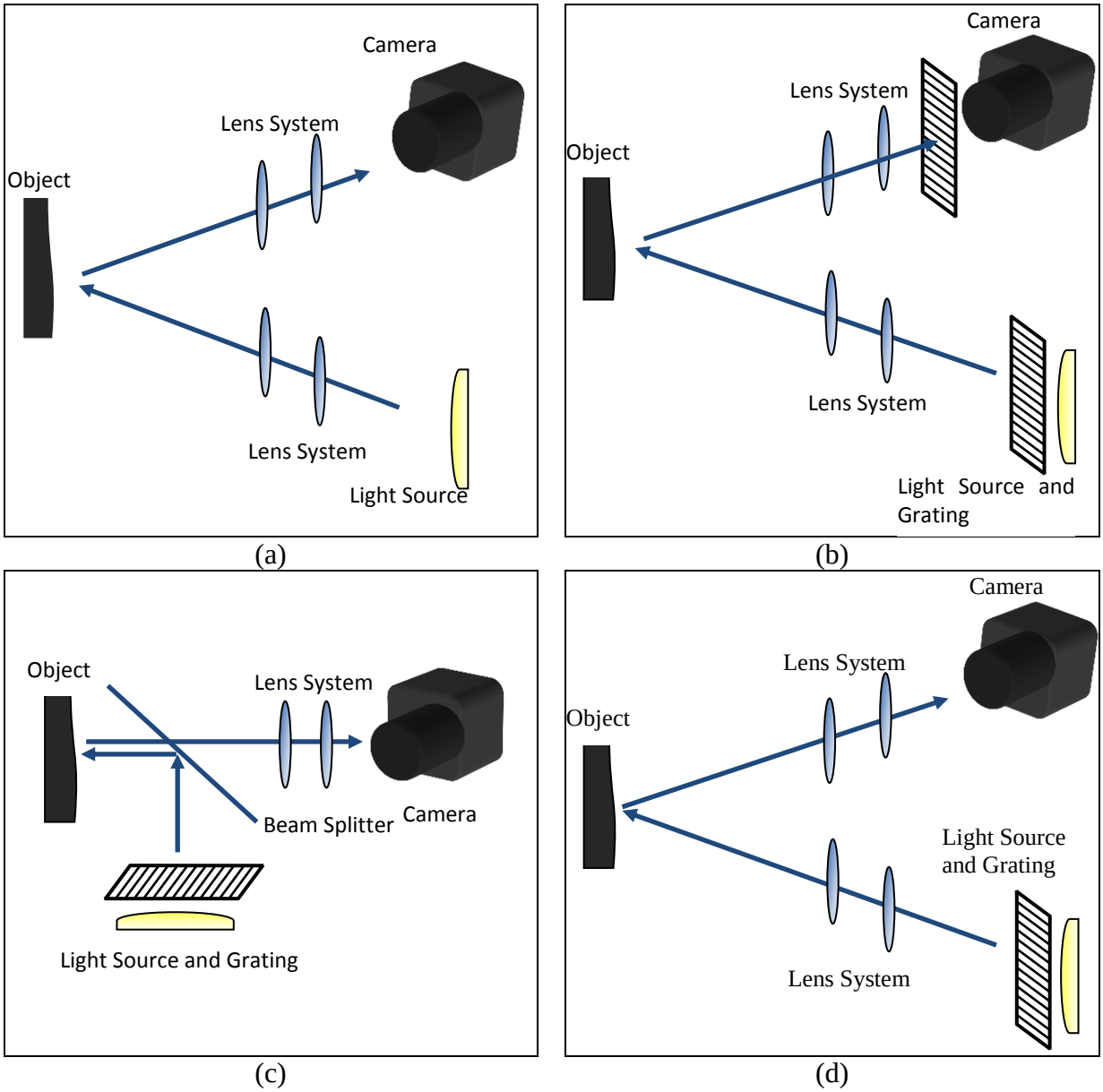

Figure 2: Schematic of moiré techniques. (a): shadow moiré, (b): projection moiré , (c): reflection moiré and (d): fringe projection

shadow moiré. The applications of the projection moiré include strain and vibration analysis, and study of the human body [17], [18], [19], [20], [21].

2.1.2.3. Reflection Moiré

Reflection moiré uses one grating in front of the light source. The structured light reflected back from an object and captured by the camera (Figure 2.c). In contrast to

other moiré methods, the deformation of the structured light (grating) is related to the slope and curvature distribution of the object profile. The limitation of this technique is that the surface of the object under test should be specular. As other moiré methods, the reflection moiré is utilized for surface topography. Specifically the reflection moiré can be used for strain measurement and vibration in plates [22], [23], [24].

2.1.2.4. Fringe Projection

Fringe projection introduced by Rowe and Welford [25]. They used fringe projection technique to measure surface topography. Figure 2.d shows a schematic of this moiré technique.

In the fringe projection, a fringe pattern (parallel lines) is projected onto the object and the projected fringe pattern is captured from another angle. The fringe pattern will be distorted according to the profile of the object. The distance between contours of the acquired fringe pattern depends on the pitch of projected fringe pattern and the parameters of fringe projection setup. By analyzing the acquired fringe pattern and knowing the parameters of the fringe projection setup, the profile of the object is calculated. The fringe projection technique can be used as a fast method to measure the 3D form of the object [26], [27], [28].

Figure 3 shows again the schematic for a fringe projection system where the object is horizontal. The angle between the projection plane and the reference plane is α and the angle between the imaging plane and the reference plane is β. The fringe pattern period on projection plane is λ_1. For a flat surface (reference plane) the period of the captured fringe pattern on imaging plane will be $\lambda_2 = \frac{cos\beta}{cos\alpha}\lambda_1$. Assuming that the projected fringe pattern is a sinusoidal pattern with period of λ_1, then the fringe pattern obtained from a

flat object will be a sinusoidal pattern with period of λ_2. For a non-flat object, the deviation of the object from the reference plane causes shift in the phase of the fringe pattern on the image plane. The phase shift can be expressed in terms of the displacement "d" with the following relationship:

$$\varphi = \frac{2\pi}{\lambda_2} d \tag{2.8}$$

Figure 3 shows the displacement of the captured ray when a flat surface is replaced by a non-flat object.

By finding the relation between d and the corresponding height of the object, h, the relationship between height and the phase of captured fringe pattern will be known. The relation between displacement and the height of the object can be calculated as follows.

In the AOH triangle:

$$\overline{OA} = \frac{\mathrm{h}}{\cos\alpha} \tag{2.9}$$

for the ABO triangle:

$$\frac{\overline{OA}}{\overline{OB}} = \frac{\sin\beta}{\sin(\alpha+\beta)} \tag{2.10}$$

and in the DBO triangle:

$$\mathrm{d} = \sin\beta\,\overline{OB} \tag{2.11}$$

From equations (2.9), (2.10), and (2.11), displacement d is derived in terms of the height of the object as:

$$\begin{aligned} \mathrm{d} = \sin\beta\,\overline{OB} = \sin\beta\frac{\sin(\alpha+\beta)}{\sin\beta}\overline{OA} = \frac{\sin(\alpha+\beta)}{\cos\alpha}\mathrm{h} \\ = (\sin\beta + \cos\beta\tan\alpha)\mathrm{h} \end{aligned} \tag{2.12}$$

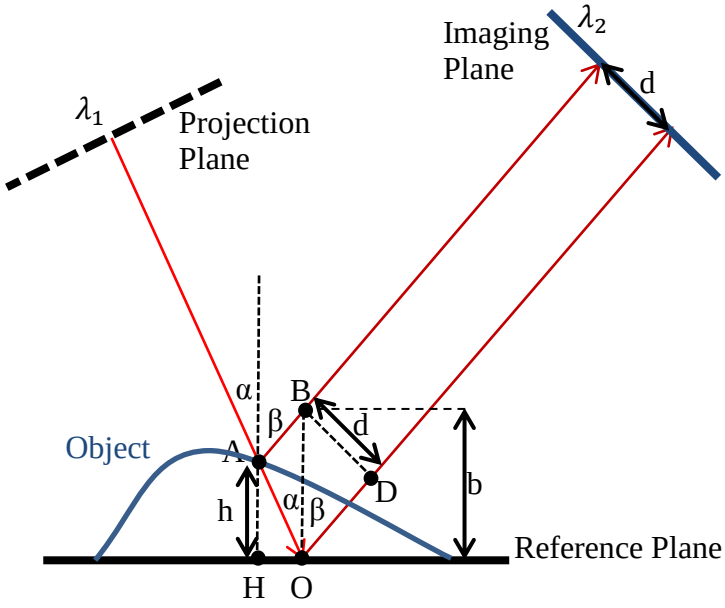

Figure 3: Schematic for fringe projection

Considering equations (2.8) and (2.12), the relation between the phase shift and the height of the object is calculated as:

$$\mathrm{h} = \frac{d}{\sin\beta + \cos\beta\tan\alpha} = \frac{\lambda_2}{2\pi(\sin\beta + \cos\beta\tan\alpha)}\varphi = \frac{\lambda_{eq}}{2\pi}\varphi = \mathrm{k}\varphi \qquad (2.13)$$

where $\lambda_{eq} = \frac{\lambda_2}{(\sin\beta + \cos\beta\tan\alpha)}$ is the equivalent wavelength of the fringe projection system and $k = \frac{\lambda_2}{2\pi(\sin\beta + \cos\beta\tan\alpha)}$ is the coefficient that depends on the period of the fringe pattern and the configuration of the fringe projection system.

If the light is not collimated, the equivalent wavelength and the coefficient both depend on the distance of the projection plane and imaging plane from the reference plane, and the position of each pixel, too. One way to find the equivalent wavelength is by a calibration method using a flat object. This way the equivalent wavelength can be calculated for each pixel. This technique will be explained in the next chapter.

2.2. Interferometry

Interferometry is a technique that employs the interference of two or more light waves. Interferometry technique is used to extract the information carried in a modulated wavefront of a light wave. To do so, the modulated wavefront is superimposed by a light wave that its properties are known. The superimposed wavefronts contain the information in the phase, i.e. the information is modulated as phase modulation. Therefore a phase demodulation technique is used to extract the information.

First experiment to demonstrate the interferometry was Young's double slit that was performed by Thomas Young in 1803 [29]. Figure 4 Figure 4 shows the schematic of Young's double slit experiment. Light waves from a light source, first pass through two holes and interfere on a screen at a distance from holes. The resultant pattern on the screen is a sinusoidal shape of intensity distribution. This work was a breakthrough in the understanding of the nature of light and along with works of Huyghens and Fresnel led to the acceptance of wave nature of light.

The instrument that uses the interferometry technique is called interferometer. Interferometers are used to measure some aspects of object under measurement with high precision. The first work on interferometry was done by Michelson and Morley [30]. They performed this experiment to show the "aether drift" and implemented an interferometer for their experiment. Although, the null result of their experiment led to rejection of concept of aether. The application of interferometry followed after this experiment mainly lied in the field of metrology and spectroscopy. After the invention of laser, the interferometry experienced a rapid growth.

There are different ways to categorize the interferometers. One category is based on the number of light waves (beams) that interfere that can be two or more than two beams. Michelson interferometer is an example of two-beam interferometer and Fabry-Perot interferometer is an example of multi-beam interferometer. Another category of interferometers, divide interferometers into interference by division of amplitude and interference by division of wavefront. Rayleigh interferometer is an example of former while Mach-Zehnder interferometer is an example of the latter one.

In the following, first, a brief mathematical description of basic of interference will be given then some common interferometers will be explained, and lastly, fiber interferometers are described.

2.2.1. Interference

Interference is the superposition of two or more electromagnetic waves providing that the electromagnetic waves have a degree of coherence and the same state of polarization.

Suppose $\boldsymbol{E_1}$ and $\boldsymbol{E_2}$ are two light waves:

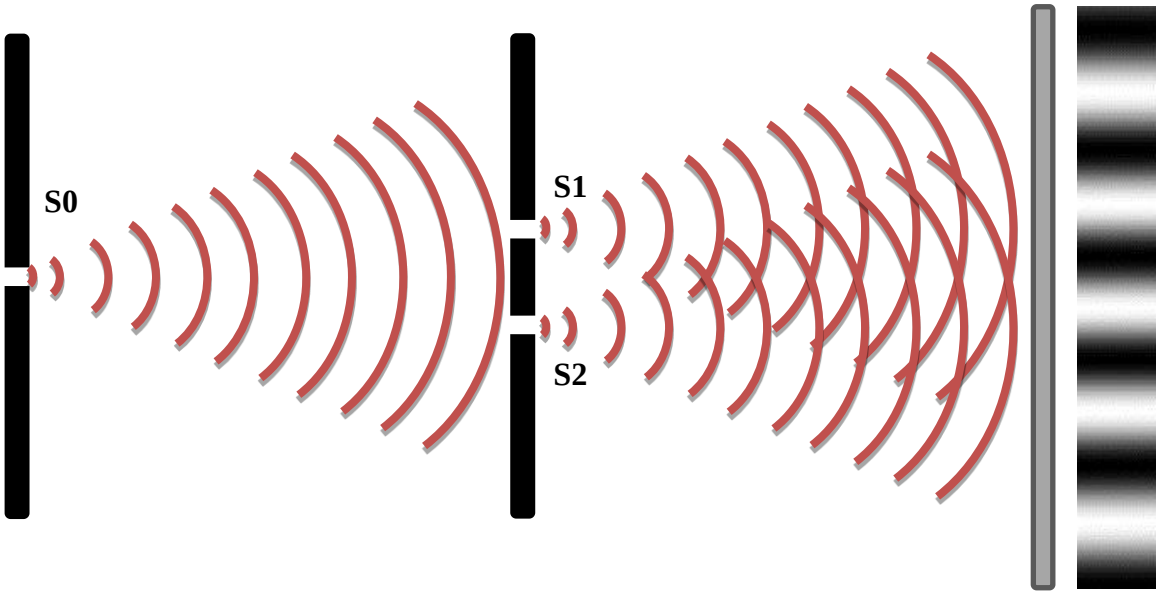

Figure 4: Young experiment

$$\boldsymbol{E_1} = \boldsymbol{E_{01}} cos(\boldsymbol{k_1}.\boldsymbol{r} + w_1 t + \varphi_1) \tag{2.14}$$

$$\boldsymbol{E_2} = \boldsymbol{E_{02}} cos(\boldsymbol{k_2}.\boldsymbol{r} + w_2 t + \varphi_2) \tag{2.15}$$

For simplicity we assumed that light waves are monochromatic and plane waves. Then the interference between these two waves can be expressed as

$$\begin{aligned} I \propto \langle \boldsymbol{E_{total}^2} \rangle_T &= \langle (\boldsymbol{E_1} + \boldsymbol{E_2})^2 \rangle_T \\ &= \langle \boldsymbol{E_1}^2 \rangle_T + \langle \boldsymbol{E_2}^2 \rangle_T \\ &+ \langle 2\boldsymbol{E_1}.\boldsymbol{E_2} cos\big((\boldsymbol{k_1} - \boldsymbol{k_2}).\boldsymbol{r} + (w_1 - w_2)t + (\varphi_1 - \varphi_2)\big) \rangle_T \end{aligned} \tag{2.16}$$

where

$$\langle x(t) \rangle_T = \frac{1}{T} \int_t^{t+T} x(\tau) d\tau \tag{2.17}$$

Assuming that the averaging time T is much greater compare to $1/w_1$ and much smaller than $1/(w_1 - w_2)$, i.e . $1/w_1 \ll T \ll 1/(w_1 - w_2)$, then the intensity can be expressed as:

$$\begin{aligned} I \propto \langle \boldsymbol{E_{total}^2} \rangle_T &= \langle (\boldsymbol{E_1} + \boldsymbol{E_2})^2 \rangle_T \\ &\approx \frac{1}{2} E_{01}^2 + \frac{1}{2} E_{02}^2 \\ &+ \boldsymbol{E_{01}}.\boldsymbol{E_{02}} cos\big((\boldsymbol{k_1} - \boldsymbol{k_2}).\boldsymbol{r} + (w_1 - w_2)t + (\varphi_1 - \varphi_2)\big) \end{aligned} \tag{2.18}$$

Assuming that both light waves have the same state of polarization ($\boldsymbol{E_{01}} || \boldsymbol{E_{02}}$):

$$\begin{aligned} I \propto \langle \boldsymbol{E_{total}^2} \rangle_T &= \langle (\boldsymbol{E_1} + \boldsymbol{E_2})^2 \rangle_T \\ &= \frac{1}{2} E_{01}^2 + \frac{1}{2} E_{02}^2 \\ &+ E_{01} E_{02} cos\big((\boldsymbol{k_1} - \boldsymbol{k_2}).\boldsymbol{r} + (w_1 - w_2)t + (\varphi_1 - \varphi_2)\big) \end{aligned} \tag{2.19}$$

Furthermore if we assume $w_1 = w_2$, then:

$$I \propto \frac{1}{2}E_{01}^2 + \frac{1}{2}E_{02}^2 + E_{01}E_{02}cos\big((\boldsymbol{k_1} - \boldsymbol{k_2}).\boldsymbol{r} + (\varphi_1 - \varphi_2)\big) \tag{2.20}$$

If both light waves propagate at the same direction with the same propagation constant ($\boldsymbol{k_1} = \boldsymbol{k_2}$), then:

$$I \propto \frac{1}{2}E_{01}^2 + \frac{1}{2}E_{02}^2 + E_{01}E_{02}cos(\varphi_1 - \varphi_2) \tag{2.21}$$

Therefore irradiance can be expressed as

$$I = I_1 + I_2 + 2\sqrt{I_1 I_2}cos(\varphi_1 - \varphi_2) \tag{2.22}$$

where $I_1 = \frac{1}{2}\epsilon\upsilon E_{01}^2$ and $I_2 = \frac{1}{2}\epsilon\upsilon E_{02}^2$.

The radiation pattern is called interferogram and $(\varphi_1 - \varphi_2)$ is the phase difference between two waves. Assuming that one of the phases is known (e.g. φ_1 is known) and the other one is modulated by the information; then the phase difference $(\varphi_1 - \varphi_2)$ which exists in the interferogram, carries the information.

As it is seen from above equation, the interference pattern has a sinusoidal shape. Since I_1 and I_2 are positive quantities, the maximum irradiance is where two light waves are completely out of phase, i.e.

$$\varphi_1 - \varphi_2 = 2k\pi + \pi, \qquad k \in \mathbb{Z} \rightarrow \ I_{min} = I_1 + I_2 - 2\sqrt{I_1 I_2} \tag{2.23}$$

The maximum, on the other hand, happens when two light waves are in-phase:

$$\varphi_1 - \varphi_2 = 2k\pi, \qquad k \in \mathbb{Z} \rightarrow \ I_{max} = I_1 + I_2 + 2\sqrt{I_1 I_2} \tag{2.24}$$

Visibility is a function that gives the contrast of the interferogram. It is defined as:

$$V = \frac{I_{max} - I_{min}}{I_{max} + I_{min}} \tag{2.25}$$

Maximum visibility, 1, can be obtained when light waves have the same amplitude and it is minimum when there is no variation in irradiance. Using equation derived above the visibility can be written as:

$$V = \frac{2\sqrt{I_1 I_2}}{I_1 + I_2} \tag{2.26}$$

Figure 5 shows the visibility in terms of ratio of I_1/I_2. As it is seen from the figure, even when the amplitudes of light waves are not the same, the visibility can be at acceptable level. For example if $I_2 = \frac{1}{10} I_1$ then visibility is 0.57, which is an acceptable visibility.

For other form of light waves the interference has the same general form, which is a sinusoidal shape. For example, assume the light waves are spherical waves:

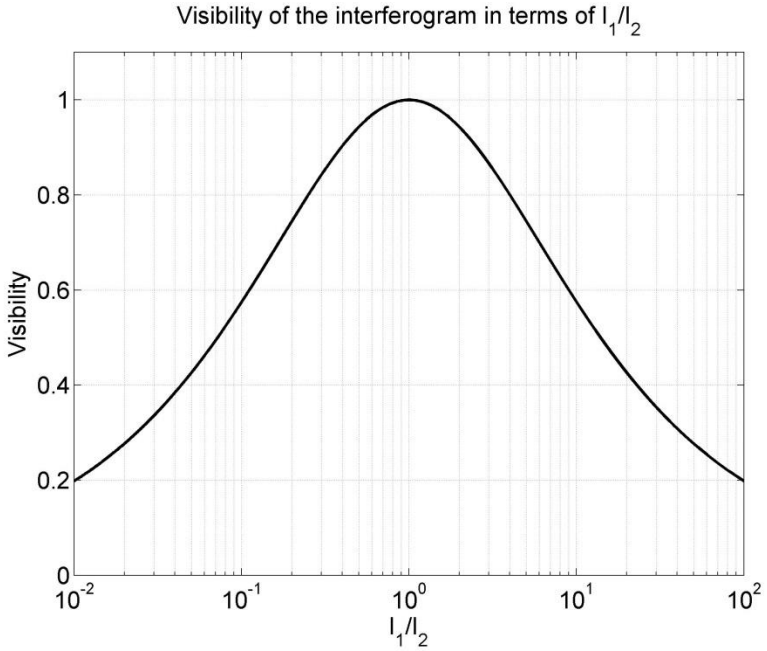

Figure 5: Visibility of interferogram in terms of the relative intensity of two interfering waves

$$\boldsymbol{E_1} = \frac{\boldsymbol{E_{01}}}{\boldsymbol{r_1}} cos(\boldsymbol{k_1}.\boldsymbol{r_1} + w_1 t + \varphi_1) \quad (2.27)$$

$$\boldsymbol{E_2} = \frac{\boldsymbol{E_{02}}}{\boldsymbol{r_2}} cos(\boldsymbol{k_2}.\boldsymbol{r_2} + w_2 t + \varphi_2) \quad (2.28)$$

Then the phase difference can be calculated as: $\delta = (\boldsymbol{k_1}.\boldsymbol{r_1} - \boldsymbol{k_2}.\boldsymbol{r_2}) + (w_1 - w_2)t + (\varphi_1 - \varphi_2)$ where $\boldsymbol{r_1}$ and $\boldsymbol{r_2}$ are the radii of spherical waves at the point of interference.

2.2.2. Coherence

As it was mentioned before, one condition for interference is coherence. Coherence describes the statistical properties of radiation, which are correlation functions. For example, two-beam interference is a simple correlation of order of two between two light waves.

There are two types of coherence namely time coherence and spatial coherence.

Suppose that the radiation source has frequency content with the bandwidth of $\Delta\nu$. Then the coherence time is defined as the inverse of bandwidth, i.e. $\Delta\tau = {}^{1}/_{\Delta\nu}$. Another quantity that relates to the coherence time is coherence length, which is defined as $\Delta l = c\Delta\tau$ where c is the speed of wave. These parameters show the temporal coherence properties of a radiation source.

Spatial coherence relates to the size of the radiation source. Assuming a light source illuminates two pinholes P_1 and P_2 with solid angle of $\Delta\Omega$, and these two secondary sources form an interferogram at a screen. If the mean wavelength of light source is λ and separation between the secondary sources are Δu then fringes will be visible if [5]

$$(\Delta u)^2 \Delta\Omega \sim \lambda^2 \quad (2.29)$$

$(\Delta u)^2$ is called the area of coherence of the light source.

Mutual coherence is a function that characterizes the coherence of light source and is defined as the time average of cross correlation between electric fields originated from the light source. Detailed discussion of coherence can be found in [31], [32].

2.2.3. Interferometers

Interferometers are instruments that employ interferometry to measure a wide range of objects and surfaces [4]. There are different configurations for interferometers including the Michelson interferometer, the Mach-Zehnder interferometer, the Fizeau interferometer, etc. In all interferometers two or more waves interfere and the resultant interference pattern is used to calculate a wavefront change that results from transmission through or reflection from an object of interest. The wavefront change, in turn, corresponds to the parameters and/or features of interest concerning the object under measurement. In the following, some of the common interferometers will be described.

2.2.3.1. Michelson Interferometer

Michelson interferometer is the most common interferometer. A Michelson interferometer configuration is illustrated in Figure 6. The light wave from the source is divided into two beams, after passing through beamsplitter. Both beams are reflected from mirrors and parts of each beam that goes downward are combined to make interference. The interference pattern then is captured by the detector. The beam that goes upward, passed through beamsplitter three times (assuming that the right surface of beamsplitter splits the beam), while the beam that goes to the right passes through beamsplitter just once. To compensate for that, a compensator, which has the same material and thickness of beamsplitter, is put in the path of the beam that goes to the

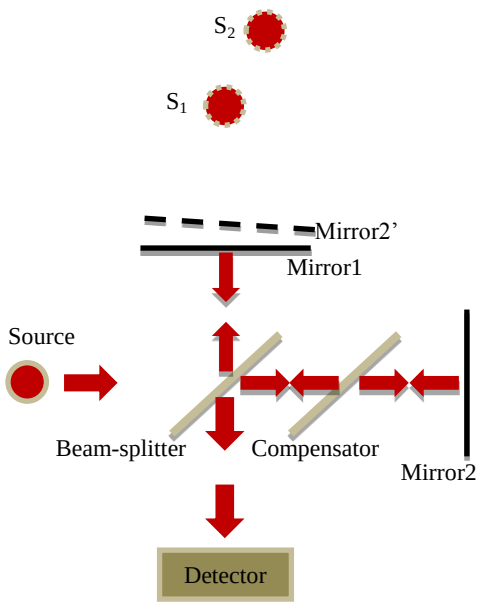

Figure 6: Michelson interferometer

right. This beam passes through compensator two times and therefore any path difference comes from actual optical path difference.

Mirror 2' is the image of mirror 2 which is the result of reflection from beam-splitter. If the mirror 2 has tilt with respect to the mirror 1 (i.e. the planes of mirrors are not perpendicular), then the image of mirror 2 also has a tilt with respect to the mirror 1 (i.e. they are not parallel). Otherwise the mirror 2' is parallel to the mirror 1. Looking from the detector the interference is the result of the interference between waves coming from the source at mirror 1 (S_1) and the source located at the virtual mirror 2' (S_2).

For parallel mirrors 1 and 2' (no tilt), the line that connects images of the source (S_1S_2) is perpendicular to the mirror 1 plane. On the other hand, if there is a tilt between the mirrors, the line S_1S_2 has an angle with the normal to the mirror 1 plane.

The straight line fringes can be seen if the source is monochromatic point source and line S_1S_2 is parallel to mirror 1. These parallel lines are actually hyperbolic fringes which

are approximated as straight lines when the distance of line S_1S_2 from the detector is much larger than the separation between S_1 and S_2. The straight line fringes also can be formed with an extended monochromatic source if there is a small angle between mirror 1 and virtual mirror 2' and again the separation between S_1 and S_2 is very small compared to the distance of virtual sources from the detector.

The circular fringes are formed with a monochromatic point source, when mirror 1 and virtual mirror 2' are parallel. With an extended monochromatic source, circular fringes are formed when mirror 1 and virtual mirror 2' are parallel, but they have a finite distance from each other. If mirror 1 and virtual mirror 2' coincide then the fringe pattern will have a uniform intensity pattern.

Michelson interferometer can be used for very precise length measurements [33], gravitational wave detection [34], refractive index measurement [35], [36] and precise displacement measurement [37].

2.2.3.2. Rayleigh Interferometer

The schematic of the Rayleigh interferometer is shown in Figure 7. Rayleigh interferometer is a division by wavefront interferometer. The source wavefront is split into two beams, each beam is passed through the objects and the beams interfere

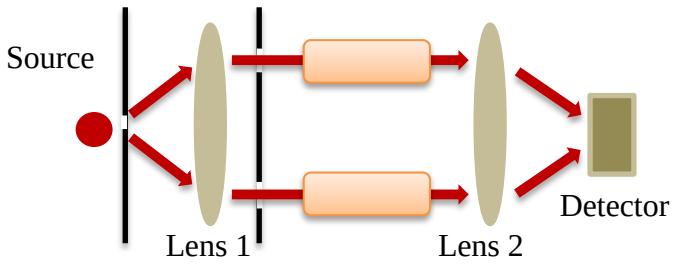

Figure 7: Schematic of Rayleigh interferometer

afterward. Lens 1 is used to collimate the light and lens 2 is used to bring the beams together to interfere. As it is seen the Rayleigh interferometer is a simple interferometer and can measure the optical path difference very precisely. One of the drawbacks of this interferometer is high density of fringes that requires magnification in order to analyze the interferogram. Rayleigh interferometers are used in determination of diffusion coefficients [38], [39], [40], [41]

2.2.3.3. Mach-Zehnder Interferometer

Schematic of a Mach-Zehnder interferometer is demonstrated in Figure 8. The beams are divided using the beam-splitter 1. Each beam reflects from a mirror and they are combined using beam-splitter 2. The optical difference between beams can be produced using a slight tilt in one of the mirrors or by inserting a wedge in the path of one of the beams. This interferometer has been used for label-free detection of liquids [42], biological and chemical properties of materials [43], [44] and refractive index sensor [45].

2.2.3.4. Sagnac Interferometer

In Sagnac interferometer, both beams go through the same loop but in opposite

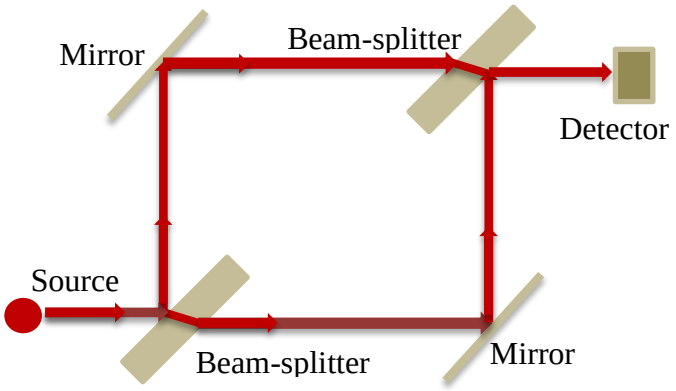

Figure 8: Mach-Zehnder interferometer

directions and then recombine, which makes this interferometer very stable and easy to align. Figure 9 shows the schematic of the Sagnac interferometer with 3 mirrors. It is also possible to make a Sagnac interferometer with one beam-splitter and two mirrors.

Sagnac interferometer with three mirrors is insensitive to the displacement of mirrors and beam-splitter while the Sagnac interferometer with two mirrors produces a shear when the mirrors or beam-splitter is displaced.

Sagnac interferometers are used as sensors for current [46], temperature [47], strain [48], rotation and gravitational wave detection [49], and in optical switches [50].

2.2.3.5. Fiber Interferometer

Fiber interferometers are the implementation of interferometers using optical fibers. The optical fibers that are used in fiber interferometers are usually single mode fibers; although birefringent fibers are also used. Figure 10 shows the schematic of a fiber Michelson interferometer. A laser source, usually a semiconductor laser, is coupled to the optical fiber. A coupler is used as the beam splitter. Lights reflect back from the end faces

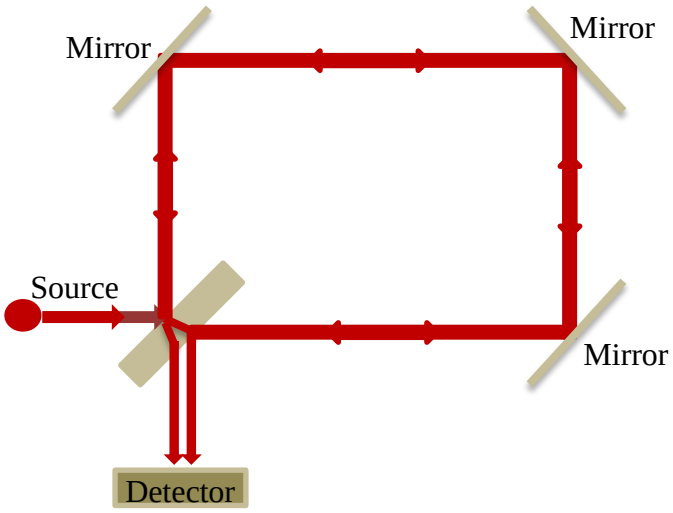

Figure 9: Sagnac interferometer

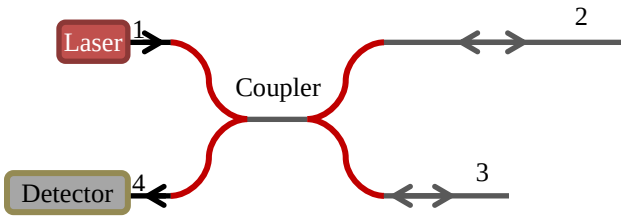

Figure 10: Schematic of a fiber Michelson interferometer

of the fibers, which act as mirrors, interfere at the fiber coupler. The end of fibers can be just cleaved to reflect about 4 percent of the light or can be coated in order to form high reflectivity fiber mirrors. The fiber interferometer can be used to measure relative phase difference between beams from the two arms, which one acts as a reference arm [51]. Piezoelectric fiber stretcher has been used in one arm of such fiber interferometers for signal processing of output signals [52].

The fiber interferometers are widely used as sensors for measurement of different physical, chemical and biological parameters [53] including displacement [54], temperature [47], strain [55], humidity [56], and multi-parameter sensors [57], [58]. The basic principle of a fiber interferometer functioning as a sensor is the fact that the physical quantities can change the refractive index and length of the optical fiber that results in change of optical path difference of fiber interferometer.

2.3. Fringe Pattern Analysis

The output of moiré systems and laser interferometers are fringe patterns. Fringe patterns contain the information about the object that the fringe patterns are formed from. Therefore fringe patterns are analyzed to extract the information about the parameter of interest, which can be the height, temperature, strain, etc. The first step, before analyzing the fringe pattern is preprocessing, which includes filtering to suppress the noise and

smoothing the fringe pattern. The next step is to calculate wrapped phase map from the preprocessed fringe patterns. The wrapped phase map is the corresponding phase of fringe pattern (relative to a reference phase on the fringe pattern), which is between 0 and 2π (or between $-\pi$ and $+\pi$). Therefore it has the ambiguity of $2m\pi$ where m is an integer number (therefore the name *wrapped* phase map).

There are two main methods to calculate the wrapped phase map from the fringe patterns [2]; the first method is the intensity method and the second one is phase measuring method. We briefly describe both methods in the following sections.

2.3.1. Intensity Methods

The intensity methods work directly on the intensity of fringe patterns. As mentioned above the first step after acquiring fringe pattern is to suppress the noise, which is usually done using filtering. There are different filters that can be used including Hanning filter, Hamming filter and Gaussian filter.

The next step in intensity methods is to recognize the fringes. The recognition of fringes can be done in one dimension or two dimensions. In one dimension, one line or average of several lines is used to recognize the fringes along that/those line(s). The line has to be perpendicular to fringes for effective fringe analysis. There are different methods to detect the fringes in one dimension including Max/Min fringe detection [59], [60], [61], Grey-level gradient change detection [62], Floating threshold fringe detection [63], Bucket-bin fringe detection [64], segmentation [65] and fringe thinning algorithms [66], [67].

After recognizing the fringes in fringe pattern, the order of the fringes have to be determined. Fringe order assignment, in which numbers are assigned to fringes, is

important since it enables to interpret the fringe pattern. Usually a priori knowledge of the object for order of fringes is needed [68]. Fringe ordering can be done manually or automatically.

2.3.2. Phase Measuring Methods

Phase measuring methods are another technique to analyze the fringe patterns. These methods are usually more accurate, mostly automated and without ambiguity [2]. Two main methods of these techniques are temporal phase measuring method and spatial phase measuring method. Temporal phase measuring methods acquire several intensity measurements in time in order to measure phase map of the fringe pattern. Spatial phase measuring methods, on the other hand, acquire fringe pattern simultaneously.

Spatial phase measuring methods include Fourier transform method [69], spatial carrier phase shifting and phase-stepped methods (Kwon and Shough 1985, Kujawinska and Wojciak 1991), wavelet transform methods [70], [71], [72], [73], short time Fourier transform methods [74], [75], [76], etc. Among these methods, Fourier transform methods are simple and accurate and do not have the complexity of wavelet transform methods and short time Fourier transform methods. Because of these advantages the decision was made to use Fourier transform for fringe analysis during this research effort.

In Fourier transform method the interferogram is in the form of

$$I(x,y) = a(x,y) + b(x,y)cos\big(2\pi f_1 x + 2\pi f_2 y + \varphi(x,y)\big) \tag{2.30}$$

where $\varphi(x,y)$ corresponds to the parameter of interest (e.g. height of the object) and (f_1, f_2) is the spatial frequency. The Fourier transform of interferogram can be written as:

$$\mathcal{F}\{I(x,y)\} = \Im(f_x, f_y) = A(f_x, f_y) + C(f_x - f_1, f_y - f_2) + C^*(f_x - f_1, f_y - f_2) \quad (2.31)$$

where $C(f_x, f_y)$ is the Fourier transform of $c(x,y) = b(x,y)e^{i\varphi(x,y)}$.

Therefore by filtering, the interferogram $c(x,y)$ can be extracted, namely the interferogram is filtered by a bandpass filter with center frequency of (f_1, f_2) and enough bandwidth to contain the information of $\varphi(x,y)$ and then shifting the filtered interferogram to the origin in frequency domain. After calculating $c(x,y)$, phase information can be extracted.

$$\varphi(x,y) = \tan^{-1}\frac{Im\{c(x,y)\}}{Re\{c(x,y)\}} \quad (2.32)$$

2.3.3. Phase Unwrapping

The next step in analyzing the fringe pattern is phase unwrapping. The output of Fourier transform method, in the last step, is the wrapped phase map; i.e. a phase map that has values between 0 and 2π (or $-\pi$ to $+\pi$). Therefore there is always an ambiguity of $2m\pi$ in the phase map (where m is an integer number). The phase unwrapping process removes this ambiguity in the phase map by finding the value of m for each pixel in phase map. The phase unwrapping problem first was analyzed by Itoh [77] for one dimension signals. Itoh showed that the phase can be unwrapped by summing over the wrapped phase differences. Specifically if $\varphi[n]$ shows the unwrapped phase at location n, and $\mathcal{W}(\varphi[n])$ shows the wrapped phase at the same location where:

$$\mathcal{W}(\varphi[n]) = \varphi[n] + 2k\pi, \qquad k \in \mathbb{Z}, \quad -\pi \le \mathcal{W}(\varphi[n]) < \pi \quad (2.33)$$

Then the unwrapped phase at location $n+1$ is:

$$\varphi[n+1] = \varphi[n] + \mathcal{W}\big(\mathcal{W}(\varphi[n+1]) - \mathcal{W}(\varphi[n])\big) \tag{2.34}$$

Two dimensional unwrapping is a more difficult task. There are two general approaches to this problem [78]. First approach is minimization methods. In this approach a cost function, which is usually an error function is defined. Then the optimization problem is to minimize the error. The cost function for minimization is defined as follows:

$$\begin{aligned} CF = \sum_{m=1}^{M-1}\sum_{n=1}^{N} \big|(\varphi[m+1,n] - \varphi[m,n]) \\ - \big(\mathcal{W}(\varphi[m+1,n]) - \mathcal{W}(\varphi[m,n])\big)\big|^p \\ + \sum_{m=1}^{M}\sum_{n=1}^{N-1} \big|(\varphi[m,n+1] - \varphi[m,n]) \\ - \big(\mathcal{W}(\varphi[m,n+1]) - \mathcal{W}(\varphi[m,n])\big)\big|^p \end{aligned} \tag{2.35}$$

where the size of image is $M \times N$, $\varphi[m,n]$ shows the unwrapped phase at location (m,n), $\mathcal{W}(\varphi[m,n])$ indicates wrapped phase at point (m,n), and $|.|^p$ is L^p-norm. If L^2-norm is used for minimization, the problem will be a least square minimization. The solution for the phase unwrapping with least square minimization can be given as:

$$\begin{aligned} (\varphi[m+1,n] - 2\varphi[m,n] + \varphi[m-1,n]) \\ + (\varphi[m,n+1] - 2\varphi[m,n] + \varphi[m,n-1]) \\ = \big(\mathcal{W}(\varphi[m+1,n]) - 2\mathcal{W}(\varphi[m,n]) + \mathcal{W}(\varphi[m-1,n])\big) \\ + \big(\mathcal{W}(\varphi[m,n+1]) - 2\mathcal{W}(\varphi[m,n]) + \mathcal{W}(\varphi[m,n-1])\big) \end{aligned} \tag{2.36}$$

The equivalent continuous form of the above equation is Poisson's equation:

$$\nabla^2\varphi = \frac{\partial^2}{\partial x^2}\,\mathcal{W}\big(\varphi(x,y)\big) + \frac{\partial^2}{\partial y^2}\,\mathcal{W}\big(\varphi(x,y)\big) \tag{2.37}$$

There are different methods to solve the equations (2.35) and (2.36) to unwrap a wrapped phase. Examples of these approaches are phase unwrapping using FFT [79], multigrid technique [80] and L^p-norm method [81].

In FFT approach the phase map is extended to form a periodic function by mirroring the phase map. Then the resulting phase map is used to solve the least-square two-dimensional phase unwrapping equation by taking the FFT from the Poisson equation, solving the Poisson equation for Fourier transform of unwrapped phase and then taking inverse FFT to retrieve unwrapped phase map.

Multigrid technique first solves the problem of phase unwrapping in a coarser grid by using schemes like Gauss-Seidel relaxation. At next step the method moves to finer grids and using the data from the last steps to find a solution.

L^p-norm method solves the problem of phase unwrapping using norms other than L^2-norm.

All these techniques can have weighted phase map. The weighted methods weight each point of the phase map according to a criterion. For example, the weight can be a quality map that shows the quality of each pixel on the phase map.

Second approach in phase unwrapping is path-following approach. In path-following methods a path is defined and the unwrapping process is done through that path. One dimensional phase unwrapping can be extended to N-dimensional unwrapping by using the following equation:

$$\varphi(\mathbf{r}) = \oint_C \nabla\varphi . \mathbf{dr} + \varphi(\mathbf{r_0}) \tag{2.38}$$

Where $\mathbf{r}$ and $\mathbf{r_0}$ are N-dimensional location vectors, $\nabla\varphi$ is phase gradient and C is any path from $\mathbf{r_0}$ to $\mathbf{r}$. Since we want to have a unique solution for unwrapped phase, the integral should be independent of the path of integration. This condition is satisfied by choosing proper paths for unwrapping. The locations that cause the integral in equation (2.38) to be path dependent are called residues. Therefore to make the integral independent of path, either path should include no residues or path includes residues that cancel out the effect of each other when unwrapping.

There are different approaches that use path-following to unwrap the phase. This includes Goldstein algorithm [82], quality guided algorithm [83] and combined branch cut and quality guided algorithm [84].

In Goldstein algorithm, a segments branch cuts are defined for phase map and the unwrapping path should not cross branch cuts. Branch cuts are the parts of phase map that violate the independency of integral in equation (2.38) from the path. Therefore avoiding branch cuts makes the error minimum. The Goldstein algorithm tries to minimize the total length of branch cuts. It is a very fast algorithm compared to other path-following techniques.

Instead of identifying the branch cuts, quality guided algorithm chooses a quality path for unwrapping. The quality map defines a path in which the integral in equation (2.38) is calculated. Quality map can be derived from the phase map or other sources. Examples of quality maps are variance of phase derivatives, maximum phase gradient and amplitude of Short Time Fourier Transform (STFT).

Quality guided algorithm starts from a point with high quality (according to quality map) and unwraps the four neighbor pixels; then the neighbor unwrapped pixel with highest quality is selected and again four neighbor pixels are unwrapped, unless they are already unwrapped. This procedure continues until all pixels with acceptable quality are unwrapped.

One can combine branch cut technique with quality map in which the choice of branch cut is guided by a quality map. This technique take advantage of both branch cut and quality guided techniques. This technique is more time consuming that the other path following techniques.

Comparing the mentioned techniques, it was shown [78, pp. 285–286] that the quality guided technique can successfully unwrap almost all wrapped phase maps. In terms of complexity and time consumption, quality map is more time efficient and less complex that the other techniques with similar performance (e.g. Mask cut).

In another comprehensive comparison [85] it was shown that the quality guided technique is the only method to successfully unwrap the interferometry phase maps.

Since our fringe pattern and phase maps are interferograms from laser interferometry and moiré technique, we choose to use quality guided technique that has the combination of good performance, low complexity and being fast. For the quality map we used STFT quality map, which is proposed by Qian Kemao [86].

CHAPTER 3: DUAL MOIRÉ LASER INTERFEROMETER

As its name suggests, the dual moiré laser interferometer consists of a moiré based instrument and a laser interferometer. The aim of designing this system is to measure an object in different scales (zoom levels) and different resolutions with a single instrument; therefore this is a multiscale measurement instrument. This chapter describes different aspects of the design and implementation of this measurement instrument. First the hardware design and different implemented prototyped are explained. The next section is dedicated to the system simulation. Both moiré and laser interferometer are simulated and the outputs of the system are shown at different levels of the zoom. This follows by a section on stitching algorithm. The proposed algorithm and the image registration, which is the core of this algorithm is explained and fringe patterns simulated in the previous section are used to evaluate the proposed algorithm. The fringe pattern analysis software is described and demonstrated in a separate section. The aim of this software is to calculate the profile of objects under test from the fringe patterns acquired from the dual moiré laser interferometer. The last section of this chapter discusses the experimental results, errors in the measurement system, and error analysis of the dual moiré laser interferometer.

3.1. System Design

Different prototypes were designed and implemented for the dual moiré laser interferometer. Each prototype was designed to overcome the problems and issues that

have existed in the previous one. Figure 11 shows the schematic of the first prototype. The shaded part in Figure 11 is common part between the moiré and laser interferometer. We refer to the left side of the system as *projector arm* (the side that the projector is placed) and the *camera arm* is referred to the right side of the system (the side that the camera is placed.)

For moiré measurement, a fringe projection technique is used; a moiré pattern is projected and deformed by the object. The deformed pattern is then captured by the camera and is used to calculate the form of the object. The laser interferometer is a partially fiber and partially free space laser interferometer. The phase difference of the laser wavefront at the two ends of the fiber is kept constant using a feedback system. The

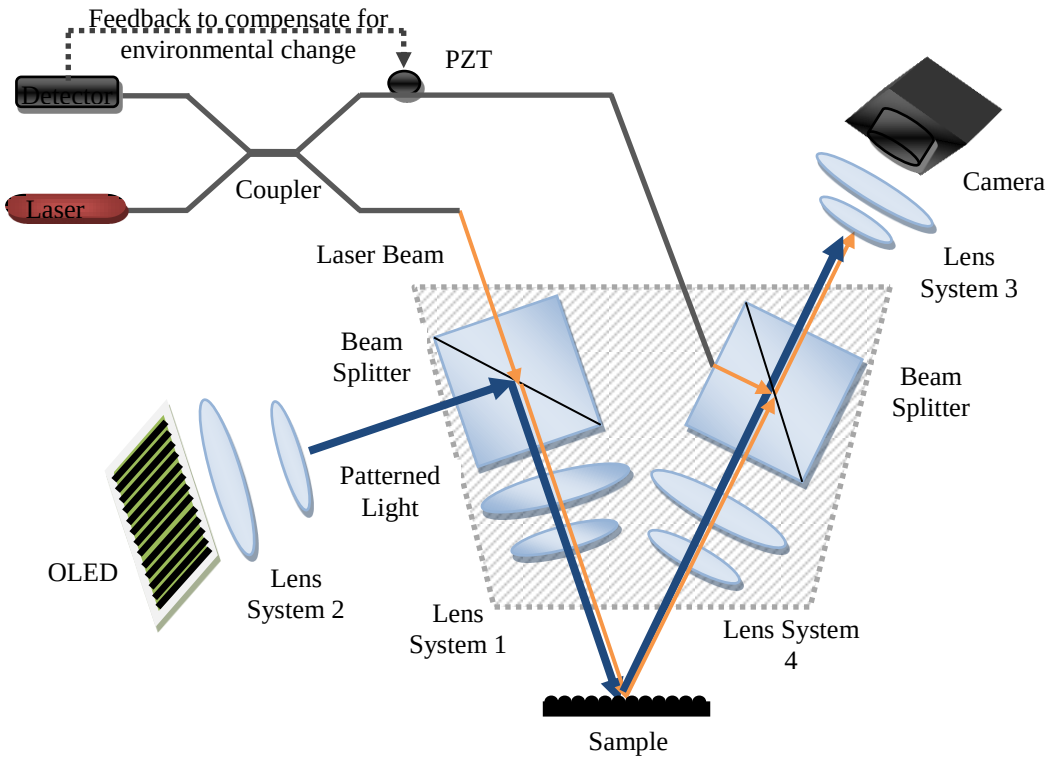

Figure 11: Schematic of the dual moiré laser interferometer

laser beam interferes with reference beam after reflecting from the object and the interference pattern is detected by the same camera. Figure 12 shows the first implemented prototype. A stereo microscope is used as a common part (the shaded part in schematic of Figure 11). The stereo microscope is Leica Wild M32 stereo microscope. The eyepieces of the stereo microscope have been removed and two fixtures were made to hold the camera and the projector. The camera that was used is a monochromatic CCD camera from Industrial Vision Source. The projector is an SVGA+ OLED-XL microdisplay from eMagin2. The resolution of the OLED microdisplay is 852×600 pixels.

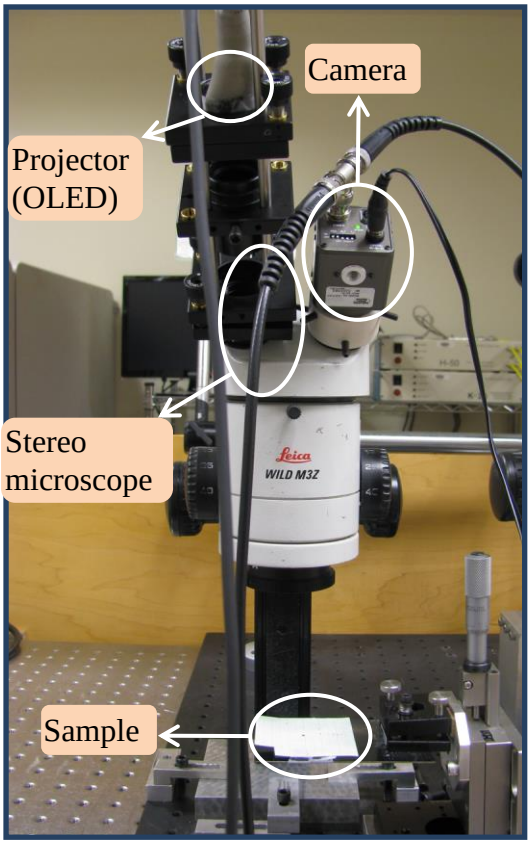

Figure 12: First prototype of dual moiré laser interferometer using a stereoscope microscope

[2] http://www.emagin.com/oled-microdisplays/

The advantage of using OLED microdisplay is that the projection pattern (moiré pattern) can be changed in software and there is no need for any hardware modification (e.g. using different Ronchi rulings). Another advantage of OLED microdisplay is the small size. The size of OLED microdisplay is about $20 \times 15 \times 5\, mm$ which makes it suitable to put on the stereo microscope.

Figure 13 shows a moiré pattern that projected by the OLED microdisplay and captured by the camera. Because the power of the OLED microdisplay is low (150 cd/m^2 and considering the viewing area of the OLED microdisplay the brightness is about $150 \frac{cd}{m^2} \times 12.78 \times 10^{-3} m \times 9 \times 10^{-3} m \times 12.57 \frac{lumen}{cd} \approx 0.22\, lumen$), the captured moiré pattern does not have enough brightness.

There are other problems with this prototype; first the change of zoom levels for the projector and camera arms are not independent and are the same for both arms. This means that we cannot change the zoom level in camera side without keeping the pitch of the moiré pattern fixed. (We can adjust that in software, but since the exact change of zoom level is not known, the compensation in software will not be exact.)

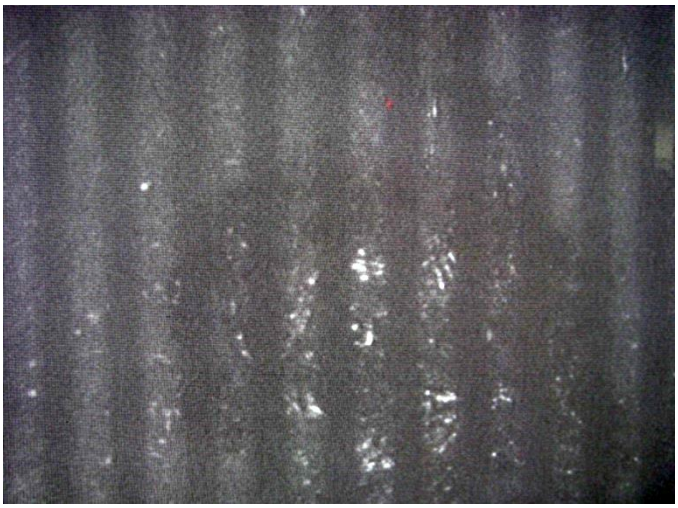

Figure 13: Fringe pattern of moiré part from first prototype. The area is approximately 1mm^2

The second problem arises when we change the zoom level. By changing from one zoom level to another the center of the captured images shifts and goes out of the field of view for a change of zoom level of four. Assume that image1 is captured at zoom level one and image2 is captured at zoom level 4. Then the center of image1 is not inside the frame of image2 and vice versa. One way to overcome this problem is to change the position of the camera correspondingly. But this approach needs some mechanical movements and corresponding stages and therefore adds to the complexity of the system.

To overcome the problems in the first prototype, the system was redesigned. The schematic of the design is the same. But instead of using a stereomicroscope, we used two separate zoom lenses to decouple the projector arm and camera arm. Figure 14 shows the implemented system. Two zoom lenses are VZM 450 Zoom Imaging Lens[3]. The angle between both projector and camera arms with normal is twenty degrees. The zoom lenses have the range of 1x to 4.5x zoom level and can be adjusted independently.

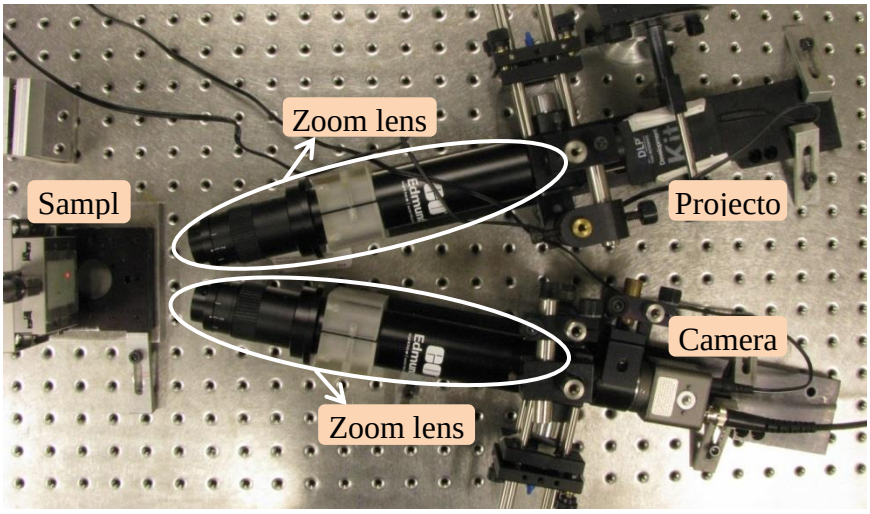

Figure 14: The second prototype; the stereoscope was replaced by two zoom lenses in order to decouple the projector arm and the camera arm.

[3] http://www.edmundoptics.com/imaging/imaging-lenses/zoom-lenses/vzm-zoom-imaging-lenses/3280

The OLED microdisplay was replaced by a DLP-based Picoprojector from Texas Instruments (made by YoungOptics). The Picoprojector resolution is 480×320 pixels and the brightness is 7 lumens.

The laser interferometer of dual moiré laser interferometer is a partial fiber – partial free space interferometer. Figure 15 shows the test setup for laser interferometer. As it is seen the laser is a red HeNe laser ($\lambda = 632.8\, nm$). The laser beam is launched into a single mode fiber and divided into two beams using a 50-50 coupler/divider. The partial back reflection from F2 and F3 ends of the fiber are used to stabilize the interferometer. Namely, the laser beams from ends of fiber (F2 and F3) partially reflect back and couple into the other end of fiber coupler/divider (F4) and interfere. The interference intensity is measured using a large area silicone photodiode[4]. After magnification and filtering, the

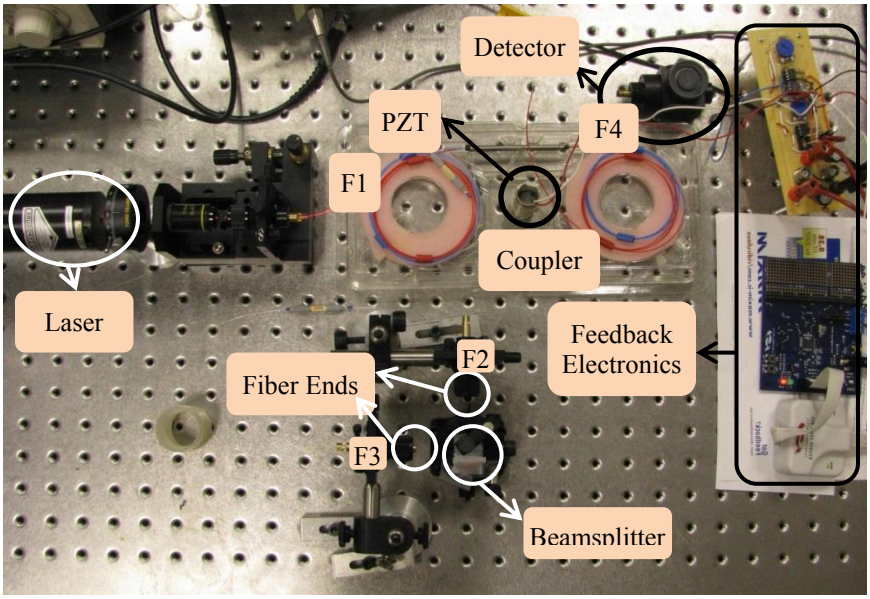

Figure 15: Test setup for partial fiber – partial free space laser interferometer. F1, F2, F3 and F4 are four ends of fiber coupler/divider

[4] http://www.thorlabs.us/thorProduct.cfm?partNumber=FDS100

output of the detector is fed to a digital feedback system. The digital feedback system uses this output to stabilize the phase difference at the ends of the fibers (ends F2 and F3), which stabilizes the interferometer. To do so, one arm of the coupler is wrapped around a PZT. By applying a voltage to the PZT, the PZT expands and contracts, which in turn changes the property of the fiber that is wrapped around the PZT. This change causes the change in the effective optical path of the laser in a way to stabilize the phase difference of laser beams at the two ends of the fiber (ends F2 and F3). Figure 16 shows the schematic of the digital feedback system. The control unit of the feedback system is a precision mixed-signal microcontroller[5] from SiliconLabs.

As it is shown in Figure 17 the feedback process consists of two steps: the initialization and the tracking. In the initialization step a triangular voltage is applied to the PZT. The PZT (Boston Piezo Optics Inc[6]) has an outside diameter (OD) of 0.728", wall thickness of .060" and length of 2". The material of the PZT is PZT-5H. The radial change of a PZT occurs according to the following equation:

$$\Delta r = d_{33} V \tag{3.1}$$

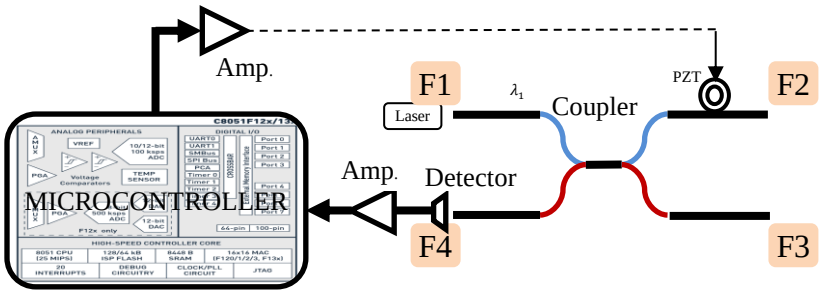

Figure 16: The schematic of laser interferometer with digital feedback system

[5] http://www.silabs.com/products/mcu/Pages/C8051F120DK.aspx
[6] http://bostonpiezooptics.com/

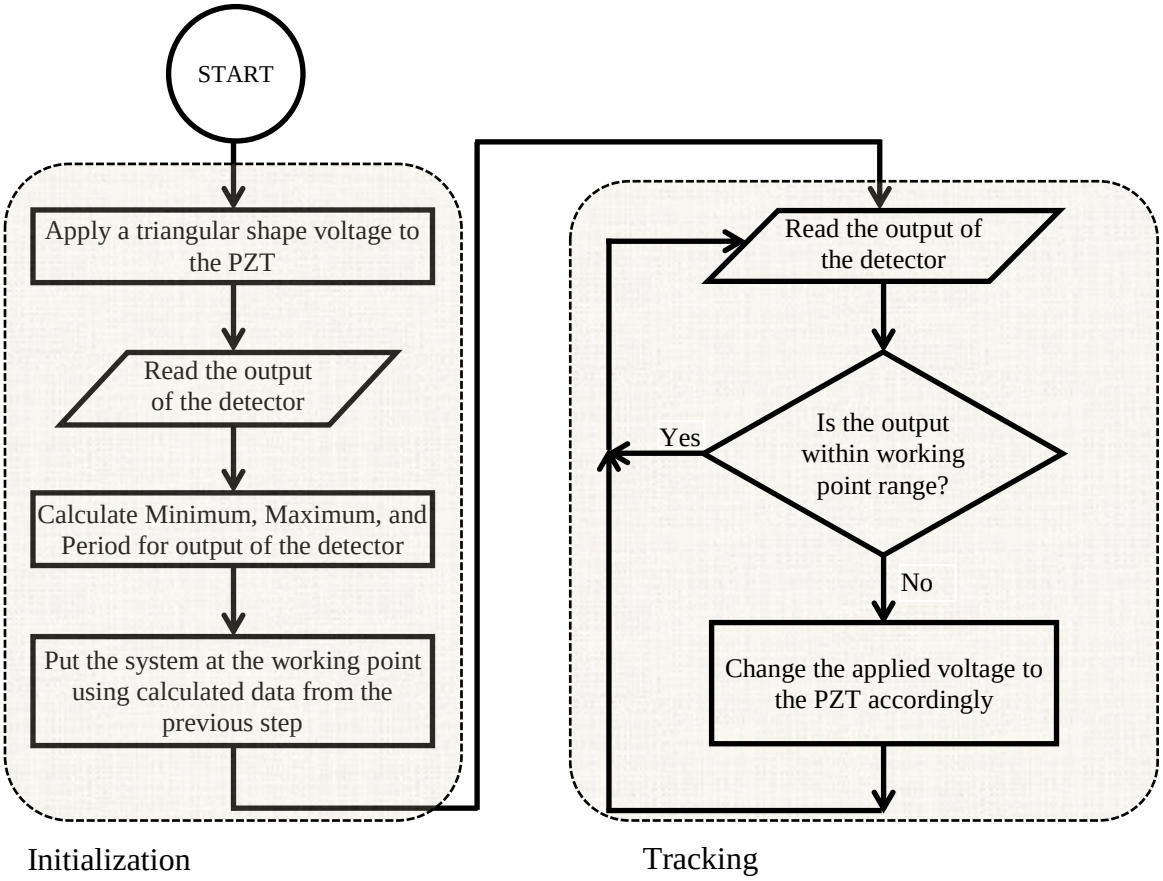

Figure 17: The flowchart of digital feedback software

where V is the applied voltage to the PZT and d_{33} is a piezoelectric constant. For PZT-5H material that constant is $d_{33} = 585 \times 10^{-12}\, m/V$ [7].

By wrapping a fiber around the PZT and applying a voltage the length and refractive index of the fiber will change. Considering the change in the length of the fiber, we wrapped about 80 turns of fiber around PZT. Therefore, the change of the length of the fiber per one volt would be:

$$\Delta l \;=\; 2\pi\Delta r \times N = 2\pi d_{33} V \times N \;=\; 2\pi \times 585 \times 10^{-12} \times 1 \times 80 = 294\, nm$$

[7] http://bostonpiezooptics.com/ceramic-materials-pzt

Assuming the refractive index of fiber to be $n \approx 1.5$ and the laser wavelength $\lambda = 632.8\,nm$, the equivalent phase change of laser beam would be:

$$\Delta\varphi = \frac{2\pi n \Delta l}{\lambda} = \frac{2\pi \times 1.5 \times 294 \times 10^{-9}}{632.8 \times 10^{-9}} \cong 1.39\pi$$

Therefore to change the phase by 2π, the required voltage would be: $V = 2\pi/1.39\pi = 1.43\,V$. The applied voltage to the PZT is a triangular voltage with the amplitude of $5V$ and period of 0.5 sec. This triangular signal is synthesized with microcontroller and amplified using an analog circuit (Figure 18). The triangular signal with an amplitude of $5V$ causes the phase of the laser beam to change $5/1.43 \times 2\pi \approx 7\pi$, which results in a couple of periods $5V$ of the sinusoidal signal at the detector output. The output of the detector is amplified, filtered and converted to a digital signal. Figure 19 shows the corresponding circuit.

The microcontroller acquires the output of the detector and calculates the average period, and minimum and maximum voltage value. By calculating those parameters, the digital feedback system knows how change in PZT voltage changes the phase difference of laser beam at the ends of the fiber interferometer.

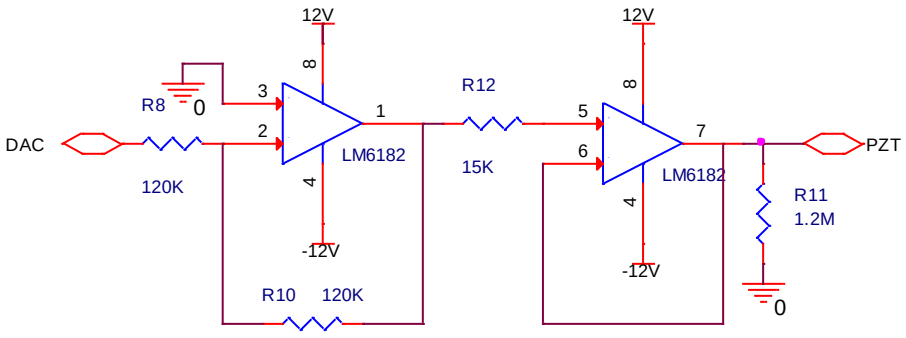

Figure 18: Analog circuit for applying voltage to the PZT

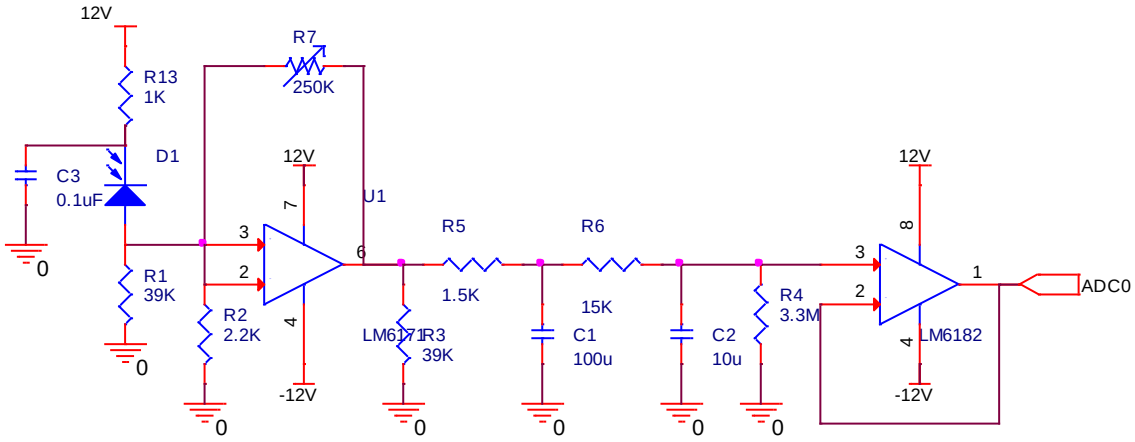

Figure 19: The circuit for acquiring the output of the detector

The next step after initialization is tracking. In the tracking step, first the laser interferometer is put at a working point. Working point for the laser interferometer is usually at quadrature; i.e. the phase difference of ninety degrees. At quadrature working point, the laser interferometer is more sensitive to the changes, which makes it possible to keep the laser interferometer at this position more precisely. This results in a more stable laser interferometer.

Mathematically assume that the output of the interferometer is as follows:

$$V = V_b\left(1 + \gamma cos\big(\varphi(t)\big)\right) + N_E \tag{3.2}$$

where γ is the fringe contrast, N_E is the electronic noise, and $\varphi(t)$ is the phase difference. The sensitivity of output voltage to the phase change would be:

$$\frac{\partial V}{\partial \varphi(t)} = -V_b \gamma sin\big(\varphi(t)\big) \tag{3.3}$$

and the maximum of sensitivity occurs when:

$$\frac{\partial}{\partial \varphi(t)}\frac{\partial V}{\partial \varphi(t)} = -V_b \gamma cos\big(\varphi(t)\big) = 0 \quad \rightarrow \quad \varphi(t) = k\pi + \pi/2 \tag{3.4}$$

which means that the sensitivity is maximum when the laser interferometer is at quadrature.

After putting the laser interferometer at its working point, the digital feedback system tracks the output of the detector by sampling it at the frequency of 1KHz and adjusting the voltage of PZT to compensate for environmental change and keep the laser interferometer at quadrature. Figure 20 shows the output of the detector along with the voltage applied to the PZT. Figure 20.a is the signals when the digital feedback is off. The applied voltage to the PZT is constant (orange signal) and the output of the detector, which shows the phase difference of laser beams at fiber ends F2 and F3 is unstable (blue signal). On the other hand, when the digital feedback system is on (Figure 20.b) the applied voltage to the PZT (orange signal) is changing in order to keep the laser interferometer stable (blue signal).

After making sure that the laser interferometer is stable, a laser interferogram is acquired from the laser interferometer (Figure 21). As it is seen, the interferogram suffers from high noise level including speckles. There are different methods to reduce the speckle [87], [88], [89], [90].

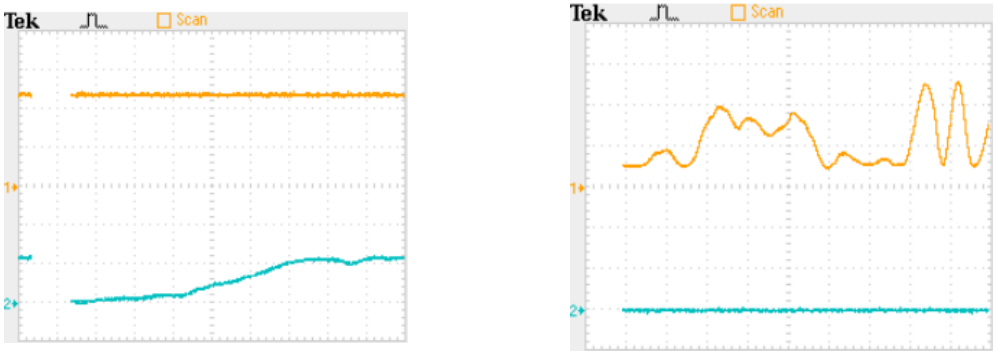

(a) (b)

Figure 20: The voltage applied to PZT (orange signal) and the detector output (blue signal) when (a): digital feedback is turned off and (b) digital feedback is turned on.

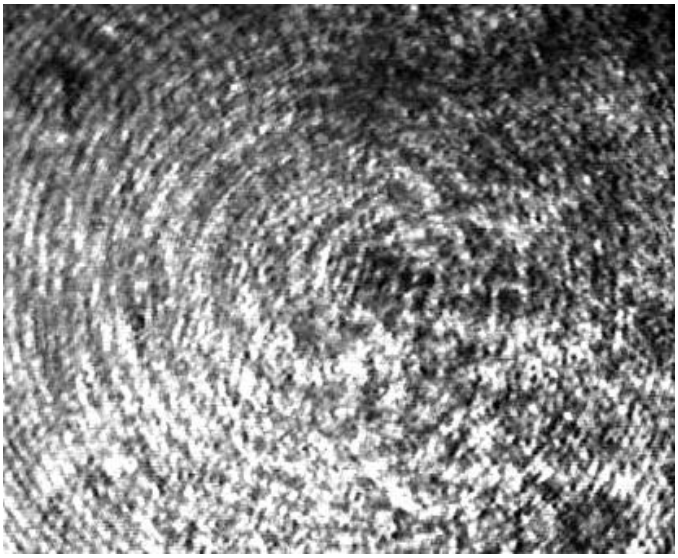

Figure 21: Interferogram from the laser interferometer

Reducing the spatial coherence of the laser beam is one way to reduce the speckle in hardware. One method to do so is to use a rotating ground glass in front of the laser beam at the end of the fibers (Figure 22). But since the two ends of the fiber have different rotating ground glass, this reduces the temporal coherence, too; which results in very poor interferogram (Figure 23).

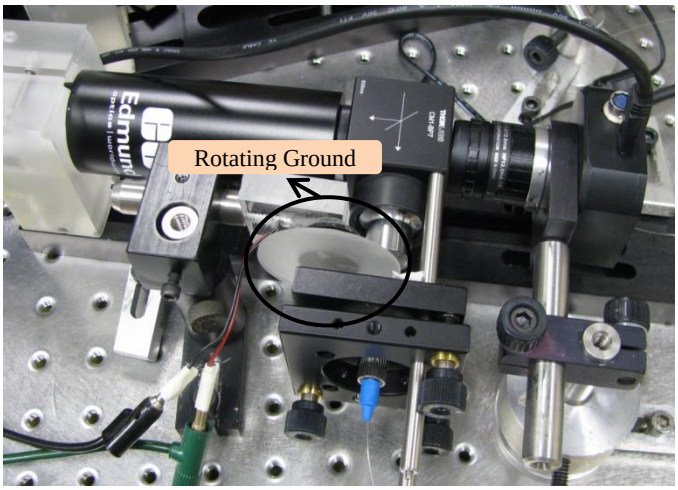

Figure 22: Adding a rotating ground glass to reduce the spatial coherence of laser beam in which results in speckle reduction

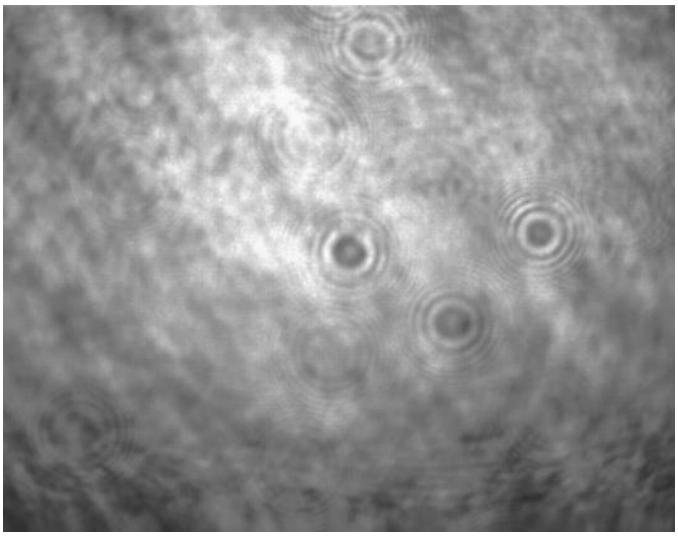

Figure 23: Interferogram after adding ground glass

We developed another technique to reduce the spatial coherence of the laser beam. This technique is based on dynamic mode combining in a multimode fiber. Figure 24 shows the schematic of this method. The laser beam is launched into a coupler with multimode fiber (I1). The beam is divided on the right side of couple 1 (I2 and I3). One arm of the coupler is wrapped around a PZT (I2). A high frequency (5KHz) noise like signal is applied to the PZT, which results in random changes on the fiber around the PZT and in turn changes the spatial modes of laser in the fiber. This mode-scrambled laser beam (arm I2) is mixed with the laser beam (arm I3) and coupled into arm O1. Since the change on arm I2 is random and very fast, the average of intensity over a range of tens of

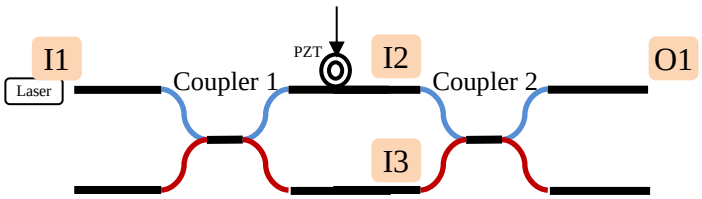

Figure 24: Setup to produce a uniform laser beam in order to decrease the speckle pattern

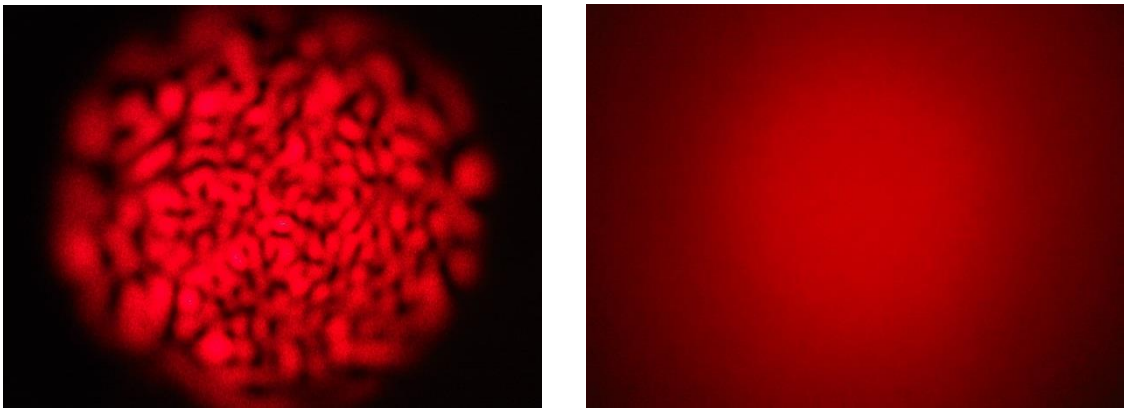

(a) (b)

Figure 25: Intensity profile of the laser beam using the proposed laser beam delivery system: (a) output of a multimode fiber (b): output of the proposed mode scrambling system when a high frequency random voltage applied to the PZT.

milliseconds or longer times is the average of random mode patterns of a multimode fiber. This average intensity is more uniform than the output of a simple single of multimode fiber. Figure 25 shows the intensity pattern of the proposed laser beam delivery system. Figure 25.a is the output of a multimode fiber and Figure 25.b shows the intensity profile when the modes are scrambled (a high frequency random signal is applied to the PZT). As it is seen the intensity pattern for the mode-scrambled laser beam is more uniform than a multimode fiber output intensity profile (no mode scrambling).

The next modification that was done on the system was improving the system performance by simulating some part of camera arm and projector arm in ZEMAX™. A lens is placed in front of projector in order to decrease the size of projected pattern. The lens has a diameter of 25.4 mm and a focal length of 24.5 mm (LB1761-A from ThorLabs[8]). The purpose of the first simulation was to find the proper distance between the lens and projector to minimize the projected pattern. Figure 26 shows the schematic

[8] http://www.thorlabs.us/NewGroupPage9.cfm?ObjectGroup_ID=4848&pn=LB1761-A#4864

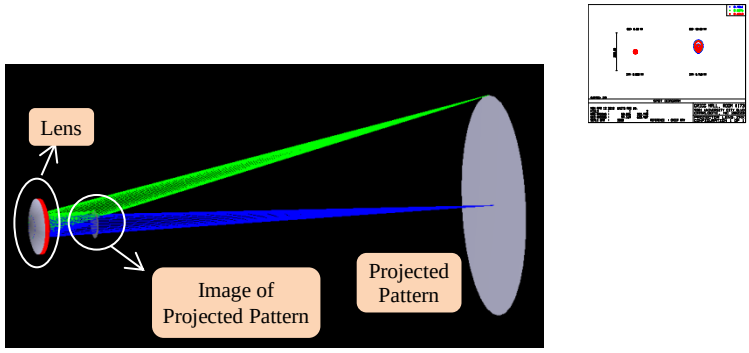

(a) (b)

Figure 26: ZEMAX simulation to minimize the projected pattern of the projector using two lenses: (a) the schematic of the lens system with object (projected pattern) and image (image of projected pattern) and (b): the spot diagram of the optimized system.

of the simulated system along with the spot diagram of optimized system. As it is seen assuming that the projected pattern has the diameter of 50 mm, the image of the projected pattern shrinks to 5.8 mm and the optimum distance of lens from the projector is 7.5 mm. The second simulation was on the camera arm (Figure 27.a), which uses a zoom lens to create an image on the camera and maximizing the resolution of the final image (by minimizing the spot size of the final image). For this setup we used two LB1761-A lenses

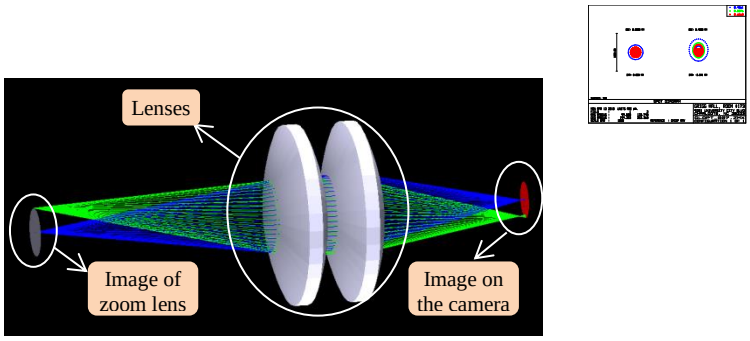

(a) (b)

Figure 27: ZEMAX simulation to optimize the resolution of the final image on the camera arm: (a) the schematic of two lenses with object (image of zoom lens) and image (image on the camera) and (b) the spot diagram of optimized system.

and optimized the distance between the lenses and the distance between the lenses and the zoom lens. As Figure 27.b shows the spot size is about 100 μm. The optimum distance between the lenses is 2.3 mm and the distance between the lenses and the image of the zoom lens is 22.3 mm.

The results of simulation are used to modify both lens systems to obtain better interferograms.

The next modification was on the projector. Since working with the DLP-based Picoprojector needs a supporting beagleboard[9] it was replaced by a 3M MPro 110 micro projector (Figure 28), which directly connects to the computer. This projector has the resolution of 640×480 pixels and the brightness of 10 Lumens. The advantage of this projector is the straight projection; i.e. the projection is not off-axis, therefore there is no need to tilt the projector with respect to the optical axis of the projector arm. At higher zoom levels still the power of projector was not enough. Therefore that projector was

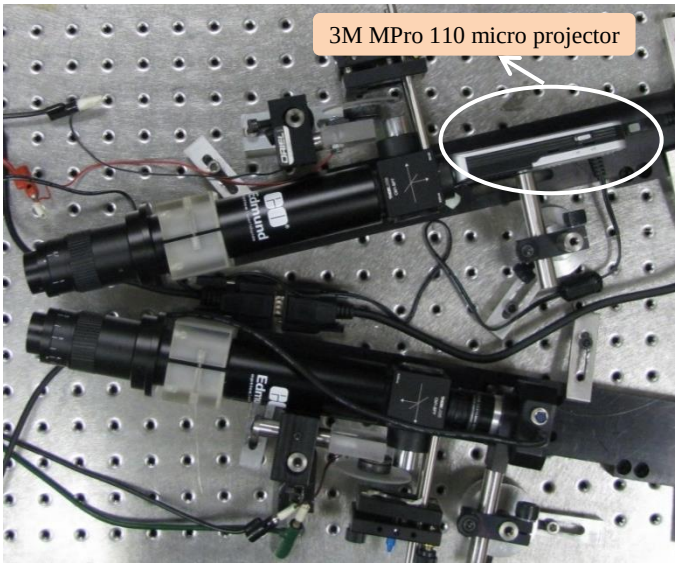

Figure 28: Setup with 3M MPro 110 micro projector

[9] http://beaglebard.org/

replaced by a AAXA M2 micro projector[10] (Figure 31). The M2 is LCoS (Liquid Crystal on Silicon) projector and its light source is LED and has a 110 Lumens brightness and the Native XVGA (1024x768) resolution.

The camera was also replaced by a SMX-11M5M camera which is a monochrome 5 megapixel (2592 x 1944) CMOS camera with USB2.0 interface[11] (Figure 31).

Figure 29 shows the interferogram from moiré and laser interferometer for a bump-shaped artifact (Solder bump). The acquired moiré pattern has enough intensity and can be analyzed using fringe analysis technique. The interferogram from the laser interferometer on the other hand has very dense fringes. The reason is that the laser beam goes through a few optical elements (before and after reflecting back from the object) before interfering with the reference beam. Therefore the interferogram contains the phase changes introduced by optical elements besides the object. Compensating these unwanted phase changes in software is a very difficult task if not impossible. To reduce the effect of unwanted phase changes in wavefront of laser beam we changed the position

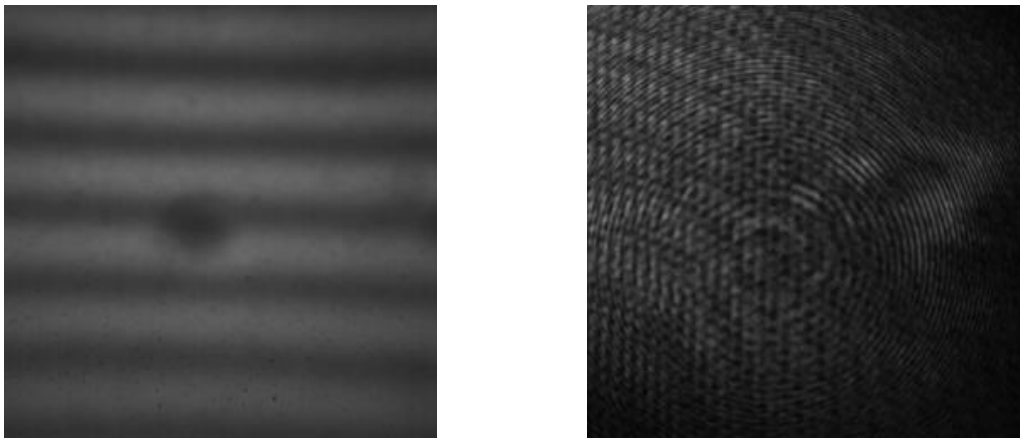

(a) (b)

Figure 29: Interferogram from Solder bump. (a): Moiré interferogram at zoom level 4x and (b): Laser interferogram at zoom level 12x

[10] http://www.aaxatech.com/news/m2_micro_projector.html
[11] http://www.sumix.com/products/cameras/smx-11m5m.html

of the laser interferometer and positioned it as close as possible to the object. This choice of location of laser interferometer makes sure that the laser wavefront almost only deformed by the object and not optical elements before interfering with reference beam of the laser. Figure 30 shows the schematic of the modified system. As it is seen in the schematic, the laser interferometer is close to the object and the interference between laser beam reflected from the object and the reference beam happens before beams enter the zoom lenses. The camera arm also is perpendicular to the flat object. This choice of angle in combination with the laser interferometer enables the system to capture more light for laser interferometer. The moiré part also benefits from this configuration since for a flat object all the regions of the object have the same distance from the camera therefore there is no need to compensate for different distances, which results in different magnification.

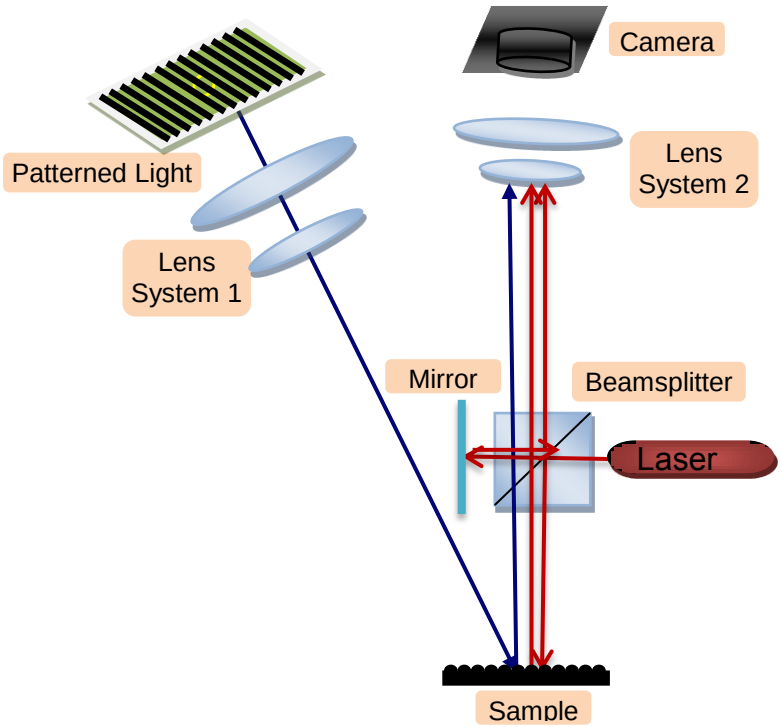

Figure 30: Schematic of the dual moiré laser interferometer

Another benefit of this configuration is the enhancement in the combination of field of view and range of depth measurement. The zoom lenses have specific depth of focus for each zoom level; when the camera arm is not perpendicular to the flat object, different points of the object have different distance from the zoom lens. This means that the field of view cannot be arbitrary large since the points out of a specific field of view lie outside the depth of focus of the zoom lens. Therefore there is a tradeoff between the angle of the camera arm, field of view and depth of focus. On the other hand, when the camera arm is perpendicular for a flat object all the points on the object have the same distance from the zoom lens and therefore there is no limit for the field of view imposed by the limited depth of focus. Likewise, when the object is not flat, the limitation for the system with perpendicular camera arm is less compared to the system with angled camera arm.

Figure 31 shows the implemented system. The lens system in the projector arm consists

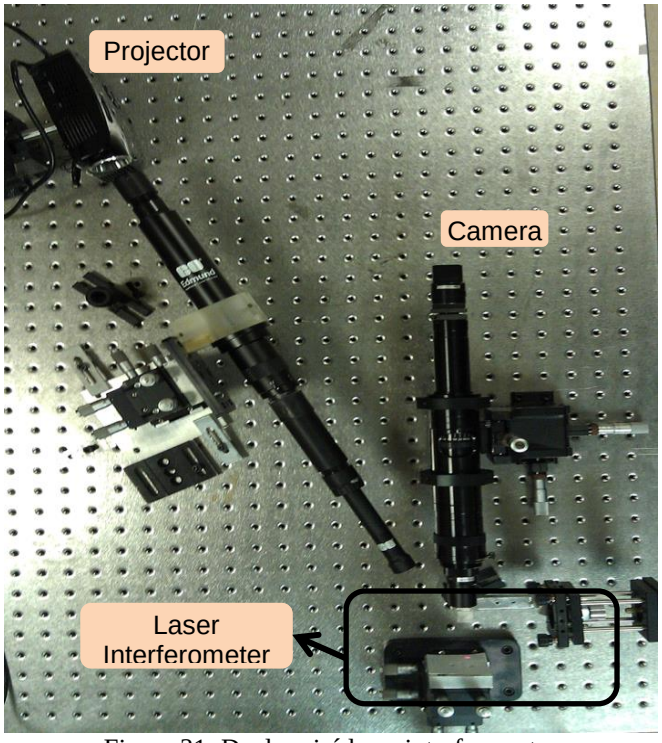

Figure 31: Dual moiré laser interferometer

Table 1: Specification of VZM 450 Zoom Imaging lens

Primary Magnification	**Minimum: 0.7X**	**Maximum: 4.5X**
FOV (1/2" CCD, Horizontal)	8.8mm	1.4mm
Resolution in Object Space	30 lp/mm	144 lp/mm
Resolution in Image Space	41 lp/mm	32 lp/mm
Working Distance (±3mm)	90mm	90mm

Table 2: Specification of 1x compact telecentric lens

Magnification	**1X**
FOV (1/2" CCD, Horizontal)	6.4mm
Aperture (f/#)	20.9
Numerical Aperture	0.019
Distortion (%)	<0.2
Telecentricity (°)	<0.2
Working Distance (±1mm)	89mm

of a single lens, a zoom lens and a telecentric lens. Zoom lens is a VZM 450 Zoom Imaging Lens[12]. The telecentric lens is a 1X compact telecentric Lens, with 110mm Working Distance[13]. The specification of the VZM 450 zoom lens and telecentric lens is given in Table 1 and Table 2, respectively. The optical system of the camera arm has two different configurations. The first configuration consists of a zoom lens and an optional objective lens. The objective lens is a Mitutoyo M Plan Apo 5x objective lens[14] and the zoom lens is 12.5x Precision Zoom Lens[15]. The specification of the objective lens and precision zoom lens are shown in Table 3 and Table 4, accordingly. The second configuration includes VZM 450 Zoom Imaging Lens and 12.5x Precision Zoom Lens.

The laser interferometer is shown in Figure 32. Laser source for laser interferometer

[12] http://www.edmundoptics.com/imaging/imaging-lenses/zoom-lenses/vzm-zoom-imaging-lenses/3280

[13] http://www.edmundoptics.com/imaging/imaging-lenses/edmund-optics-designed-lenses/compact-telecentric-lenses/3146?dc&PageNum=2#products

[14] http://www.edmundoptics.com/imaging/imaging-lenses/fixed-magnification-lenses/mitutoyo-infinity-corrected-long-working-distance-objectives/1942

[15] http://www.edmundoptics.com/imaging/imaging-lenses/zoom-lenses/12-5x-precision-zoom-lens/2872

Table 3: Specification of 5X Mitutoyo Plan Apo Infinity-Corrected Long WD objective

Magnification	5X
FOV (1/2" CCD) (mm)	1.28 x 0.96
Focal Length (mm)	40
Resolving Power (µm)	2.0
Numerical Aperture	0.14
Depth of Focus (µm)	14.0
Telecentricity (°)	<0.2
Working Distance	34.0mm

Table 4: Specification of 12.5x Precision Zoom Lens

Primary Magnification	Minimum: 1X	Maximum: 13X
FOV (1/2" CCD, Horizontal)	6.4mm	0.49mm
Resolution in Object Space	57 lp/mm	300 lp/mm
Numerical Aperture	0.019	0.10
Working Distance	89mm	89mm
Depth of Field	0.78mm	0.028mm

is delivered using a single mode optical fiber. A lens in front of the fiber makes the laser beam collimated. The laser interferometer has a Michelson configuration.

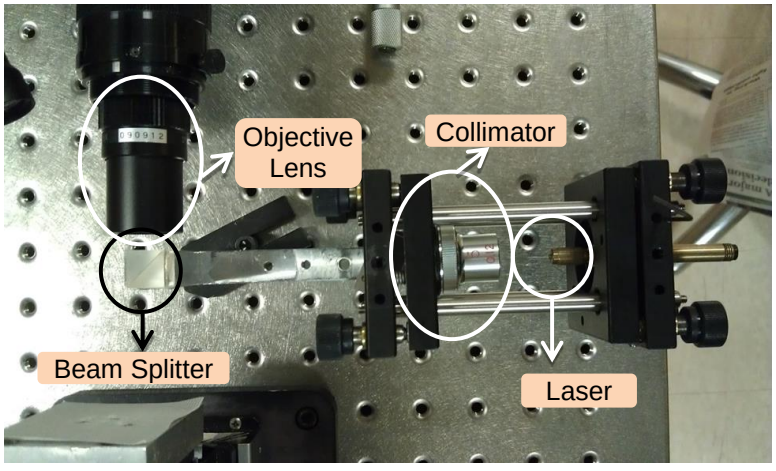

Figure 32: Laser interferometer

3.2. Simulation

To evaluate the system, both fringe projection and laser interferometer were simulated in MATLAB™ environment. For fringe projection, the effect of finite resolution of camera was considered and the interferogram was generated. Moiré simulation was performed using ray-tracing technique. The ray-tracing can be done by tracing from the light source to the camera pixels or tracing the rays from each pixel of camera back to the light source. We simulated both methods and the results of simulations happened to be the same. Although for non-flat object, the backward tracing (tracing the rays from camera plane back to the light source) needs less time. Therefore we use backward tracing. Figure 33 shows the universal coordinate system and coordinate of the center of the object (X_b, Y_b), center of the camera $(X_{0Camera}, Y_{0Camera})$ and the center of the light source and grating $(X_{0Grating}, Y_{0Grating})$ used for the simulation of the moiré system.

The effect of electronics noise was also considered in moiré simulation. For laser interferometer, the effect of noise and speckle were considered.

Laser interferometer was modeled as having the following output signal,

$$I(r,t) \approx I_0[1 + V\cos\delta(r)]R_s(r) + R_E(r,t) \tag{3.5}$$

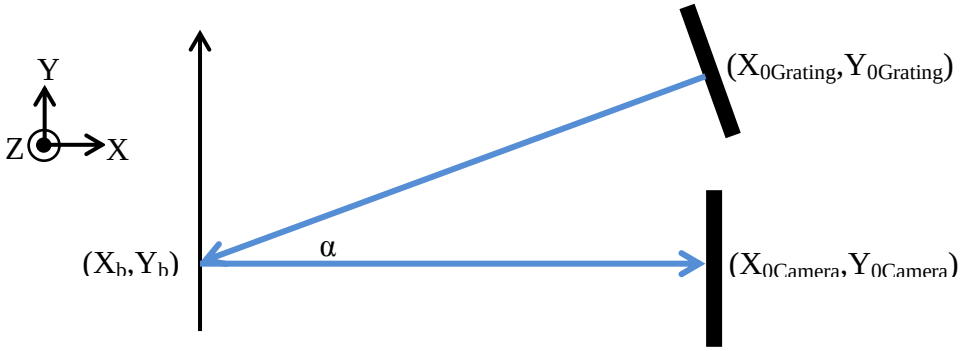

Figure 33: The coordinate and geometrical parameters for simulation of dual moiré laser interferometer

where V is fringe contrast, $\delta(r)$ is phase that corresponds to profile of the object, $R_s(r)$ is speckle noise and $R_E(r,t)$ is electronics nosie.

Parameters of simulations are as follows: speckle noise is considered as averaged exponential distribution; electronics noise is additive white Gaussian noise (AWGN) with signal to noise ratio (SNR) of 20dB and contrast was one. The angle between camera arm and projector arm is 20 degrees; camera is 512 by 512 pixels; laser wavelength is 633 nm; number of fringes at lowest zoom level for projection moiré is 51.2 and the grating pitch of moiré pattern is .1 mm.

The simulated object has both form and features. The form of the object is a circular symmetric cosine shape with amplitude of 0.2 mm and period of 2 mm. Features are also circular symmetric cosine shape with amplitude of 1 μm and period of 2 μm.

Figure 34 shows the simulated object at different levels of zoom. As it is seen at low zoom level only the form of the object is visible and when we zoom in on the object more and more, the features of the object start to appear.

Figure 35 shows the simulated interferograms for fringe projection and laser interferometer. As it is shown, at lower zoom level, which form of the object is visible, the moiré interferogram has a conventional pattern that can be used to extract the phase map and form of the object. On the other hand, the laser interferogram does not have useful information and cannot be used to extract information about the features of the object. At high zoom level (2048x), the visible features are present in the field of view of the measurement instrument and therefore laser interferogram has the features information encoded in fringe pattern. At this zoom level, moiré interferogram has no meaningful information and therefore no information can be extracted.

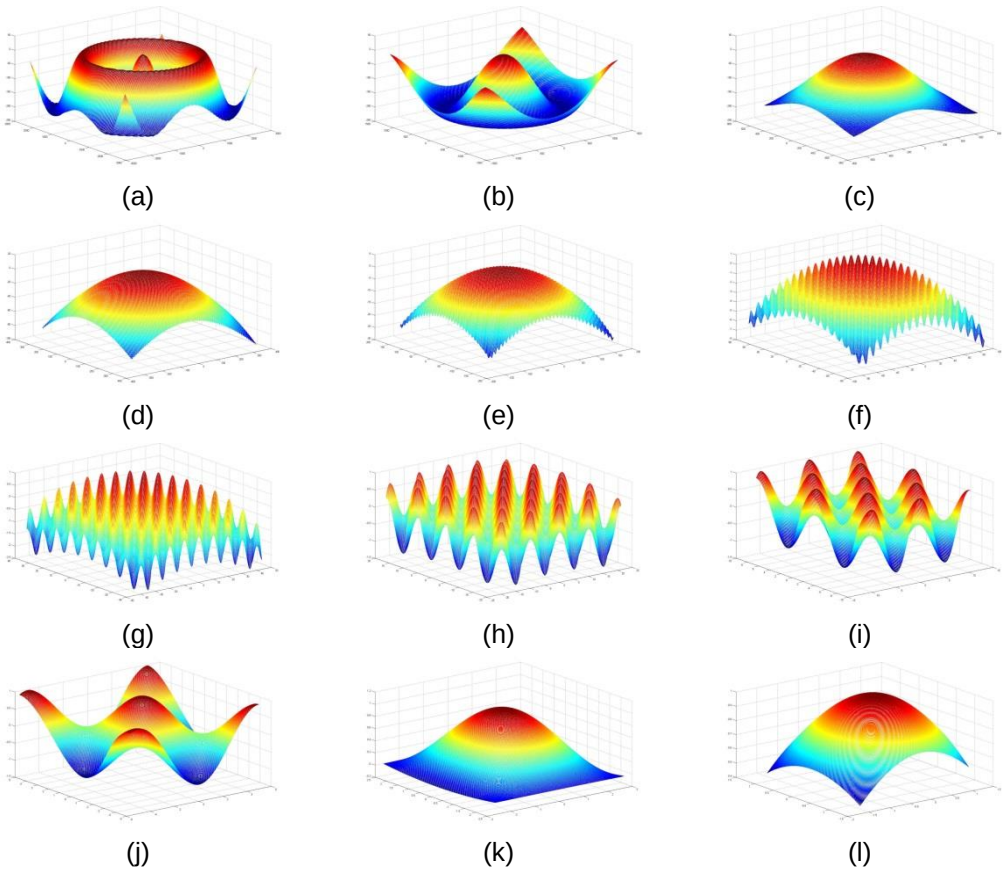

Figure 34: Simulated object at different levels of zoom (a): zoom 1x, (b): zoom 2x, (c):zoom 4x, (d):zoom 8x, (e):zoom 16x, (f):zoom 32x, (g):zoom 64x, (g):zoom 128x, (h):zoom 256x, (i):zoom 512x, (j):zoom 1024x, (k):zoom 2048x and (l):zoom 4096x.

The next step is to combine the information from different zoom levels. We have form of the object from moiré system in lower zoom level and features of the object from laser interferometer at higher zoom level. The combination is the combination of lateral information and height information. Height information is combined using data fusion techniques. But before combining height information from different zoom levels, we have to relate each pixel from one interferogram to its corresponding pixel in another interferogram at different scale (zoom level). This lateral information combination is explained in next section.

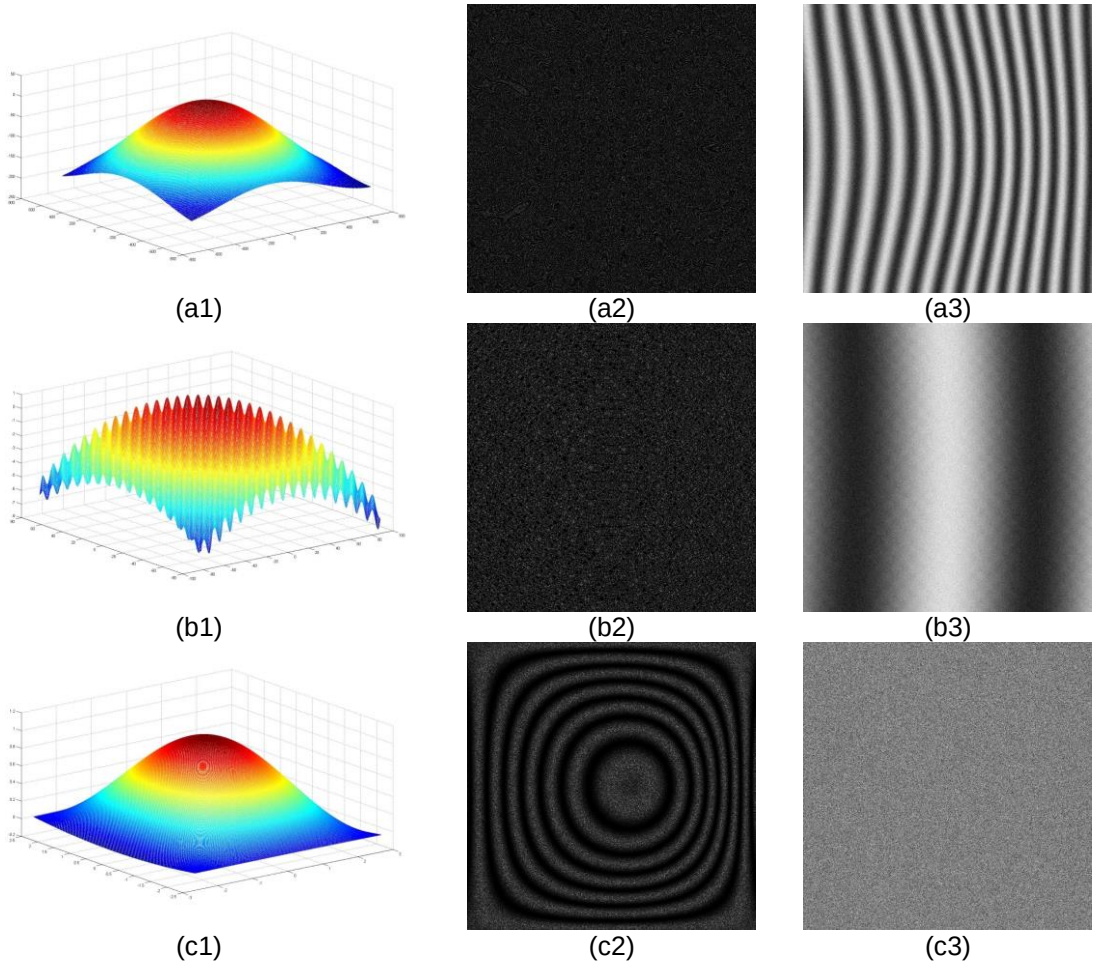

Figure 35: Simulated object and the resultant interferogram from fringe projection and laser interferometer at different levels of zoom: (a1): object at zoom 4x, (a2): laser interferogram at zoom 4x, (a3): moiré pattern at zoom 4x, (b1): object at zoom 32x, (b2): laser interferogram at zoom 32x, (b3): moiré pattern at zoom 32x, (c1): object at zoom 2048x, (c2): laser interferogram at zoom 2048x, (c3): moiré pattern at zoom 2048x.

3.3. Data Stitching

As mentioned in previous section, we need to stitch data from moiré measurement system and laser interferometer, and also from different levels of zoom.

The data to be stitched is raw or intermediate output from moiré system or laser interferometer, which are fringe patterns that are processed to extract the desired measurand. For large objects these measurement systems usually have variable magnification capabilities that are typically accomplished with a zoom lens or different

objective lenses. When reconfiguring the instrument for a measurement at a new magnification, the field of view does not necessarily stay centered and the value of the magnification (the new field of view) is only known approximately from the instrument settings. To quantitatively relate fine and coarse measurements, it is necessary to find the relative coordinates and value of the magnification with respect to a reference image that can be conveniently taken to be the measurement at the lowest magnification.. This can be accomplished using image registration.

3.3.1. Image Registration

Image registration is a technique to align two images from one scene [91]. These images can be taken with two different instruments, from two different angles, with two different levels of zoom, or at different times. One image is referred to as the reference image and the other one is the target image [91]. Mathematically speaking, the reference image (R) and the target image (T) belong to sets of d-dimensional images with $d = 2$; i.e. $R, T \in Img(d = 2) \coloneqq \{b: \mathbb{R}^2 \to \mathbb{R} \,|b\ is\ 2 - dimensional\ image\}$. Image registration aligns the target image with the reference image by transforming the target image and minimizes the difference (or maximize the similarity) between the target and reference images

To summarize, the problem of 2-d image registration can be stated as follows [92]: Given a distance measure $\mathcal{D}: Img(d)^2 \to \mathbb{R}$ and two images $R, T \in img(d)$, find a mapping $\varphi: \mathbb{R}^d \to \mathbb{R}^d$ and a mapping $g: \mathbb{R} \to \mathbb{R}$ such that $\mathcal{D}\left(R, g\left(T\left(\varphi(v)\right)\right)\right)$ is minimum.

The transformation of the target image can be rigid or non-rigid. The rigid transformation preserves the distance between two points. Rigid transformation includes

rotation, translation and reflection. The rigid transformation essentially preserves size and shape of the image. The non-rigid transformation, on the other hand, includes any deformation that does not preserve the shape and the size of the reference image.

Another important class of transformation is the affine transformation. Affine transformation preserves the straight lines and the ratio of distances on a straight line. Therefore all rigid transformations are affine transformation. Scale (expansion and contraction) and shear are two other transformations classified as affine transformation.

Image registration can also be classified as parametric or non-parametric [92]. Generally, there are three approaches for the parametric image registration, which are landmark-based registration [93], [94], [95], [96], principal axes-based registration [97], [98], [99] and optimal linear registration [100], [101], [102], [103].

In landmark-based registration, some features of the image, which are referred as landmarks, are registered. The landmarks are the features that are pronounced and therefore can be located easily. The landmarks are usually identified manually and image registration tries to map the landmarks of target image to corresponding landmarks of reference image in a way that the difference between transformed target image and reference image is minimum. Since we need to identify and locate the landmarks for registration, the process is not fully automatic and therefore this technique is not suitable for fully automatic processes.

The principal axes-based registration uses the features that are derived from the image itself (e.g. edges, corners). Those extracted features are called principal axes. Like landmark-based registration the target image is transformed such that the distance between the features (principal axes) of the target image and reference image is

minimum. Although this technique is fast and automatic, it is not suitable for multimodal images. The reason is that the images from same subject that are taken with different instruments have different features and therefore they cannot be matched.

The optimal linear registration minimizes a distance measure (or maximize similarity measure) using a linear transformation. The distance (similarity) measure is used to quantify the difference (or similarity) of two images. Considering similarity, the similarity measure can be based on intensity of images [103], [104], [105] , correlation between images [100], mutual information between images [106], [107], or other measures.

The intensity-based measures are the measures that are based on the intensity itself. The simplest intensity-based measure is the difference measure, which simply measures the difference between intensity of the images. This measure is defined as:

$$\mathfrak{D} = \left\| I_R(v) - I_{T\circ\varphi}(v) \right\|_p \tag{3.6}$$

which measures the norm p distance between intensity of reference image and transformed target image.

The correlation measure maximizes the correlation between the reference image and transformed target image and is defined as:

$$\mathfrak{D} = corr\left(I_R, I_{T\circ\varphi}\right) = \sum_v \left(I_R(v) - \bar{I}_R(v)\right)\left(I_{T\circ\varphi}(v) - \bar{I}_{T\circ\varphi}(v)\right) \tag{3.7}$$

where $\bar{I}(.)$ Is the average of $I(.)$.

As it is seen the correlation measure directly depends on the intensity of the images. The reference and target image might have different intensities, which affect the correlation measure. To reduce this effect, it is better to normalize the intensity of both

images as a preprocessing step. The normalization can be done on the amplitude of the images or the mean value of the intensity of the images.

Gradient measure is another distance measure, which works on the gradient of images. Instead of calculating the correlation between the images' intensities, the correlation is taken between the intensity gradients of images.

$$\mathfrak{D} = corr\left(\frac{dI_R}{dx}, \frac{dI_{T\circ\varphi}}{dx}\right) + corr\left(\frac{dI_R}{dy}, \frac{dI_{T\circ\varphi}}{dy}\right) \tag{3.8}$$

where dI/dx and dI/dy are the derivative in x-direction y-direction respectively.

Since the gradient measure uses the derivative in x and y directions, it is sensitive to the edges.

The mutual information similarity measures mutual information between intensity of two images. Assuming two images R and T, then the mutual information similarity measure is defined as

$$\mathfrak{D} = \mathcal{I}(p_R, p_T) = \sum_{r,t} p_{R,T}(r,t) log \frac{p_{R,T}(r,t)}{p_R(r)p_T(t)} \tag{3.9}$$

where $p_R(r)$ and $p_T(t)$ are the probability density functions of intensity of images R and T; and $p_{R,T}(r,t)$ is the joint probability density function of intensity of images R and T.

For a reference image and transformed target image (assuming $g(x) = x$) the mutual information distance is defined as

$$\mathfrak{D} = \mathcal{I}\left(p_R, p_{T\circ\varphi}\right) \tag{3.10}$$

where $T \circ \varphi(v) = T\left(\varphi(v)\right)$.

Mutual information measure is a good measure for images taken with different imaging devices (e.g. CAT and MRI).

The similarity measure used in this work is pattern intensity [108]. The pattern intensity measure for two images *R* and *T* is defined as

$$\mathfrak{D} = P_{r,\sigma}(\lambda) = \sum_{i,j} \sum_{d^2 \le r^2} \frac{\sigma^2}{\sigma^2 + \left(I_{dif}(i,j) - I_{dif}(v,w)\right)^2}, \quad d^2 = (i-v)^2 + (j-w)^2 \tag{3.11}$$

where $I_{dif} = I_R - \lambda I_{T \circ \varphi}$ and $\varphi(x,y)$ is the transformation of the coordinates of the image $I(x,y)$.

The pattern intensity operates on the difference between images. The average intensity of the captured fringe patterns at different zoom levels are different, and this is compensated for by multiplying one fringe pattern with parameter λ and making the average intensity of both images equal. Parameter *r* determines the radius inside of which the difference comparison (calculation) is made. The parameter σ determines the sharpness of the similarity measure. Smaller σ means more sensitivity to the pixel differences and therefore a sharper similarity curve versus the difference between pixels. In our calculations values of $\sigma = 10$ and $r = 5$ provide the best results for image registration of fringe patterns. The function φ is the transformation of the coordinates of the image.

As mentioned above, there are different transformations used to implement image registration [109], [110], [111]. In the case of changing the zoom level, the transformation is dominated by translation and scaling only, so an affine transformation is sufficient to register the images.

The affine transformation used here is defined by $\varphi(x) = Ax + b, \ A \in \mathbb{R}^{d \times d} \varphi(\mathrm{x}) = \mathrm{Ax} + \mathrm{b}, \mathrm{A} \in \mathrm{R}^{\mathrm{d} \times \mathrm{d}}$ with $\det(A) > 0, b \in \mathbb{R}^d$ [92] where $\det(A)$ is determinant of matrix

A. For the case of 2-d image transformation that includes translation and scaling, the transformation can be defined as

$$\varphi\left(\begin{bmatrix} x \\ y \end{bmatrix}\right) = \begin{bmatrix} s_x & 0 \\ 0 & s_y \end{bmatrix}\begin{bmatrix} x \\ y \end{bmatrix} + \begin{bmatrix} t_x \\ t_y \end{bmatrix}$$

To summarize, in this work the distance measure (similarity measure) is pattern intensity, transformation is an affine transformation with 2-d images of fringe patterns, and $g(x) = x$.

For resampling and interpolation we chose to use linear interpolation since it is simple and works for the fringe patterns as input images.

The optimization that is used to find the parameters is a nonlinear least squares optimization that implements trust-region-reflective algorithm, and Levenberg-Marquardt algorithm. The optimization belongs to the optimization toolbox of the MATLAB.

3.3.2. Data Stitching Algorithm

Figure 36 shows the flowchart for the algorithm to stitch the interferograms from fringe projection and laser interferometers at different zoom levels, and calculate the location of all acquired interferograms relative to a reference point on object. First an image is acquired at the lowest zoom level using fringe projection. Then more interferograms are acquired using both fringe projection and laser interferometer by zooming in on regions of interest. Using our technique, the exact zoom level change (scale) and shift in lateral directions (translation in x and y axis) will be calculated. Therefore the coordinate of each point at any interferogram is available relative to a reference point on first interferogram at the lowest zoom level.

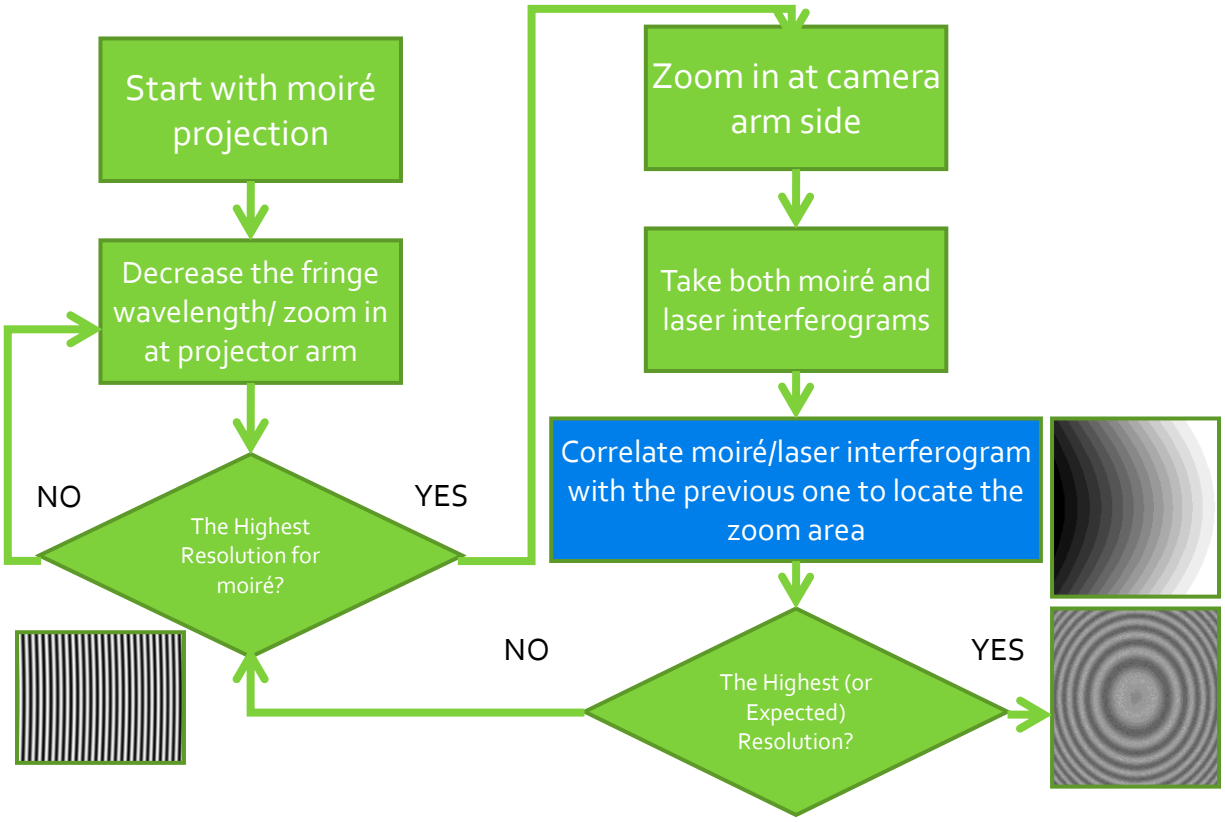

Figure 36: Stitching algorithm

We applied the algorithm first to the simulated moiré fringe patterns. Figure 37 shows the results of applying the proposed algorithm to the moiré fringe patterns at zoom levels

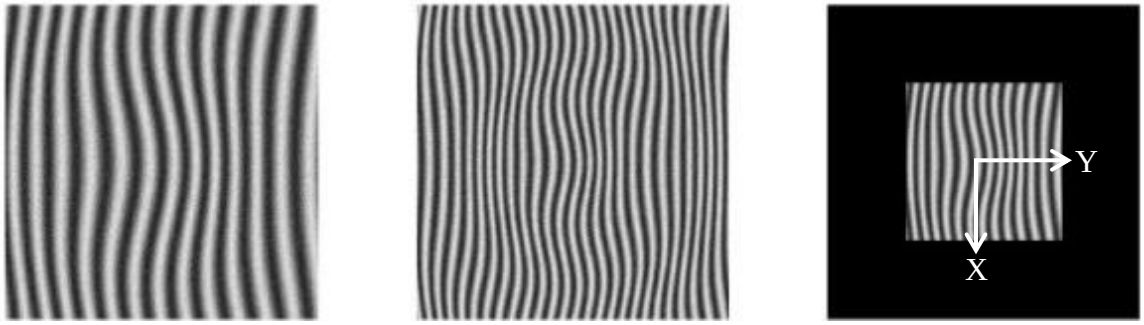

(a) (b) (c)

Figure 37: Results of image registration to determine the shift and scale in both x and y directions at different levels of zoom. Images (a) and (b) are simulated moiré fringe patterns from the fringe projection moiré system at zoom levels of 2 and 1, and without any shift of the center of the images. Image (c) is the scaled and translated version of (a) and it is located with respect to the coordinate system of image (b).

Table 5: Scale (change of zoom level in X and Y directions) and translation (shift in X and Y directions) values for moiré fringe patterns at zoom levels 1x and 2x (Figure 37).

X-Translation (Pixels)	Y-Translation (Pixels)	X-Scale	Y-Scale
0.5	-1.6	1.998	1.999

one and two. The center of the images are kept fixed, which results in the zero translation in both X and Y directions. The results of the algorithm are shown in Figure 37.c and Table 5. As it is seen the algorithm shows 0.5 pixel shift in X direction and 1.6 pixel shift in Y direction. The scale in X direction is given as 1.998 and in Y direction is calculated as 1.999. Considering the 512x512 resolution of the images, the result shows that the algorithm can achieve pixel resolution for data stitching.

In next step the algorithm was applied to the laser interferograms. Figure 38 shows the results for the laser interferograms acquired at zoom levels 256 and 512. As it is seen in Table 6, the algorithm shows shifts of 0.5 and 0.4 pixels in X and Y directions respectively and zoom change of 1.999 in both X and Y directions. Therefore the algorithm is able to find shift and scale of fringe patterns (acquired from both moiré and laser interferometer) within a pixel resolution.

Since only one camera is used for acquiring interferograms from both fringe projection and laser interferometer, the pixels of acquired interferograms from fringe projection and laser interferometer correspond to each other (assuming that the camera is focused on the object and the region of the interest of the object is within the field of the view of both laser interferometer and the moiré system at that specific zoom level). Therefore in a specific zoom level, switching from fringe projection to laser interferometer (or vice

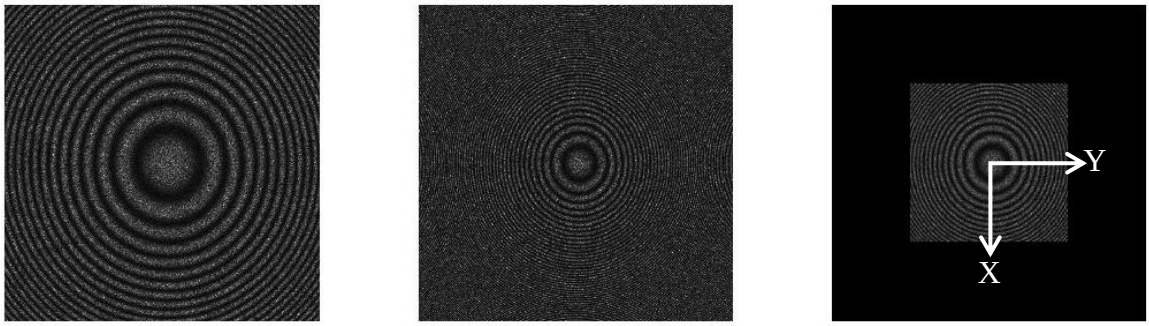

(a) (b) (c)

Figure 38: Results of image registration to determine the shift and scale in both x and y directions at different levels of zoom. Images (a) and (b) are simulated laser interferograms from the laser interferometer system at zoom levels of 512 and 256, and without any shift of the center of the images. Image (c) is the scaled and translated version of (a) and it is located with respect to the coordinate system of image (b).

Table 6: Scale (change of zoom level in X and Y directions) and translation (shift in X and Y directions) values for laser interferograms at zoom levels 1x and 2x (Figure 38)

X-Translation (Pixels)	Y-Translation (Pixels)	X-Scale	Y-Scale
0.5	0.4	1.999	1.999

versa) does not require further calculations to correspond pixel coordinates of their interferograms.

3.4. Fringe Pattern Analysis Software

The raw output of both moiré system and laser interferometer is interferograms (fringe pattern). These data need to be analyzed to extract the parameter of interest (e.g. the height information). The commercial fringe analysis softwares usually require interferograms that are taken from specific interferometers and/or with specific techniques. Since we developed both moiré system and laser interferometer and wanted to have freedom in designing and configuration of the system, we decided to develop our own fringe analysis software

The first step in the fringe pattern analysis is the preprocessing that includes masking, brightness adjustment, filtering, etc. After preprocessing the fringe pattern, the phase map

is calculated from the fringe pattern. As mentioned in the previous chapter, there are different techniques to calculate the phase map from the fringe pattern including fringe counting, Fourier analysis, wavelet analysis, short time Fourier analysis, etc. We examined Fourier analysis, short time Fourier analysis and wavelet analysis. For our fringe patterns, all the methods have comparable performance. Although the Fourier analysis needs less computation and therefore is faster compared to other techniques; therefore we chose the Fourier analysis to calculate the phase map.

The phase map that is calculated from fringe patterns is a wrapped phase. This means that the value of the phase is between 0 and 2π (or $-\pi$ and $+\pi$). Therefore there is an ambiguity of $2k\pi$ in phase for each pixel where k is an integer. There are different methods to remove this ambiguity and find the unwrapped phase which were explained in the previous chapter. As mentioned there, we chose to use quality guided method for unwrapping the phase and the magnitude of short time Fourier transform of the complex value of the phase map is used as the quality criterion. Figure 39 shows different steps in the implemented software. Figure 39.a is the fringe pattern. For filtering the fringe pattern, the software first find the carrier frequency (main frequency) of the fringe pattern. Then a band pass Hanning filter centered at the carrier frequency is used to filter out the noise. The bandwidth of the Hanning filter is chosen to include all necessary information and to remove the noise as much as possible. Figure 39.b shows the Hanning filter corresponds to the interferogram.

For calculating the phase map, software needs a reference fringe pattern (fringe pattern from a flat surface). If the reference pattern is not provided, the software virtually makes a reference fringe pattern based on the carrier frequency of the acquired fringe

pattern. Figure 39.c shows the wrapped phase map which calculated without the reference interferogram. The next step is to unwrap the wrapped phase map. Therefore, software calculates the short time Fourier transform for each pixel of the wrapped phase map. The magnitude of the short time Fourier transform is used as the quality map for unwrapping the calculated wrapped phase. The software then uses the quality map to unwrap the phase map. Figure 39.d shows the unwrapped phase map. As it is seen the unwrapped phase map has a tilt. The tilt can be removed by calculating the amount of the tilt and subtracting a tilted plane from the unwrapped phase map. Figure 39.e shows the unwrapped phase when the tilt is removed. Multiplying the unwrapped phase map with

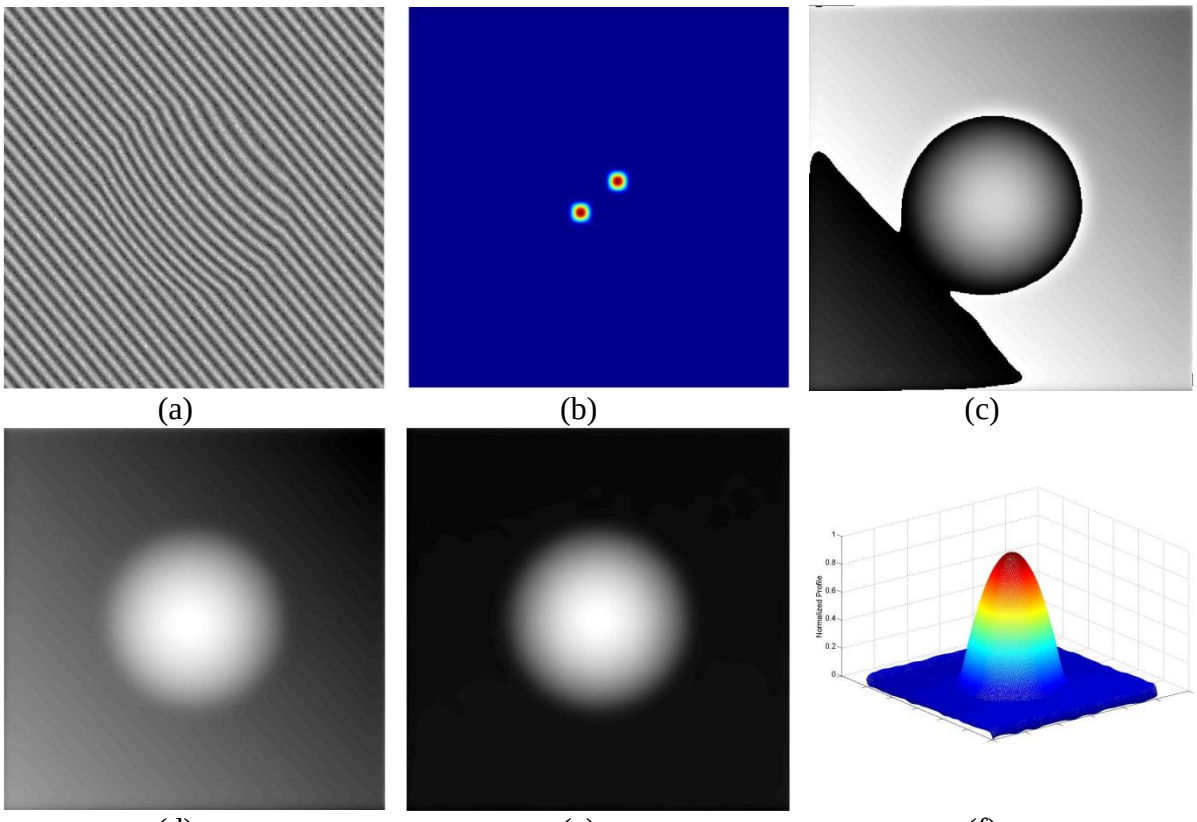

Figure 39: Inputs and outputs of the fringe analysis. (a): interferogram, (b): Hanning filter in which the central frequency is the same as the carrier frequency of the interferogram, (c): wrapped phase map, (d): unwrapped phase map, (e): unwrapped phase with removed tilt, and (f): the normalized profile of the object

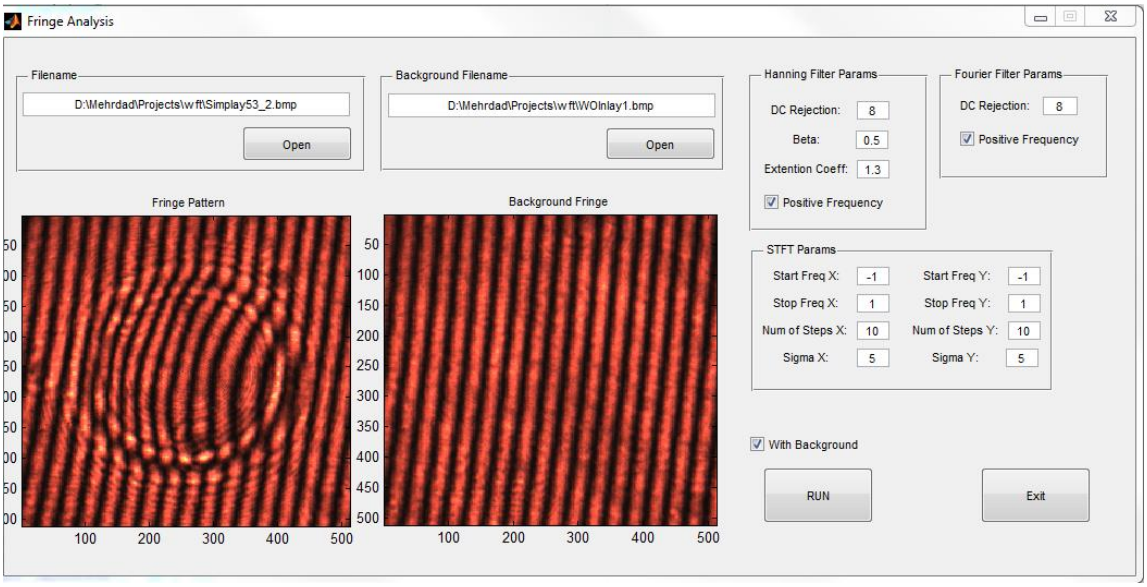

Figure 40: Fringe analysis software

the wavelength and dividing it by 2π gives the profile of the object (Figure 39.f). Figure 40 shows the GUI of the software developed in MATLAB. As it is seen the user can control the parameters for Hanning filter and for the short time Fourier transform.

Figure 41 shows the results of the software for fringe patterns captured from moiré system and laser interferometer. For laser interferogram a reference interferogram is provided and therefore the software uses that interferogram as a reference. For moiré fringe pattern, the reference interferogram is not available and therefore the software generates a reference from the moiré fringe pattern itself.

The fringe analysis software could be improved in terms of speed, performance and ability to analyze different fringe patterns, which each of them can be the topic of an

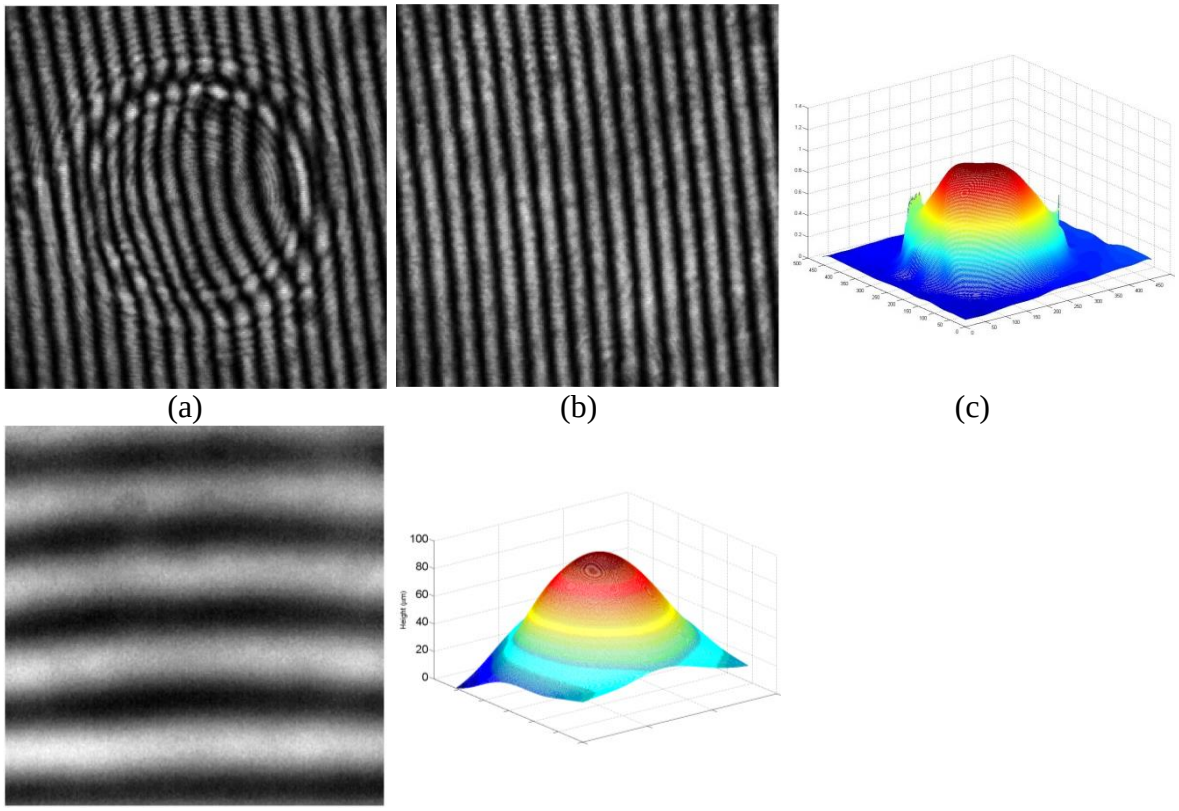

Figure 41: Fringe analysis for moiré and laser interferograms. (a): laser interferogram for a microlens (b): corresponding reference interferogram, (c): calculated profile by fringe analysis software, (d): moiré interferogram from a bump artifact, and (e): calculated profile by fringe analysis software.

independent research. The focus of this work was on other parts of the system including hardware development and stitching the data acquired from moiré and laser interferometer and also from different levels of the zoom. Fringe analysis software was developed in order to enable us to demonstrate the results not only in the form of fringe patterns, but in the form of the profile of the object.

3.5. Experiment

After completing the hardware development and verifying that the proposed algorithm can be used for stitching the interferograms, we applied the technique to the interferograms acquired form moiré and laser interferometer. For laser interferometer, the

wavelength is the wavelength of the He-Ne laser (632.8 nm); for the moiré system the equivalent wavelength depends on the pitch of the grating (period of fringe patterns) and the configuration of the system. To measure the equivalent wavelength experimentally, we adopted the technique in [112]. In this technique, the equivalent wavelength is calculated regionally and for each pixel. To do this, we used a flat surface as the object and changed the distance of the object incrementally. For each incremental change we acquired the fringe pattern. As the object moves, the fringe patterns also moves. By looking at one pixel, we observed that the change of the intensity follows a sinusoidal function (Figure 42). The amount of movement that corresponds to the period of this sinusoidal function is the equivalent wavelength for that pixel. In other words, the displacement of the object that causes the fringe pattern to move one period is the equivalent wavelength. For the experiment, the incremental displacement was 25.4 μm. We captured 180 fringe patterns and extracted the intensity changes for each pixel. Then

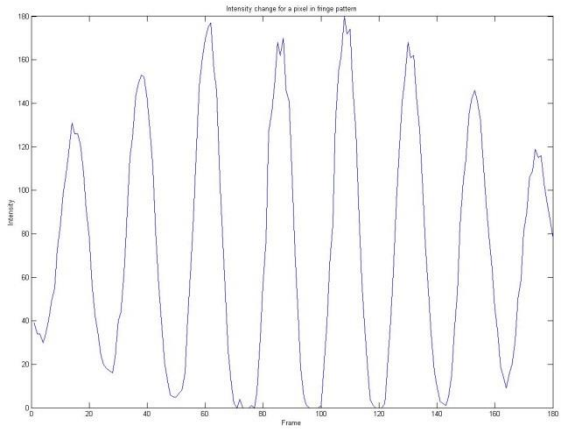

Figure 42: The change of intensity for a typical pixel of the captured fringe pattern in terms of the flat object displacement.

a sinusoidal function was fitted to the intensity of each pixel to calculate the equivalent wavelength of the moiré system for that pixel. The change of the equivalent wavelength from one pixel to another depends on the configuration of the moiré system (e.g. the angle of the projector arm and camera arm) and the quality of the optical component (e.g. zoom lenses and telecentric lens). Figure 43 shows the map of the equivalent wavelength when the zoom level at the projector arm is 1 and zoom level at the camera arm is one. As it is seen the equivalent wavelength is changing between 572 µm and 586 µm. Note that to change the equivalent wavelength we either can change the zoom level of the projector arm or change the period of fringe pattern in software. Changing the zoom level at camera arm does not change the equivalent wavelength. Although, for each zoom level of camera arm, we have to scale the equivalent wavelength map to find the corresponding map for the pixels at new zoom level.

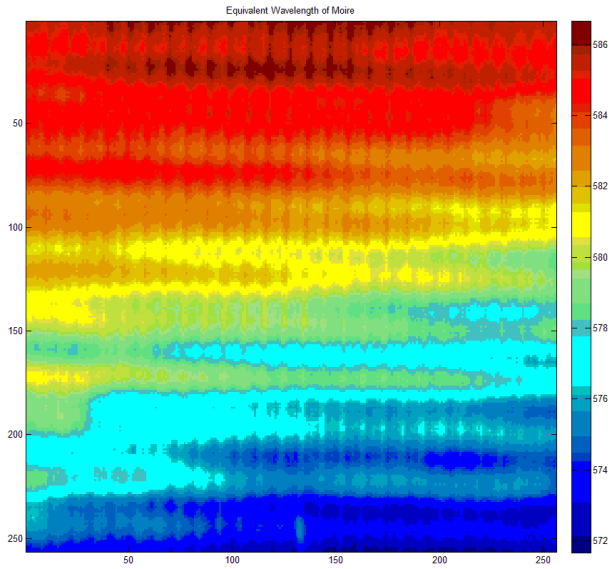

Figure 43: Equivalent wavelength map for moiré system at zoom level one for both projector arm and camera arm.

As mentioned before, fringe projection is used for coarse measurement (form of the object). This is done to generally inspect the whole area of the object and to find the regions of interest. The first object that was measured using moiré system was a bump artifact (Figure 44). Using this object, we captured the moiré patterns at zoom levels 1x, 1.5x, 2x, 2.5x, and 3x (on camera arm). Figure 45 shows the captured fringe patterns along with their corresponding reference fringe patterns. Since the change in zoom level is done manually, the numbers that are given as the level of zoom (e.g. 1.5x) are approximate. Our stitching algorithm finds the exact change in zoom level based on image registration technique. Another problem is the misalignment of optical axes of optical elements. Since the optical axes of our optical elements (e.g. zoom lenses) are not perfectly aligned, by changing the zoom level, the center of the image shifts. Another reason for shift in the center of the image is the fact that we might deliberately change the position of the center of the object (e.g. using the stage that the object is placed on) to

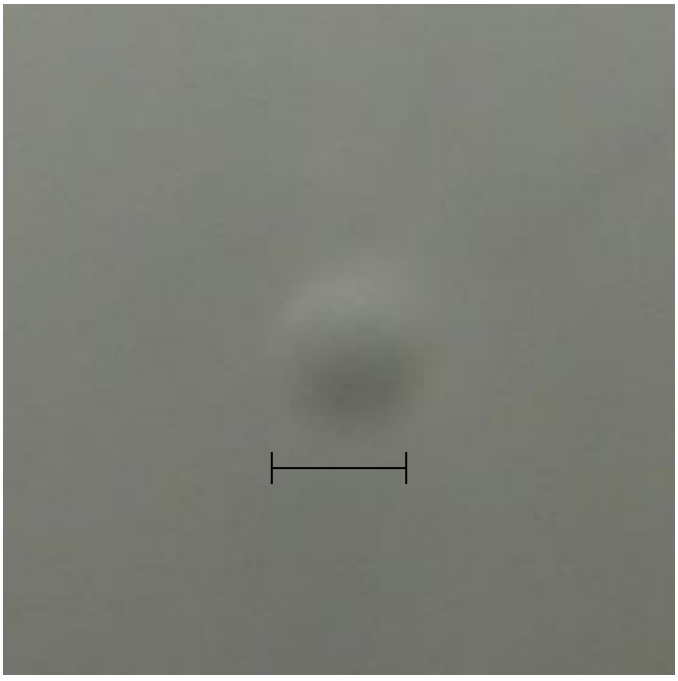

Figure 44: Bump artifact as the object

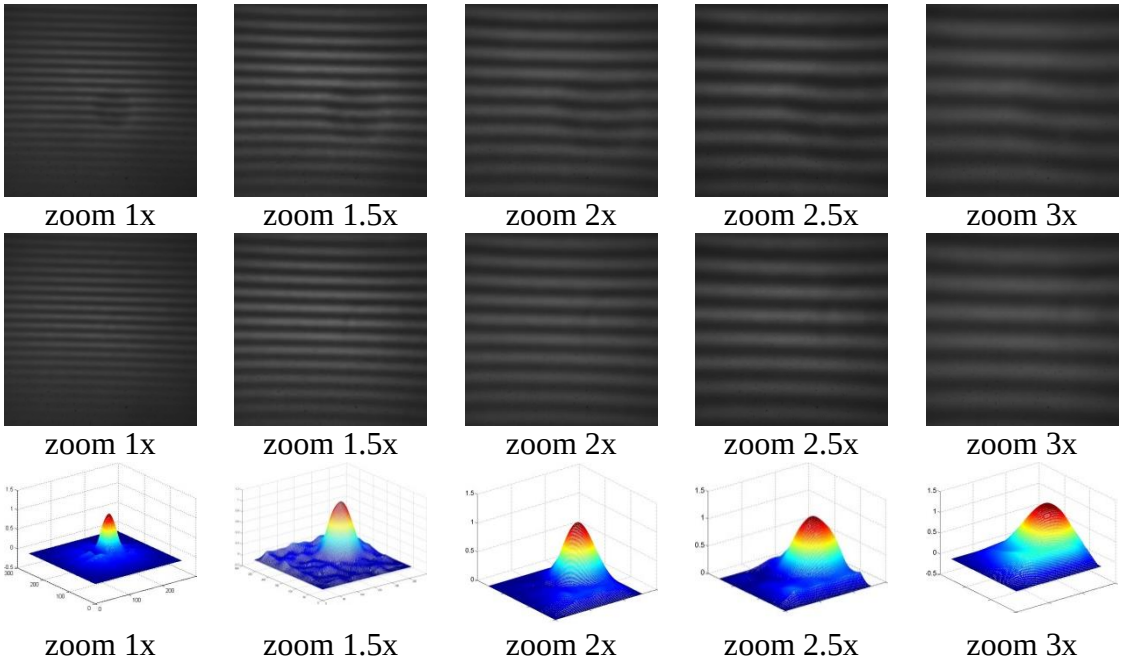

Figure 45: Deformed and reference fringe patterns from a bump artifact. The first row shows the deformed fringe patterns from a bump artifact at zoom levels of 1x, 1.5x, 2x, 2.5x and 3x. The second row is the reference fringe patterns at the corresponding zoom levels. The third row is the profile of the artifact at the corresponding zoom levels.

look at different regions of the object, therefore we need to know the exact amount of the shift in order to stitch the images at different levels of the zoom. This is also done using our algorithm.

The next step is to find the location of the fringe patterns at higher zoom level with respect to the fringe pattern with lower zoom level. As mentioned before, our approach for this problem is using image registration technique, which is shown, by simulation, to be a reliable method for both moiré and laser interferograms. We chose the fringe patterns at zoom levels 1x, 2x and 3x and first find the location of the fringe pattern with zoom level 2x with respect to fringe pattern with zoom level 1x. Figure 46 and the corresponding Table 7 show the result of image registration for fringe patterns at zoom level 1x and 2x. Figure 46.a shows the fringe pattern with higher zoom level (2x),

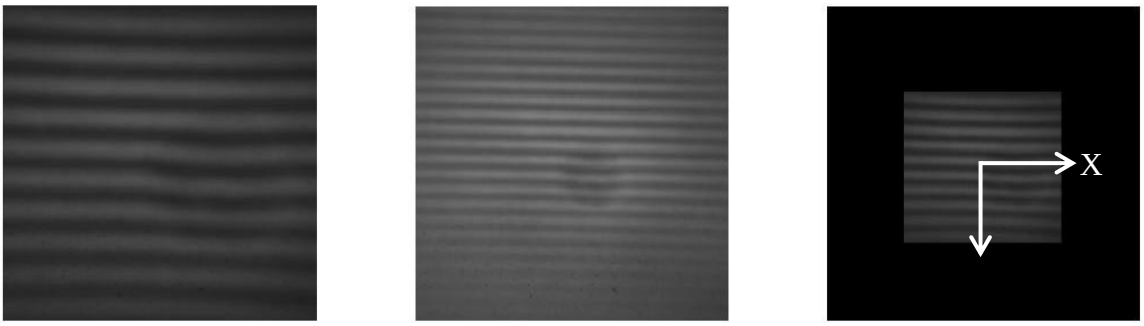

(a) (b) (c)

Figure 46: Finding the location of fringe pattern at zoom level 2x (a) with respect to fringe pattern with zoom level 1x (b). (c) shows the scaled and transferred fringe pattern at zoom level 2x at the coordinate of fringe pattern with zoom level 1x.

Table 7: Scale (change of zoom level in X and Y directions) and translation (shift in X and Y directions) values for fringe patterns at zoom levels 1x and 2x (Figure 46).

X-Translation (Pixels)	**Y-Translation (Pixels)**	**X-Scale**	**Y-Scale**
6.1	2.0	2.091	1.992

Figure 46.b shows the fringe pattern with lower zoom level (1x), and Figure 46.c shows the scaled and translated fringe pattern with higher zoom level (2x) in the coordinate of the fringe pattern with lower zoom level (1x). As it is given in Table 7, the shift in X direction is 6.1 pixels, and in Y direction is 2.0 pixels. Note that the positive X direction is vertical and downward, and the positive Y direction is horizontal and to the right. The scale in X direction is 2.091 and and in Y direction is 1.992. Note that the scale is with respect to the center of the image. The inequality in scale in X and Y directions comes from the imperfection of the optical elements. For example, aberration of lens (e.g. astigmatism, barrel and pincushion distortions) results in different magnifications at different points of the field of view of the lens. Therefore, going from one zoom level to another zoom level can cause different change of zoom levels at different directions.

The next step is to register fringe pattern with zoom level 3x with respect to the fringe pattern with zoom level 2x. As it was demonstrated in Figure 47 and

Table 8, image registration technique registers the fringe pattern with zoom level 3x with respect to fringe pattern with zoom level 2x. As in

Table 8, the shift in X and Y directions is -2.4 and -0.1 respectively, and the scale in X and Y directions is 1.526 and 1.500, correspondingly.

The relationship between coordinate at the higher zoom level (x_{hz}, y_{hz}) and the lower zoom level (x_{lz}, y_{lz}) can be written as:

$$\begin{cases} x_{hz} = a_x x_{lz} + x_0 \\ y_{hz} = a_y y_{lz} + y_0 \end{cases} \quad (3.12)$$

where a_x and a_y are the scale in X and Y directions, and x_0 and y_0 are the translation in X and Y directions. Therefore the coordinate of the image at higher zoom level can be

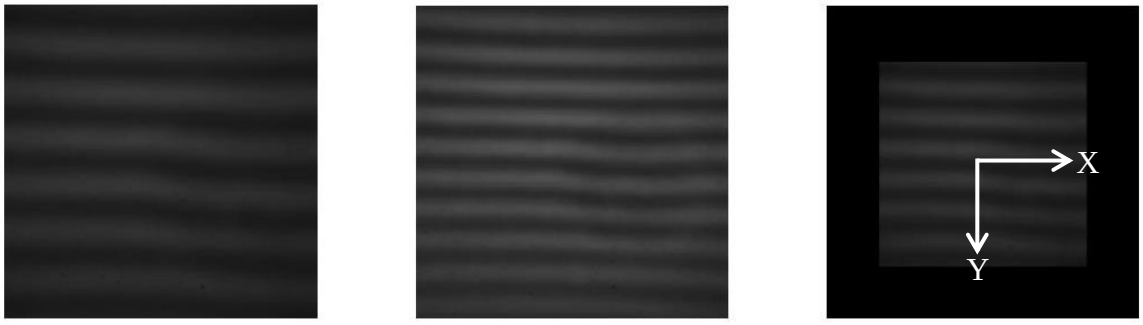

(a) (b) (c)

Figure 47: Finding the location of fringe pattern at zoom level 3x (a) with respect to fringe pattern with zoom level 2x (b). (c) shows the scaled and transferred fringe pattern at zoom level 3x at the coordinate of fringe pattern with zoom level 2x.

Table 8: Scale (change of zoom level in X and Y directions) and translation (shift in X and Y directions) values for fringe patterns at zoom levels 1x and 2x (Figure 47).

X-Translation (Pixels)	Y-Translation (Pixels)	X-Scale	Y-Scale
-2.4	-0.1	1.526	1.500

written in terms of the coordinate in lower zoom level as:

$$\begin{cases} x_{lz} = \dfrac{1}{a_x}(x_{hz} - x_0) \\ y_{lz} = \dfrac{1}{a_y}(y_{hz} - y_0) \end{cases} \tag{3.13}$$

We already know the relationship between fringe patterns at zoom levels 1x and 2x; therefore by knowing the relationship between fringe patterns at zoom levels 2x and 3x, the relationship between 1x and 3x will be known. Namely, the map from 1x to 2x can be written as:

$$\begin{cases} x_{1\times} = \dfrac{1}{2.091}(x_{2\times} - 6.1) \\ y_{1\times} = \dfrac{1}{1.992}(y_{2\times} - 2.0) \end{cases} \tag{3.14}$$

and the map from 2x to 3x is given as:

$$\begin{cases} x_{2\times} = \dfrac{1}{1.526}(x_{3\times} + 2.4) \\ y_{2\times} = \dfrac{1}{1.500}(y_{3\times} + 0.1) \end{cases} \tag{3.15}$$

Therefore map between coordinate of the 1x and 3x zoom will be:

$$\begin{cases} x_{1\times} = \dfrac{1}{2.091}\left(\dfrac{1}{1.526}(x_{3\times} + 2.4) - 6.1\right) = \dfrac{1}{3.191}x_{3\times} - 2.2 \\ y_{1\times} = \dfrac{1}{1.992}\left(\dfrac{1}{1.500}(y_{3\times} + 0.1) - 2.0\right) = \dfrac{1}{2.998}y_{3\times} - 1.0 \end{cases} \tag{3.16}$$

This means that the change of zoom in X direction is 3.191 and in Y direction is 2.998. The shift in X direction is 2.2 pixels and in Y direction is 1 pixel.

The next sample that we measured with moiré system was a solder bump flip chip. Figure 48 shows the moiré fringe patterns from the solder bump at zoom levels 1x, 1.5x, 2.5x and 3.5x. As in the previous experiment we would like to locate the fringe pattern with the highest zoom level (3.5x) in the coordinate of fringe pattern with lowest zoom

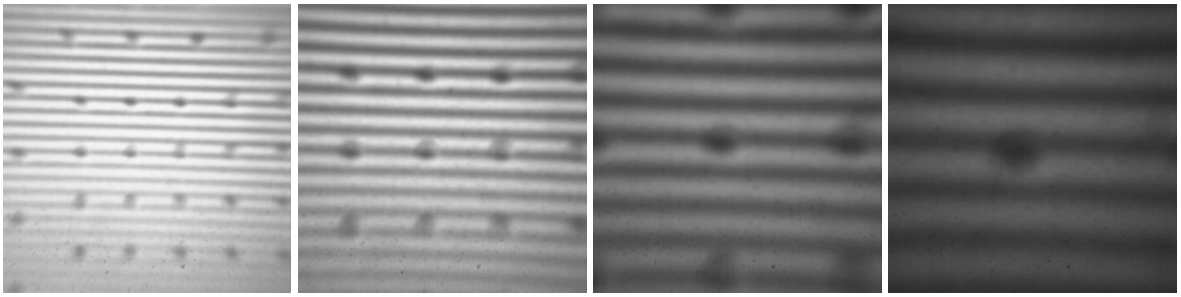

(a) (b) (c) (d)

Figure 48: Moiré fringe patterns from a solder bump flip chip at zoom levels (a): 1x, (b): 1.5x, (c): 2.5x and (d): 3.5x

level (1x). The procedure is the same. To do that, we applied the stitching algorithm to the moiré fringe patterns with zoom levels 1x and 1.5x (Figure 49.(a,b,c)). The next pair is the moiré fringe patterns with zoom levels 1.5x and 2.5x (Figure 49.(d,e,f)) and finally, the image registration was applied to the moiré fringe pattern with zoom levels 2.5x and 3.5x (Figure 49.(g,h,i)). The corresponding parameters are given in the Table 9. The total scale and shift is calculated as:

$$\begin{cases} x_{1\times} = \frac{1}{1.523}\left(\frac{1}{1.728}\left(\frac{1}{1.394}\left(x_{3.5\times} - 5.9\right) - 14.5\right) + 2.8\right) = \frac{1}{3.669}x_{3.5\times} - 5.3 \\ y_{1\times} = \frac{1}{1.479}\left(\frac{1}{1.623}\left(\frac{1}{1.376}\left(y_{3.5\times} + 0.7\right) - 0.8\right) + 1.6\right) = \frac{1}{3.303}y_{3.5\times} + 1.0 \end{cases} \quad (3.17)$$

As it is seen the change of zoom levels from the lowest to the highest zoom level are 3.67 and 3.30 in X and Y directions, respectively. The shift in X and Y directions are 5.3 and 1.0 pixels, correspondingly.

At the next step, we zoomed in on the solder bumps and start to get laser interferograms and finding the location of laser interferograms (corresponding to the fine measurement of the features of the object) with respect to the coordinate of moiré fringe pattern at the lowest level. By finding this relationship, we were able to find the coordinate of each pixel at any fringe pattern with respect to a specific pixel on the fringe

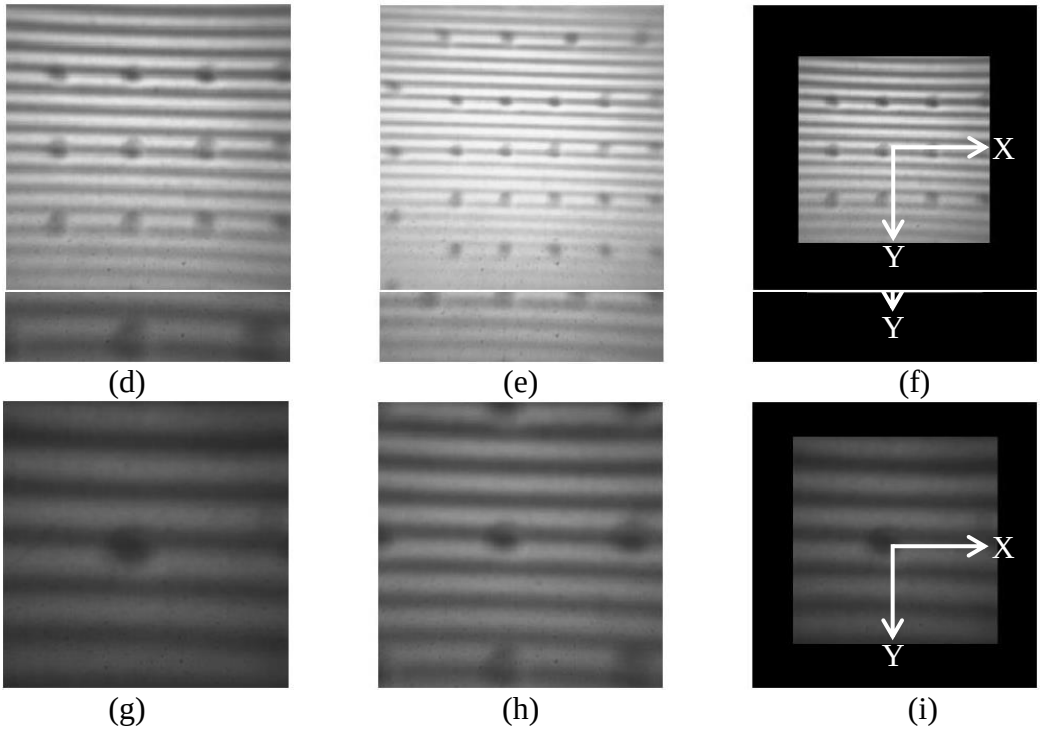

Figure 49: Finding the location of fringe pattern with zoom level 3.5x (g) with respect to fringe pattern with zoom level 1x (b). This is done in three steps. First the fringe pattern with zoom level 1.5x (a) is located in the coordinate of the fringe pattern with zoom level 1x (b). (c) shows the scaled and transferred fringe pattern with zoom level 1.5x at the coordinate of fringe pattern with zoom level 1x. The same is performed for moiré fringe patterns with zoom levels 2.5x (d) and 1.5x (e) pair and moiré fringe pattern with zoom levels 3.5x (g) and 2.5x (h). (f) shows the scaled and transferred fringe pattern with zoom level 2.5x at the coordinate of fringe pattern with zoom level 1.5x and (i) shows the scaled and transferred fringe pattern with zoom level 3.5x at the coordinate of fringe pattern with zoom level 2.5x.

Table 9: Scale (change of zoom level in X and Y directions) and translation (shift in X and Y directions) values for moiré fringe patterns for a solder bump flip chip (Figure 49).

Moiré Fringe Patterns Pair	**X-Translation (Pixels)**	**Y-Translation (Pixels)**	**X-Scale**	**Y-Scale**
1x and 1.5x	-2.8	-1.6	1.523	1.479
1.5x and 2.5x	14.5	0.8	1.728	1.623
2.5x and 3.5x	5.9	-0.7	1.394	1.376

pattern at the lowest zoom level, in which represents a reference point on the object. Having this capability enabled us to find the form of the object (using moiré fringe patterns) and for a specific point or region on the object, finding the features of the object (using laser fringe patterns).

To relate the moiré fringe patterns and laser fringe patterns we needed to have a specific zoom level in which both moiré and laser fringe patterns could be obtained. This means that the range of measurement for moiré system and laser interferometer have to overlap. The choice of moiré system and laser interferometer as a multiscale measurement instrument was based on this consideration. On the other word, the range of measurement for moiré system and range of the measurement for the laser interferometer overlap. At this specific zoom level, we are able to acquire both moiré and laser fringe patterns. Note that the fringe patterns at this zoom levels does not need to be processable using the fringe analysis software, but they need to be processable using the image registration algorithm. Therefore at that zoom level we acquire fringe patterns from both moiré and laser interferometer. Since both moiré system and laser interferometer use the same camera (Figure 30) the pixels of moiré fringe pattern and laser fringe pattern have a one-to-one relationship. This means that the parameters that relate these two fringe patterns are known (no change in zoom level and zero shift). This relationship between two fringe patterns are based on the assumption that the camera is focused on the object and therefore both moiré fringe pattern and laser fringe pattern represent the same part of the object.

The first solder bump sample have been coated with a layer of the paint, therefore we were not able to acquire a processable laser interferogram. Therefore we used another solder bump sample and captured both moiré and laser fringe patterns (Figure 50). As it is seen, we have processable moiré fringe patterns at zoom levels 1x, 2x, 4x and processable laser interferograms at 48x, 24x, and 16x.

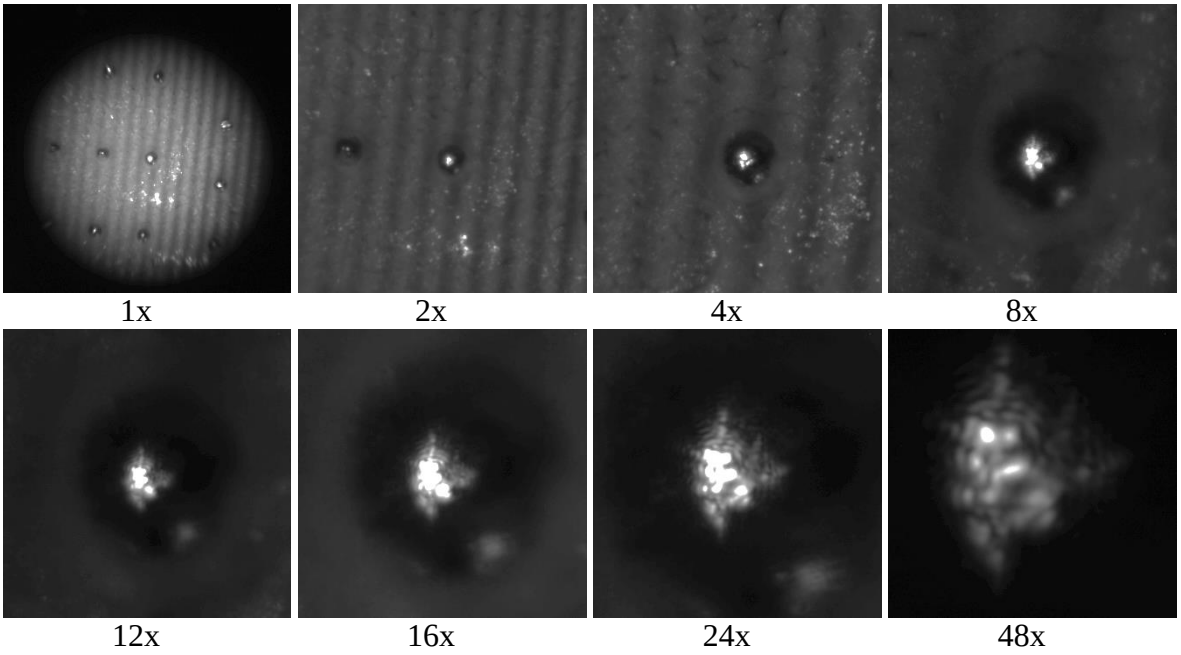

(a)

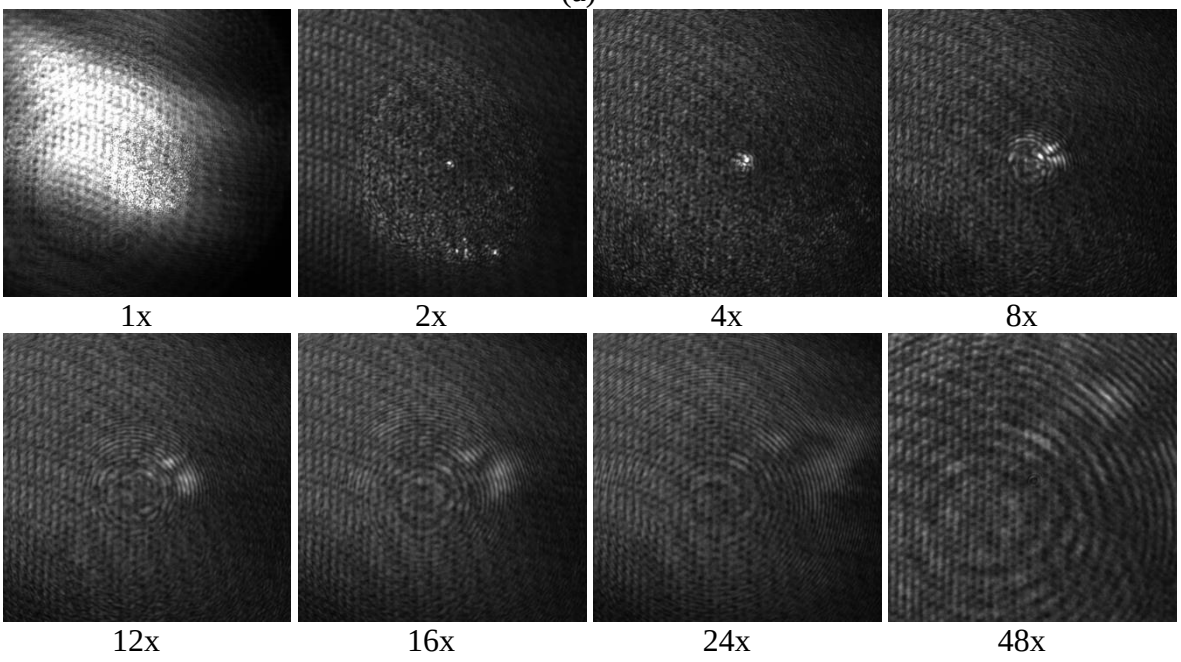

(b)

Figure 50: (a): Moiré fringe patterns at zoom levels 1x to 48x. (b): laser interferograms at zoom levels 1x to 48x.

To demonstrate stitching the data from the lowest to the highest zoom level we considered the moiré fringe patterns at zoom levels 1x, 2x 4x, and 8x and laser fringe patterns at zoom levels 8x, 16x, 24x and 48x. The solder bump flip chip that was imaged

had the same structure as the one in Figure 48, but the tip of the bumps were not coated and because of that there were saturated pixels on the moiré fringe patterns.

We know the pixels of laser interferogram and moiré fringe pattern have the one-to-one correspondence at zoom level 8x. Therefore if we stitch the laser interferograms from zoom level 8x to 48x, then the location of each pixel at zoom level 48x (highest zoom level) can be found with respect to a reference point on the object (i.e. moiré fringe pattern at zoom level 1x).

The stitching algorithm was applied to the moiré fringe patterns at zoom level 1x, 2x, 4x and 8x and for laser interferograms at zoom levels 8x, 16x, 24x and 48x. Figure 51 and Table 10 show the results of the stitching algorithm. Figure 52 shows the stitched image from the moiré and laser interferograms. The stitched image is at the coordinate of the moiré interferogram at zoom level 1x. As it is seen the coordinate of each pixel at the

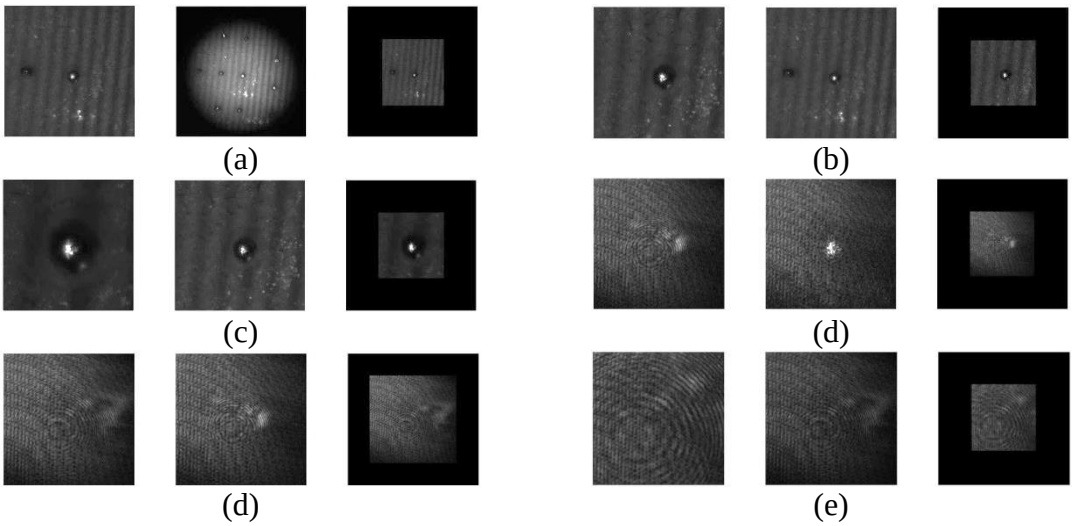

Figure 51: Results of image registration for moiré and laser interferograms. At each image, the first image is the image in the higher zoom level, the second image is the in eat lower zoom level, and the third image is the scale and shifted image at higher zoom level in the coordinate of the image with lower zoom level. The parameters for each registration are given in Table 10. (a): moiré interferograms at zoom levels 1x and 2x. (b): moiré interferograms at zoom levels 2x and 4x. (c): moiré interferograms at zoom levels 4x and 8x. (d): laser interferograms at zoom levels 8x and 16x. (e): laser interferograms at zoom levels 16x and 24x. (f): laser interferograms at zoom levels 24x and 48x.

Table 10: Results of image registration for moiré interferograms at zoom levels 1x, 2x, 4x, and 8x; and for laser interferograms at zoom levels 8x, 16x, 24x, and 48x.

Moiré Fringe Patterns Pair	**X-Translation (Pixels)**	**Y-Translation (Pixels)**	**X-Scale**	**Y-Scale**
1x and 2x	-3.0	0.0	1.974	2.118
2x and 4x	0.6	0.0	2.024	2.022
4x and 8x	0.4	0.0	1.999	1.992
Laser Interferograms Pair	**X-Translation (Pixels)**	**Y-Translation (Pixels)**	**X-Scale**	**Y-Scale**
8x and 16x	1.3	1.6	2.031	2.038
16x and 24x	1.0	0.9	1.511	1.517
24x and 48x	3.5	1.5	2.000	2.034

highest zoom level (48x) is determined at the coordinate of the image at the lowest zoom level (1x). The relation between the coordinate at zoom level 48x and 1x can be calculated as:

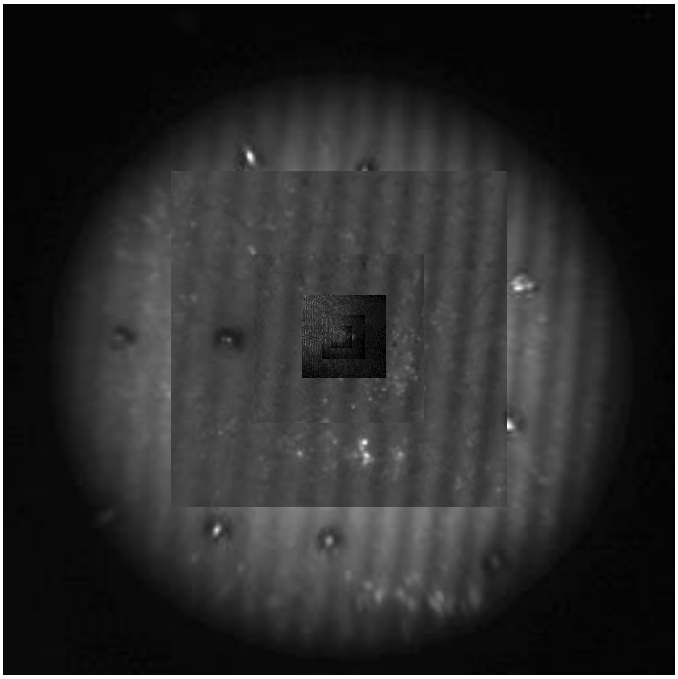

Figure 52: Stitched image of moiré and laser interferograms at the coordinate of the image at zoom level 1x.

$$\begin{cases} x_{8\times} = \dfrac{1}{2.031}\left(\dfrac{1}{1.511}\left(\dfrac{1}{2.000}(x_{48\times} - 3.5) - 1.0\right) - 1.3\right) = \dfrac{1}{6.138}x_{48\times} - 1.5 \\ y_{8\times} = \dfrac{1}{2.038}\left(\dfrac{1}{1.517}\left(\dfrac{1}{2.034}(y_{48\times} - 1.5) - 0.9\right) - 1.6\right) = \dfrac{1}{6.288}y_{48\times} - 1.3 \end{cases} \tag{3.18}$$

$$\begin{cases} x_{1\times} = \dfrac{1}{1.974}\left(\dfrac{1}{2.024}\left(\dfrac{1}{1.999}(x_{8\times} - 0.4) - 0.6\right) + 3\right) = \dfrac{1}{7.987}x_{8\times} + 1.3 \\ \quad = \dfrac{1}{7.987}\left(\dfrac{1}{6.138}x_{48\times} - 1.5\right) + 1.3 = \dfrac{1}{49.024}x_{48\times} + 1.1 \\ y_{1\times} = \dfrac{1}{2.118}\left(\dfrac{1}{2.022}\left(\dfrac{1}{1.992}(y_{8\times} - 0.0) - 0.0\right) - 0.0\right) = \dfrac{1}{8.531}y_{8\times} \\ \quad = \dfrac{1}{8.531}\left(\dfrac{1}{6.288}y_{48\times} - 1.3\right) = \dfrac{1}{53.643}y_{48\times} - 0.1 \end{cases} \tag{3.19}$$

The next step is to analyze the laser interferograms fringes in order to calculate the profile of the features, but due to the damage on the tip of the solder bump, we were not able to correctly reconstruct the profile. Figure 53 shows the unwrapped phase map for the laser interferograms at the zoom level 24x with different parameters. As it is seen, none of the unwrapped phase map represents the correct phase map. We used Intelliwave™, a commercial fringe analysis software, and tried to manually identify the fringes and their orders to reconstruct the profile with no success. Figure 54 shows the result for the same laser interferogram at zoom level 24x using Intelliwave. Therefore we made another sample which was a mirror covered by paper tape unless for a small aperture. Figure 55 shows the object. The paper tape part of the object can be analyzed by moiré fringe pattern, while the mirror part of the surface can be analyzed using laser fringe patterns. For this object we removed both Mitutoyo M Plan Apo 5x Objective lens and VZM 450 Zoom Imaging Lens and left 12.5x Precision Zoom Lens from the camera arm. The zoom range in the camera arm is then between 1x and 13x.

The moiré fringe patterns were taken at zoom levels 1x, 1.5x, 2x and 3x and the laser

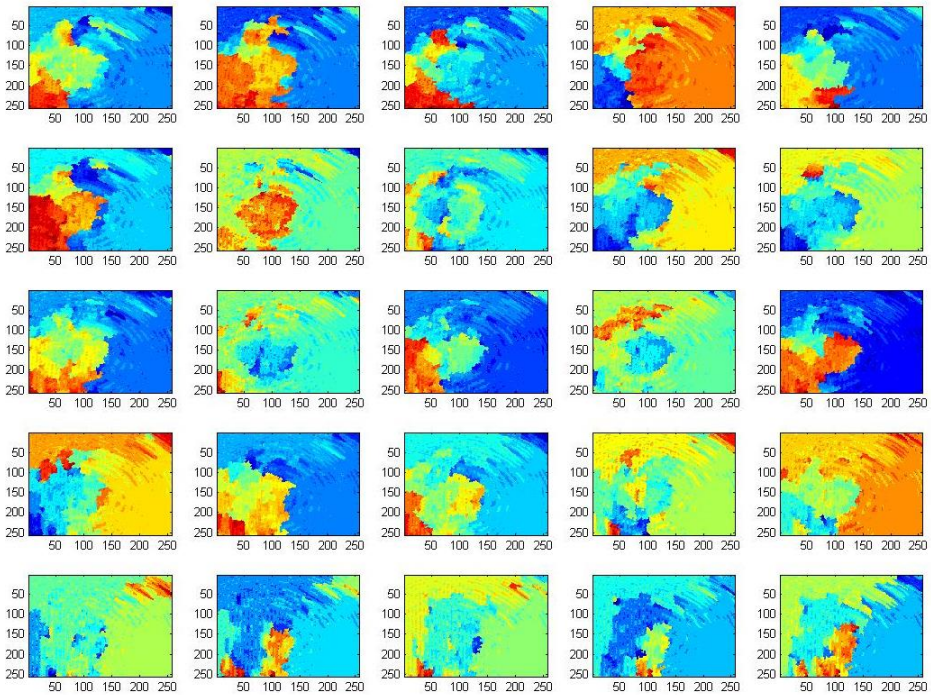

Figure 53: The unwrapped phase of laser interferogram at zoom level 24x with different parameters. The rows show the unwrapped phase with different window size (5, 10, 15, 20 and 25 pixels) of short time Fourier transform and the columns show the unwrapped phase from wrapped phase map with different noise with different DC noise reduction (using high pass filter with cutoff frequency of 6, 12, 18, 24 and 30).

interferograms at zoom levels 2x, 3x, 4x, 6x, 8x, 10x, 12x and 13x. Figure 56 shows the acquired interferograms from fringe projection (Figure 56.a) and laser interferogram

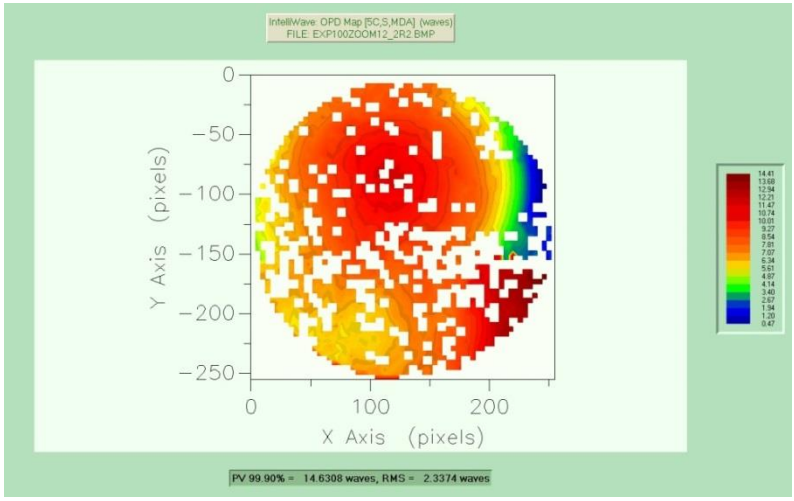

Figure 54: Result of phase unwrapping for the laser interferogram at zoom level 24x with IntelliWave

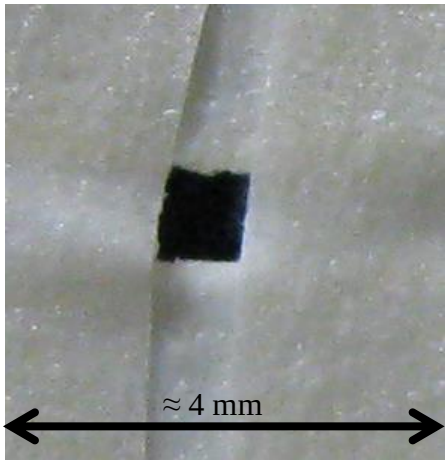

Figure 55: The object: a mirror surface covered with paper tape, except for a small aperture.

(Figure 56.b). As it is seen, moiré fringes show a dark region where the mirror surface is located while the mirror surface has visible fringe pattern when fringe pattern is acquired using laser interferometer.

The moiré fringes first were stitched using the image registration and then the laser interferograms at zoom levels 3x, 6x, 12x and 13x were registered. Figure 57 shows the registered interferograms and Table 11 shows the calculated parameters of image registration. Therefore using the calculated parameters, the coordinate of each pixel in any zoom level can be calculated with respect to a reference point on the object (i.e. coordinate of the image with the lowest zoom level).

$$\begin{cases} x_{3\times} = \frac{1}{2.002}\left(\frac{1}{2.006}\left(\frac{1}{1.092}(x_{13\times} - 4.5) + 1.5\right) - 0.8\right) = \frac{1}{4.386}x_{13\times} - 1.0 \\ y_{3\times} = \frac{1}{2.016}\left(\frac{1}{2.003}\left(\frac{1}{1.093}(y_{13\times} + 1.1) - 3.6\right) + 5.6\right) = \frac{1}{4.414}y_{13\times} + 2.1 \end{cases} \quad (3.20)$$

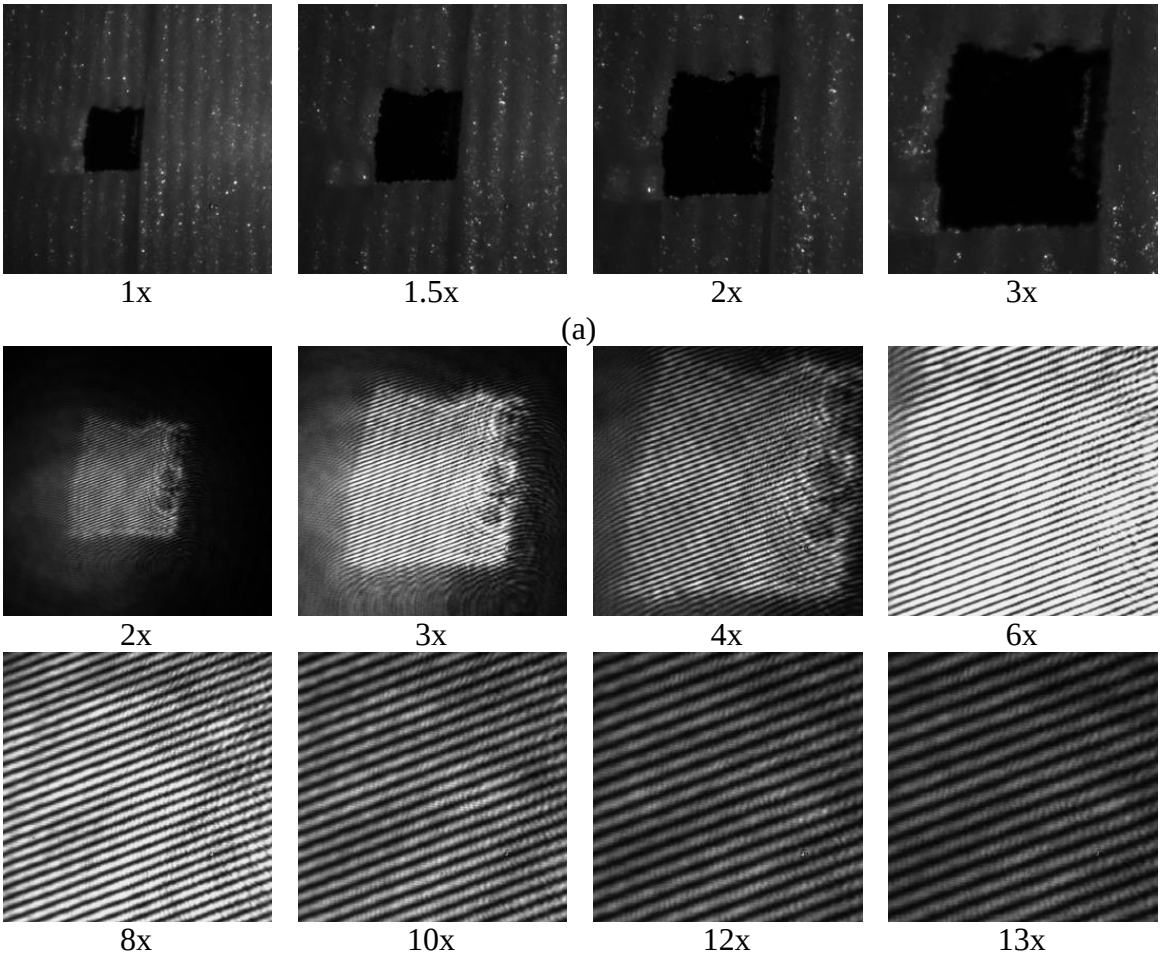

Figure 56: Interferograms from a mirror surface covered with paper tape except for an aperture. (a): Moiré fringe patterns at zoom levels 1x, 1.5x, 2x and 3x. (b): laser interferograms at zoom levels 2x, 3x, 4x, 6x, 8x, 10x, 12x and 13x

$$\begin{cases} x_{1\times} = \dfrac{1}{1.505}\left(\dfrac{1}{1.331}\left(\dfrac{1}{1.508}(x_{3\times} - 0.8) - 0.0\right) - 0.5\right) = \dfrac{1}{3.021}x_{3\times} - 0.6 \\ \qquad = \dfrac{1}{3.021}\left(\dfrac{1}{4.386}x_{13\times} - 1.0\right) - 0.6 = \dfrac{1}{13.250}x_{13\times} - 0.9 \\ y_{1\times} = \dfrac{1}{1.501}\left(\dfrac{1}{1.343}\left(\dfrac{1}{1.515}(y_{3\times} - 2.1) - 0.3\right) - 0.8\right) = \dfrac{1}{3.054}y_{3\times} - 1.4 \\ \qquad = \dfrac{1}{3.054}\left(\dfrac{1}{4.414}y_{13\times} + 2.1\right) - 1.4 = \dfrac{1}{13.480}y_{13\times} - 0.7 \end{cases} \tag{3.21}$$

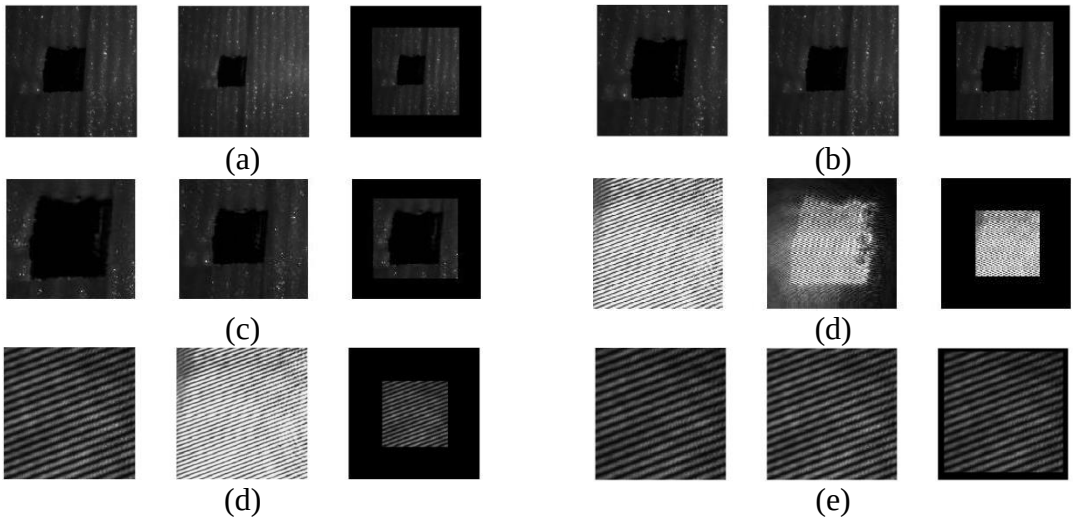

Figure 57: Results of image registration for moiré and laser interferograms. At each image, the first image is the image in the higher zoom level, the second image is the in eat lower zoom level, and the third image is the scale and shifted image at higher zoom level in the coordinate of the image with lower zoom level. (a) Moiré interferograms at zoom levels 1x and 1.5x. (b) moiré interferograms at zoom levels 1.5x and 2x, (c) moiré interferograms at zoom levels 2x and 3x, (d) laser interferograms at zoom levels 3x and 6x, (e) laser interferograms at zoom levels 6x and 12x, and (f) laser interferograms at zoom levels 12x and 13x.

Table 11: Results of image registration for moiré interferograms at zoom levels 1x, 1.5x, 2x, and 3x; and for laser interferograms at zoom levels 3x, 6x, 12x, and 13x.

Moiré Fringe Patterns Pair	**X-Translation (Pixels)**	**Y-Translation (Pixels)**	**X-Scale**	**Y-Scale**
1x and 1.5x	.5	0.8	1.505	1.501
1.5x and 2x	0.0	0.3	1.331	1.343
2x and 3x	0.8	2.1	1.508	1.515
Laser Interferograms Pair	X-Translation (Pixels)	Y-Translation (Pixels)	X-Scale	Y-Scale
3x and 6x	0.8	-5.6	2.002	2.016
6x and 12x	-1.5	3.6	2.006	2.003
12x and 13x	4.5	-1.1	1.092	1.093

Figure 58 shows the object at different zoom levels. As it is seen at low zoom level 1x the form of the object is apparent, but the details of the profile are not visible, when we zoom in on the object the features of the object are apparent at higher zoom level (e.g. 12x).

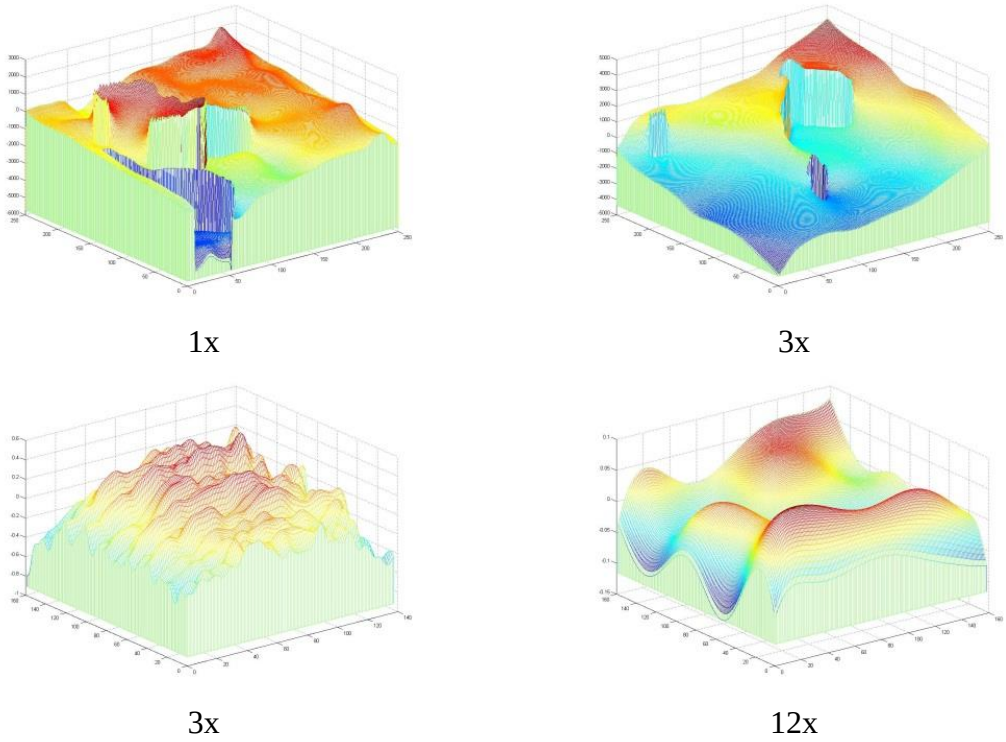

Figure 58: Profile of object in Figure 55 at different zoom levels

3.6. Uncertainty Analysis

To characterize the system, an uncertainty analysis was performed for both moiré system and laser interferometer, namely the repeatability of the moiré system and laser interferometer were measured. To measure the repeatability we performed the following procedure: at each zoom level we acquired an interferogram, then removed the object and put it back in its place and measured the object again by acquiring an interferogram. We performed this procedure ten times for each zoom level. Then the profile is calculated for each interferogram. The standard deviation of difference between the measurements are calculated and normalized to the wavelength (equivalent wavelength for moiré system). Then the normalized standard deviation is multiplied by six to obtain the error at 99.6%. Table 12 shows the results of uncertainty analysis. As it is shown, the repeatability for

Table 12: Error percentage at different zoom levels for fringe projection and laser interferometer

Fringe Projection		**Laser Interferometer**	
Zoom Level	**Normalized Repeatability %**	**Zoom Level**	**Normalized Repeatability %**
1	0.34	5	0.33
1.5	0.34	7.5	0.41
2	0.58	10	0.18
3	0.15	15	0.25
4	0.40	20	0.42
5	0.11	25	0.33
7.5	0.33	30	0.37
10	0.23	32.5	0.44

fringe projection is below 0.6% and the repeatability for laser interferometer is below 0.44% for different zoom levels.

The majority of measurement error comes from instability of laser wavelength, vibration of optical table, air flow and electronics noise. Also there are diffraction patterns that distort the interferograms.

3.5.1. Lateral Resolution

Dual moiré laser interferometer uses two zoom lenses: a $12.5\times$ precision zoom lens and a VZM 450 zoom imaging lens. Considering the $12.5\times$ precision zoom lens the lateral resolution at the highest zoom level ($13\times$) is 300 lp/mm which results in lateral resolution of $r_1 = \frac{1000}{2\times300} = 1.66\,\mu m$. In the case of VZM 450 zoom imaging lens, the resolution at the highest zoom level ($4.5\times$) is 144 lp/mm which means that the highest resolution for this zoom lens would be $r_2 = \frac{1000}{2\times144} = 3.47\,\mu m$.

Considering the cameras, two cameras have been used in the dual moiré laser interferometer system; first one was SUMIX SMX-M73 and the second one was AVT Guppy F-146. Therefore the second camera (the one with the lower number of pixels) would be the camera that might limit the lateral resolution. To calculate the best available

resolution based on the camera resolution we need the field of view. The field of view for the 12.5 × precision zoom lens at the highest zoom level is $0.37 \times 0.49\ mm$; and for the VZM 450 zoom imaging lens is $1.05 \times 1.40\ mm$ (for $\frac{1}{2"}$ camera sensor size). Therefore the corresponding best lateral resolution limited by camera would be $r_1' = \frac{0.49}{1392} = 352\ nm$ for the 12.5 × precision zoom lens and $r_2' = \frac{1.40}{1392} = 1000\ nm$ for the VZM 450 zoom imaging lens. Comparing these resolutions with the resolution of the zoom lenses (r_1 and r_2), it can be concluded that the lateral resultion is limited by the resolution of the zoom lenses, r_1 and r_2, and can be improved by improving the quality of zoom lenses.

The other parameters that contribute to the uncertainty are noise including the speckle noise and electronics noise, instability of laser wavelength, vibration of optical table, air flow, diffractions that are represented as dense circular fringe patterns on captured interferograms, errors in phase wrapping and unwrapping[16], misalignment and error of operator.

3.7. Conclusion

We have developed a new multi-scale dual moiré laser measurement system, which benefits from techniques with different measurement scales. Our measurement system includes a fringe projection system which does the coarse measurement (form of the object) and a laser interferometer measuring features of the object. We developed several prototypes and at each step the system was fully characterized and was lessons were used in the design of next prototype. Some optical arrangements of the system were simulated and optimized in Zemax in order to improve the overall system performance.

[16] We have up to 1/100th of wavelength accuracy for height measurement

Both moiré and laser interferometer were simulated with MATLAB and simulated fringe patterns were calculated. We used those simulated fringe patterns to validate and evaluate our proposed algorithm for stitching data from moiré system and laser interferometer.

The core of our algorithm for stitching data is the image registration technique. Our algorithm was implemented in MATLAB and the results showed pixel level resolution for stitching algorithm.

A software to analyze fringe patterns was also developed. Fourier analysis was used for phase wrapping step and quality guided technique was used for phase unwrapping.

An error analysis was performed to characterize the system. The relative error for both moiré and laser interferometer are within 5% of equivalent wavelength for moiré system and 1% of wavelength for laser interferometer at different zoom levels.

Results show that the dual moiré laser interferometer is capable of measuring the object in both low and high resolutions and the data from both moiré system and laser interferometer can be stitched to construct a continuous image of the object under measurement.

CHAPTER 4: COMPRESSIVE SAMPLING AND COMPRESSIVE IMAGING

Some of the problems that we encounter in the field of optical metrology include low light condition, high dynamic range of intensity, hyperspectral measurement; just to name a few. We tried to address these problems using compressive sampling/sensing (CS). Compressive sampling uses a single detector instead of array of detectors and reconstructs a complete image after several measurements.

Under low light condition there is not enough light for detector to detect the light from the object, which results in poor measurements. Using compressive sampling we can collect the light from almost half of the scene for each sample and also use a very sensitive detector like photomultiplier to be able to work under extremely low light level.

High dynamic range of intensity results in a measurement with some saturated regions as well as some dark regions. Our approach to this problem was using compressive sampling setup, which can be used as high dynamic range imaging system while benefiting from the compressive sampling, too.

Reaching high resolution in hyperspectral imaging requires pixel by pixel measurement and the hyperspectral imaging systems that acquire spectral images in one shot are not high resolution. Since compressive imaging uses one pixel, it is possible to acquire high resolution spectral images instead of either high resolution point measurement or low resolution spectral images.

Compressive imaging has been derived from compressive sampling/sensing theorem. In the following sections, the concept of compressive sampling is explained and then the compressive imaging (CI) with its different applications will be explained. The next chapter explains the experiments and results of different compressive imaging systems.

4.1. Compressive Sampling

Compressive sampling is an emerging area with wide range of applications [113], [114], [115], [116]. Compressive sampling has found many applications in different areas of science and engineering including imaging [117], [118], [119] , communications [120], [121], analog to digital converters [122], [123], computational biology[124], etc.

The basic idea of compressive sampling comes from the fact that if a signal (signal can be one- or multi-dimensional) can be represented sparsely in a domain, then, this signal can be sampled at rates lower than the Nyquist rate. The Nyquist sampling theorem says that if a signal is band-limited, with B being its highest frequency, the signal shall be sampled at least at a rate of 2B, in order to allow its exact reconstruction. This condition of Nyquist theorem might be considered as the worst case; in other words, it is the sufficient condition for successful reconstruction of the signal, but not necessary condition. For example, for some multiband signals, there are different methods to sample the signal at rates lower than the Nyquist rate [125]. This sub-Nyquist rate can be achieved if the signal is sparse. The sub-Nyquist sampling can be done uniformly, non-uniformly [125], randomly [122], [126], [127], in time or frequency domain [128].

There are two important concepts in the theory of compressive sampling: *sparsity* and *incoherence*. The sparsity of a discrete time signal[17] expresses that the degree of freedom of the signal is much smaller than the length of the signal. On the other words, sparsity means that the signal has a representation in a domain in which most of its coefficients in that domain are zero.

The other concept in compressive sampling is *incoherence*. While the sparsity deals with the signal itself, the incoherence deals with the relation between the sampling domain and the domain in which the signal is sparse. It expresses that the sparse signal in the sampling domain should have a representation with as much nonzero coefficients as possible. In other words, the sparse signal has to spread out in sampling domain. As the signal spreads more in sampling domain it would be more incoherent and less number of samples is needed for reconstruction.

In the following the building blocks and some important results of compressive sampling are discussed.

4.1.1. Sampling

The sampling in CS is a linear function; the signal x with the length of N is correlated with a sampling vector φ_i:

$$y_i = \langle \boldsymbol{x}, \boldsymbol{\varphi_i} \rangle = \sum_{j=1}^{N} x_j \varphi_{i,j} \tag{4.1}$$

The sampling vector can be any vector. For example if $\{\varphi_i\}$ are delta functions, then the samples $\{y_i\}$ are samples in the same domain as signal (e.g. time, space). If the sampling vectors are sinusoidal functions, then the samples $\{y_i\}$ are the Fourier

[17] In this chapter and next chapter we only consider discrete time signals since we only deal with discrete time signals and most of compressive sampling theory is developed for that type of signals.

coefficients. If the sampling vectors are wavelets, then the samples $\{y_i\}$ are the wavelet coefficients. The matrix form of the above equation can be written as:

$$y = \Phi x \tag{4.2}$$

where $y = [y_1 \quad \cdots \quad y_M]^{\mathrm{T}}$ and $\Phi = [\varphi_1 \quad \cdots \quad \varphi_M]^{\mathrm{T}}$ and "T" shows the transpose operator.

Φ is a $M \times N$ matrix and is referred as sampling matrix or measurement matrix. In CS the number of measurements is smaller than the length of the signal ($M < N$) and therefore the problem, in general, is an ill-posed problem since the number of equations (samples) is smaller than the number of variables (length of the signal). The question in compressive sampling is that, "what are the conditions that the signal can be recovered from the incomplete set of samples?" This is where two concepts of sparsity and incoherence come into play; the compressive sampling theory states that with having sparsity and incoherence properties it is possible to approximately (and even exactly) recover the undersapmled signal.

4.1.2. Sparsity

In a mathematical form, suppose that the discrete time signal x can be represented in the basis Ψ as follows:

$$x = \sum_{i=1}^{N} a_i \psi_i \tag{4.3}$$

in which only m coefficients a_i are nonzero. Then x is m-sparse in the domain Ψ. We measure the nonzero elements by using l_0 norm and show it by $\|.\|_0$ (although mathematically l_0 does not have the properties of a norm). In equation (4.3) the nonzero coefficients of x in basis Ψ are supported in a relatively small set ($\|a_i\|_0 = m < N$). If

outside of that small set the sorted coefficients are not zero but very small, and decaying rapidly enough, the signal is said to be compressible. A compressible signal can be approximated with a sparse signal and therefore it can satisfy the CS condition for sparsity.

Signals and images are usually compressible. Figure 59 shows two images that are compressed using wavelet packet with symlet of order 8 and the fifth level of the wavelet packet tree. Figure 59.a is the original image and Figure 59.b is the compressed image. To compress the image, the wavelet coefficients with the low energy are set to zero (thus making the signal strictly sparse). For Figure 59.b about 99% of wavelet coefficients are set to zero (compression ratio[18] of about 100). The remaining coefficients preserve about 99% of the energy of the original image (Figure 59.a). This means that the image can be approximated with a sparse image in wavelet packet domain. Then the images are reconstructed using the new wavelet coefficients. As it is seen the quality of the image have not degraded visually. The second example is Figure 59.c. The results of compression are demonstrated in Figure 59.d and Figure 59.e. Figure 59.d is the compressed image when around 96% of wavelet coefficients set to zero (compression ratio of about 25). With this rate of compression the new image holds 99.86% of the original image energy. To compress the image more, we zeroed 99.43% of wavelet coefficients (compression ratio of about 175). The compressed image preserves 99.4% of original image energy. The result of this compression is shown in Figure 59.e. As it is seen the quality of the image is not degraded visually. The results show that how much

[18] The compression ratio in here calculated based on the percentage of the coefficients set to zero and the information about the location of nonzero coefficients are not considered in the calculation, otherwise the compression ratio will be less since the location information of nonzero elements are needed to be stored, too.

(a) (b)

(c) (d) (e)

Figure 59: Image compression using wavelet packet. The original images (a) and (c) were compressed using wavelet packet tree at level 5 and Symlet wavelet of order 8. (b) is the compressed image of (a) when 99% of wavelet coefficients are set to zero; the compressed image preserves about 99% of energy. (d) is the compressed image of (c) when 96% of wavelet coefficients are set to zero; the remaining coefficients keep 99.86% of original image energy. (e) is the compressed image of (c) when 99.43% of coefficients are set to zero; the nonzero coefficients retain 99.43% of original image energy.

sparse the images can be if a proper basis is used. This is true for most of the signals and images[19]; and since the theory of compressed sensing and its results are mostly based on probability and statistics theory, the compressed sensing technique works for most images and signals with overwhelming probability. Therefore a compressible signal can be transformed into a sparse signal (in a proper basis) without losing significant information. In other words, when it is mentioned that an image is sparse in a specific basis, it is either sparse itself or it is compressible and can be transformed into a sparse signal by zeroing the coefficients with insignificant energy.

4.1.3. Incoherence

Mathematically, consider two bases Ψ and Φ each with N normalized elements. Then the mutual coherence between these two bases is defined as [129]:

$$M(\Phi,\Psi) = \sqrt{N}\sup_{i,j}\{|\langle\varphi_i,\psi_j\rangle|\} \tag{4.4}$$

which can be simply described as a similarity measure between two bases. The incoherence criterion states that in order to reconstruct a sparse signal with as few samples as possible the sparse basis and measurement basis need to be as incoherent as possible. In other words, let Ψ be the sparse basis and Φ the measurement basis, then the lower $M(\Phi,\Psi)$ means that a lower number of samples is needed to reconstruct the signal. This means that compressive sampling looks for bases with low coherence. Some examples of low coherence bases pairs are wavelet packets and noiselets [130], Fourier basis and delta functions, and scrambled Hadamard codes [131] and Gabor basis. The first and third pairs are the pairs that one of the bases has random properties (noiselet and

[19] There are and one can make a signal that is not compressible with respect to a basis or a family of bases. For example considering wavelet packet, the noiselets are totally uncompressible by orthogonal wavelet packets [130].

scrambled Hadamard codes). In fact random bases usually have low coherence with any fixed basis [115].

4.1.4. Signal Recovery

Assuming that the signal is sparse and a number of samples were acquired using a measurement matrix A. The undersampled signal, then, can be reconstructed using the following optimization:

$$\min_x \|x\|_0 \quad \text{subject to} \quad y = Ax \tag{4.5}$$

This means that the optimization problem looks for the sparsest signal that is consistent with the measurements y. The problem here is the fact that the zero norm is highly nonconvex, the problem is NP-hard and solving this problem has high computational cost. Chen and Donoho [132], [133] suggested to use l_1 norm, which is a convex functional, in order to recover a sparse signal. Thus the optimization problem can be expressed as:

$$\min_x \|x\|_1 \quad \text{subject to} \quad y = Ax \tag{4.6}$$

Their method, named Basic Pursuit, uses linear programming to efficiently solve the optimization problem.

The early works for reconstruction with l_1 minimization were done by Santosa and Symes [134] in 1983. They showed that it is possible to reconstruct a sparse spark train from part of its spectrum with l_1 minimization. In 1989, Donoho and Stark [135] showed that under certain conditions a noisy signal can be recovered perfectly with l_1 minimization (Logan's Certainty Principle), while it is not possible to do so with l_2 minimization. Since then there has been a lot of interest on sparse representation and l_1 minimization [136], [137].

Another approach for recovering sparse signals is Matching Pursuit, which is a greedy algorithm. The Matching Pursuit algorithm first was introduced by Mallat and Zhang [138]. In Matching Pursuit algorithm, a sparse approximation of the signal is made by choosing the vectors from the basis that have the most correlation with the measured signal. At each step, one vector is chosen and the residue, which is the difference between the measured signal and the estimated signal at that step is calculated. The residue at the first step is the measured signal itself and at each step the vectors of the basis are correlated with the residue to choose the one with the highest correlation. Examples of compressive sampling algorithms based on Matching Pursuit are given by Dai and Milenkovic [139] and Needell and Tropp [140].

The next approach for sparse signal recovery for an incomplete set of samples of an image is using the total variation (TV) minimization [141]. TV functional for an image of size $M \times N$ pixels can be expressed as:

$$\|x\|_{TV} = \sum_{p=1}^{M-1} \sum_{q=1}^{N-1} \sqrt{\big(x(p+1,q) - x(p,q)\big)^2 + \big(x(p,q+1) - x(p,q)\big)^2} \tag{4.7}$$

where (p,q) shows the pixel indices.

Total variation is an indication of sparsity of the gradient of the image and it was shown that it can recover the image from incomplete set of samples [128], [142], [143], [144]. The optimization problem with TV minimization can be stated as:

$$\min_x \|x\|_{TV} \quad \text{subject to} \quad y = Ax \tag{4.8}$$

There are also other approaches for recovering the signal. For example Chartrand [145] showed that using l_p norm with $p < 1$ can reconstruct the signal with fewer samples compared to l_1 norm.

In practice, samples of the signal are always noisy. To include the effect of the noise in signal recovery, the equality condition in optimization problem is changed to the following inequality:

$$\|y - Ax\|_2 < \varepsilon \tag{4.9}$$

where ε depends on the noise energy.

4.1.5. Some Theorems of Compressive Sampling

As mentioned in previous sections, sparsity and coherence are two necessary conditions for successful recovery of signals in compressive sampling technique. In the following we briefly review some important theorems concerning those properties and how they affect the necessary number of samples and the quality of reconstruction of signals.

The first theorem shows that with how many samples the recovery of the signal will be exact with overwhelming probability. Assume that the signal is sparse in the domain Ψ and the measurement matrix is Φ and $M(\Phi, \Psi)$ shows the incoherence between sparse domain and measurement domain. The theorem states that the number of samples required to recover the signal with length N and S-sparse is of the order of $M^2(\Phi, \Psi).S.\log(N)$.

Theorem 1 [129]: Assume that x is S-sparse in basis Ψ; and we randomly choose m measurement in the domain Φ. Then if the number of measurement m satisfies

$$m \geq C \times M^2(\Phi, \Psi) \times S \times \log(N) \tag{4.10}$$

for some positive (small) constant C, then the solution to the optimization problem (4.6) is exact with overwhelming probability.

As we mentioned in previous section, in reality the samples are corrupted with noise and to deal with this situation the optimization problem (4.6) is modified by (4.9) as:

$$\min_x \|x\|_1 \quad \text{subject to} \quad \|y - Ax\|_2 < \varepsilon \tag{4.11}$$

To have a successful recovery from this noisy situation we need a property which is called Restricted Isometry Property (RIP) [146]

Definition: Let F be the matrix with the finite collection of vectors $\left(v_j\right)_{j\in J} \in R^p$ as columns. For every integer $1 \le S \le |J|$, we define the S-restricted isometry constant δ_S to be the smallest quantity such that F_T obeys

$$(1 - \delta_S)\|c\|_2^2 \le \|F_T c\|_2^2 \le (1 + \delta_S)\|c\|_2^2 \tag{4.12}$$

for all subset $T \subset J$ of cardinality at most S, and all real coefficients $\left(c_j\right)_{j\in T}$.

Vector c is a S-sparse signal and matrix F is said to have RIP of order S if δ_S is not close to one. By using the concept of RIP, the recovery of a sparse signal from its incomplete and inaccurate measurements is stated in the following theorems:

Theorem II [147]: Let S be such that $\delta_{3S} + 3\delta_{4S} < 2$. Then for any signal x_0 supported on T_0 with $|T_0| \le S$ and any perturbation e with $\|e\|_2 \le \varepsilon$, the solution $\hat{x}$ to (4.11) obeys

$$\|\hat{x} - x_0\|_2 \le C_S \times \varepsilon \tag{4.13}$$

where the constant C_S depends only on δ_{4S}. For reasonable values of δ_{4S}, C_S is well behaved; for example, $C_S \approx 8.82$ for $\delta_{4S} = {}^1/_5$ and $C_S \approx 10.47$ for $\delta_{4S} = {}^1/_4$. It is worth to note that for noiseless data, $\varepsilon = 0$, the reconstruction is exact.

The next theorem deals with the condition where the signal is not strictly sparse.

Theorem III [147]: Suppose that x_0 is an arbitrary vector in $\mathbb{R}^m$, and let $x_{0,S}$ be the truncated vector corresponding to the S largest values of x_0 (in absolute value). Under the hypotheses of Theorem II, the solution $\hat{x}$ to (4.11) obeys

$$\|\hat{x} - x_0\|_2 \leq C_{1,S} \times \varepsilon + C_{2,S} \times \frac{\|x_0 - x_{0,S}\|_1}{\sqrt{S}} \tag{4.14}$$

for reasonable values of δ_{4S}, the constants $C_{1,S}$ and $C_{2,S}$ are well behaved; for example, $C_{1,S} \approx 12.04$ and $C_{2,S} \approx 8.77$ for $\delta_{4S} = {}^1/_5$.

This theorem is especially helpful for compressible signals where the signal is not strictly sparse, but the sorted coefficients of the signal decay rapidly.

The mentioned theorems, especially the last one, form foundation for the compressive sampling as a technique for sampling signals that are or are not sparse and noisy. The next section deals with the design of measurement matrices for compressive sampling.

4.1.6. Measurement Matrix

The matrix A in (4.11) is the multiplication of measurement matrix and basis in which the signal is sparse, i.e. $A = \Phi\Psi$. In the previous section it was stated that the robust recovery of the sparse signal depends on the RIP of matrix A. In the following we state some conditions for measurement matrix in order to have RIP.

Consider the following $M \times N$ matrices [115]:

1. The matrix consists of N column vectors sampled uniformly and randomly on the unit sphere of $\mathbb{R}^M$.
2. The matrix consists of i.i.d. elements having normal distribution with zero mean and ${}^1/_M$ variance.

3. The matrix consists of i.i.d. elements having symmetric Bernoulli distribution or other sub-Gaussian distribution.

If M (number of samples) satisfies the following inequality

$$M \geq C \times S \times \log\left(\frac{N}{S}\right) \tag{4.15}$$

then the matrix has the RIP with overwhelming probability (C is a constant that depends on the way the matrix is formed).

If we have a fixed matrix Ψ and another matrix Φ that is formed based on conditions above (1, 2 or 3), then matrix $A = \Phi\Psi$ also have the RIP property with overwhelming probability, providing condition (4.15). So if Ψ is the basis that the signal is sparse (fixed matrix but not necessarily known matrix) and Φ be a random measurement matrix formed based on the conditions above (1, 2 and 3 and (4.15)), then the matrix $A = \Phi\Psi$ holds the RIP with overwhelming probability. Another consequence is that the measurement matrix can be designed nonadaptively, i.e. without knowing that in which domain the signal is sparse.

Condition (4.15) gives a boundary of the minimum number of samples in compressive sampling technique. To give a rule of thumb for compressive imaging systems in practice, assume that the image can be estimated by K wavelet coefficients; then one roughly needs $5K$ measurement with compressive imaging system in order to reconstruct an image with the same quality of image approximated with K wavelet coefficients [148].

In practice we need to consider practical limitations of implementing the measurement matrix. In our work we chose to use scrambled Hadamard codes, which

have the randomness property and it was shown that can be used in compressive imaging systems [131].

The algorithm chosen for optimization is NESTA [149]. NESTA is written based on Nestrerov algorithm [150] (thus the name NESTA) for solving problems with incomplete measurements. The NESTA algorithm has the advantage of high speed (therefore convenient for large scale problems), few numbers of parameters, and flexibility to solve both l_1-minimization and TV-minimization.

In our work we mainly use TV norm since we work with the images and it was shown that the TV norm works equivalent or better that l_1 norm for image reconstruction [151]. Our preliminary results also showed that the results from TV norm and l_1 norm have the same image quality.

4.2. Compressive Imaging

In conventional imaging systems usually an image is captured and then compressed. This process brings up a question if there is a way to capture the image directly in a compressed form; so there is no need to process the raw image and compress it, which takes extra time and energy. Compressive sampling is the answer to this question. It can be shown that if an image is sparse in some bases (and this is why the image can be compressed), one could use the concept of compressive sampling and sample the image in a random linear projection fashion and then use a minimization method to reconstruct the signal.

Another challenge in the area of imaging is lack of camera or high resolution cameras for some regions of electromagnetic spectra. For example, in terahertz and millimeter waves there is no commercial camera available and in IR wavelengths cameras are

expensive and their spatial resolutions are less than what is available in the visible region. Compressive imaging has the capability to address this issue, too. In single pixel compressive imaging only one detector is used to capture the light from the object or scene and after collecting enough samples, the full image can be reconstructed. Compressive imaging also can be used to increase the speed of imaging in some applications like MRI [152], [153], [154], [155].

One of the early works, done for realization of the concept of compressive imaging, was conducted by Wakin et al. [156]. They proposed an imaging system in which reflected light from the object is multiplied by a random code and then captured by a single detector. This is done by a light modulator (DMD) whose pixels reflect light to the detector according to random codes. The setup of their system is shown in Figure 60. The object is illuminated with a LED and the resulting image has the resolution of 64×64. Figure 61 shows the results of the compressive imaging system. As it is seen the image "R" is recovered. With increasing the number of measurement the quality of the

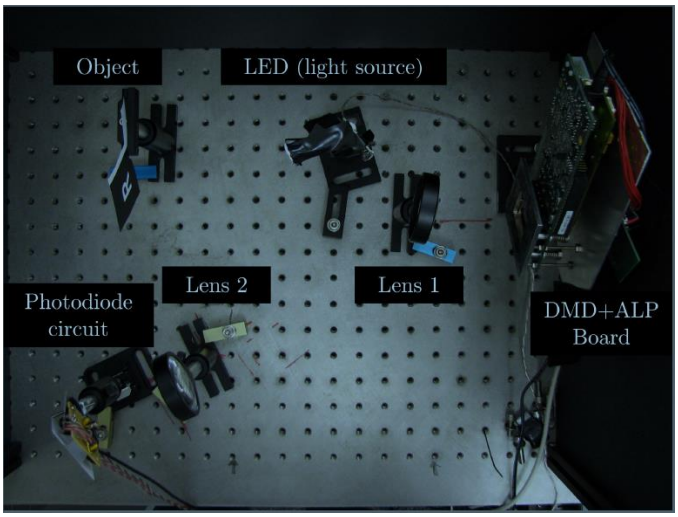

Figure 60: Compressive imaging hardware setup introduced by Wakin et.al. [156].

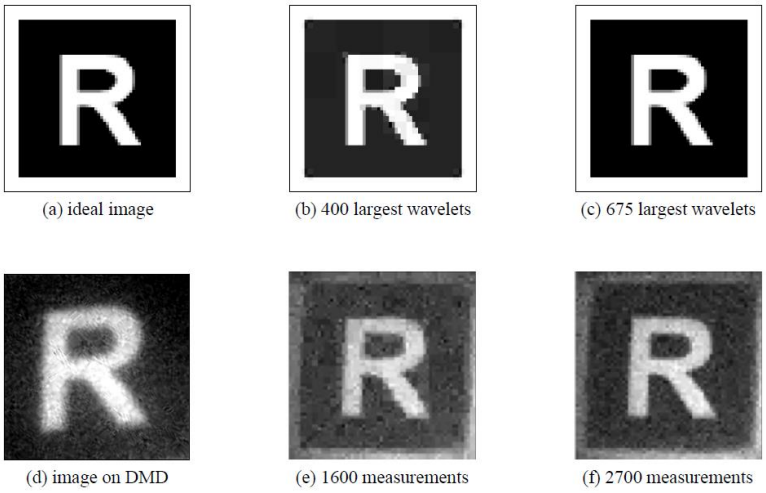

Figure 61: The results of compressive imaging system depicted in Figure 60 [156].

reconstructed image is enhanced. The quality of the results of the compressive imaging system does not strictly limited by the RIP and sparsity of signal, but it also depends on the alignment of the optical system, calibration of the system, quantization error, etc. [157].

Since the first compressive imaging system, plenty of compressive imaging systems have been emerged.

Gan [158] proposed a block compressive imaging method where the scene is captured block by block by compressive imaging technique. The advantage of this technique is the reduced implementation cost. The smaller size of each block gives the faster reconstruction and less memory usage, while the bigger block size results in better image reconstruction quality. The results for two images of boat (512x512) and Man (1024x1024) are given in Figure 62. As it is seen the results of scrambled block Hadamard are comparable to that scrambled Fourier ensemble, while the scrambled block Hadamard ensemble has much less complexity for implementation.

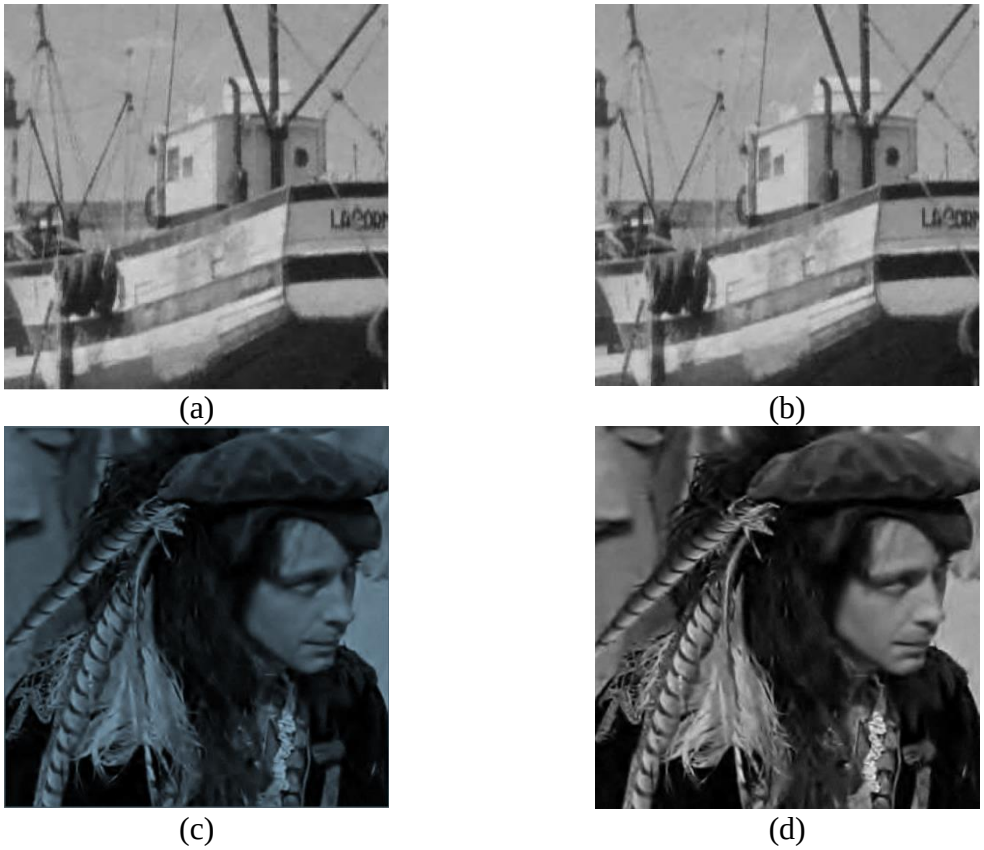

(a) (b)

(c) (d)

Figure 62: The reconstructed image using scrambled Fourier ensemble (SFE) and scrambled block Hadamard ensemble (SBHE) using block size of 32 [131]: (a): The reconstructed boat image of size 512x512 compressively sampled using SFE. (b): The reconstructed boat image of size 512x512 compressively sampled using SBHE. (c): The reconstructed Man image of size 1024x1024 compressively sampled using SFE. (a): The reconstructed Man image of size 1024x1024 compressively sampled using SBHE.

In another work, Gan et al. [131] proposed scrambled Hadamard codes for compressive imaging. Those codes are made from randomly permuting the columns of a partial block Hadamard matrix. The Hadamard codes are binary and therefore convenient to be implemented in optical domain using for example DMD. They showed that those integer-valued codes have performance compared to dense scrambled Fourier ensemble which has floating point accuracy and high computational cost. Thus the scrambled Hadamard codes have the property of having near optimal performance and fast computation along with universality and requiring small amount of memory.

Shishkin [159] also used a mixed Hadamard sensing matrix along with TV minimization for compressive imaging and showed that those codes result in faster algorithms with high quality reconstructed images. The mixed Hadamard codes are made by multiplying each element of the Hadamard code with a stochastic variable with the values ± 1 with probability of $1/2$. Figure 63 shows the results of this technique with different sampling rate and noise level. As it is seen even for low rate 6%, the results have acceptable PSNR of 23dB.

Rivenson and Stern [160] introduced separable sensing operator for compressive imaging that significantly lower the complexity of compressive imaging for large images at the cost of acquiring more samples. Figure 64 shows the image of a man and the reconstructed image with separable sensing technique. As it is seen, the image reconstructed using 430x430 samples (compression ratio of $\frac{1024^2}{430^2} = 5.67$) has a perfect reconstruction (PSNR = 244 dB).

Nagesh and Li [161] proposed architecture and a reconstruction algorithm for compressive imaging of colored images. They use a DMD for applying the codes and

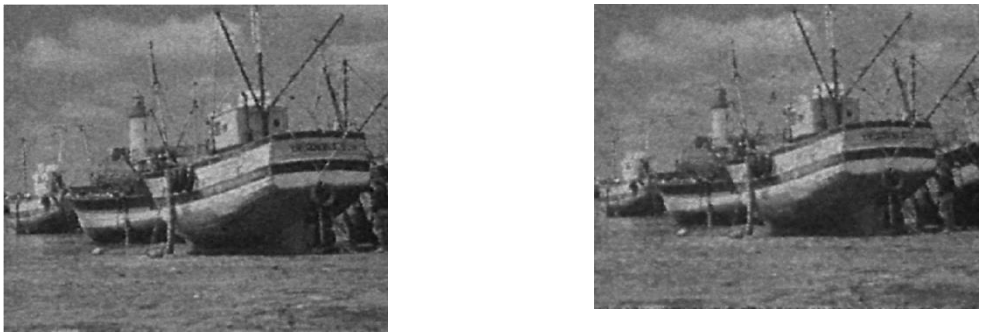

(a) (b)

Figure 63: The results of compressive imaging using mixed Hadamard codes and TV minimization for boats image of resolution 1024x1024 [159]: (a): sample rate: 10%, noise: 10%,PSNR: 25dB. (b): sample rate: 6%, noise: 10%,PSNR: 23dB.

(a) (b) (c)

Figure 64: Reconstruction of image of a man (1024x1024): (a):original image approximated with 25,000 Haar wavelet coefficient; (b): reconstruction from 430x430 sample (PSNR =244 dB) and (c): reconstruction from 350x350 samples (PSNR =27 dB) [160]

assign each pixel of DMD to a color (red, blue or green) to simulate a virtual Bayer filter (Figure 65.a). For each sample a random code is applied to the DMD and they use a rotating color filter to choose one color associated to each sample. The rotating color filter is located between the object and the DMD (Figure 65.b); and for each color, the DMD pixels with the same color label will be active and the pixels with other color labels will be off regardless of the value of the random code assigned to that pixel. After acquiring enough samples the color image is reconstructed.

Zerom et al. [162] demonstrated high-resolution quantum ghost imaging with the use

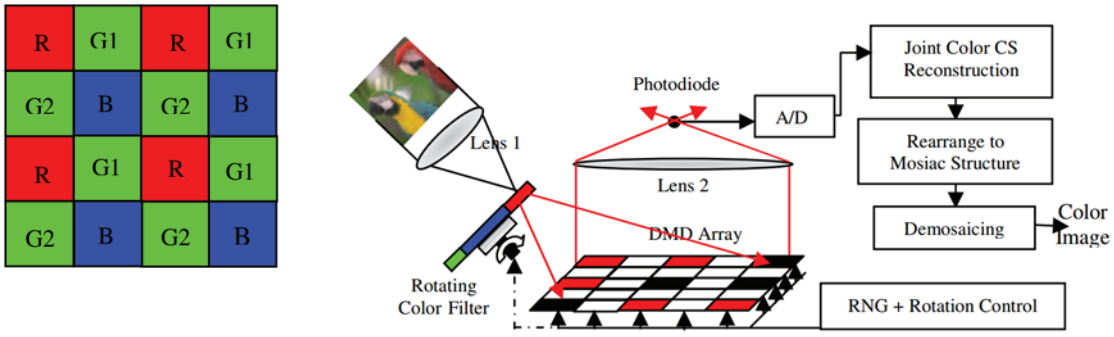

(a) (b)

Figure 65: (a): Virtual Bayer Filter structure on the DMD; (b): color CS camera structure [161].

of compressive imaging. They reported that their technique both reduces acquisition time and use photons more effectively.

In the field of medical imaging, there are also plenty of works related to compressive imaging. Lustig et al. have a series of papers that propose methods for rapid MRI imaging [152], [153], [154], [155]. Their method is based on randomly selected pixels in k-space and reconstruction with l_1 minimization or TV minimization. With these techniques the image can be acquired faster and with relatively better quality.

There are some works in implementing the compressive imaging on a CMOS sensor. Robucci et.al. [163] proposed a Separable-transform imager IC to compressively sample the image in analog domain. Figure 66 shows the block diagram of the chip. As it is seen the chip consists of a random-access analog memory, row and readout control, computational sensor element, current to voltage converter and an analog to digital converter. Figure 67 shows the result of reconstruction of an image with noiselet and DCT bases with different compression ratio.

In next chapter we describe different compressive imaging system that we have developed and demonstrate the results and outputs of each compressive imaging system.

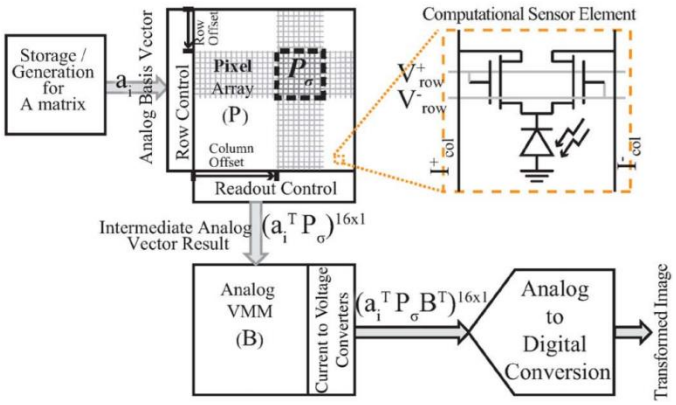

Figure 66: Block diagram of the separable-transform imager chip [163].

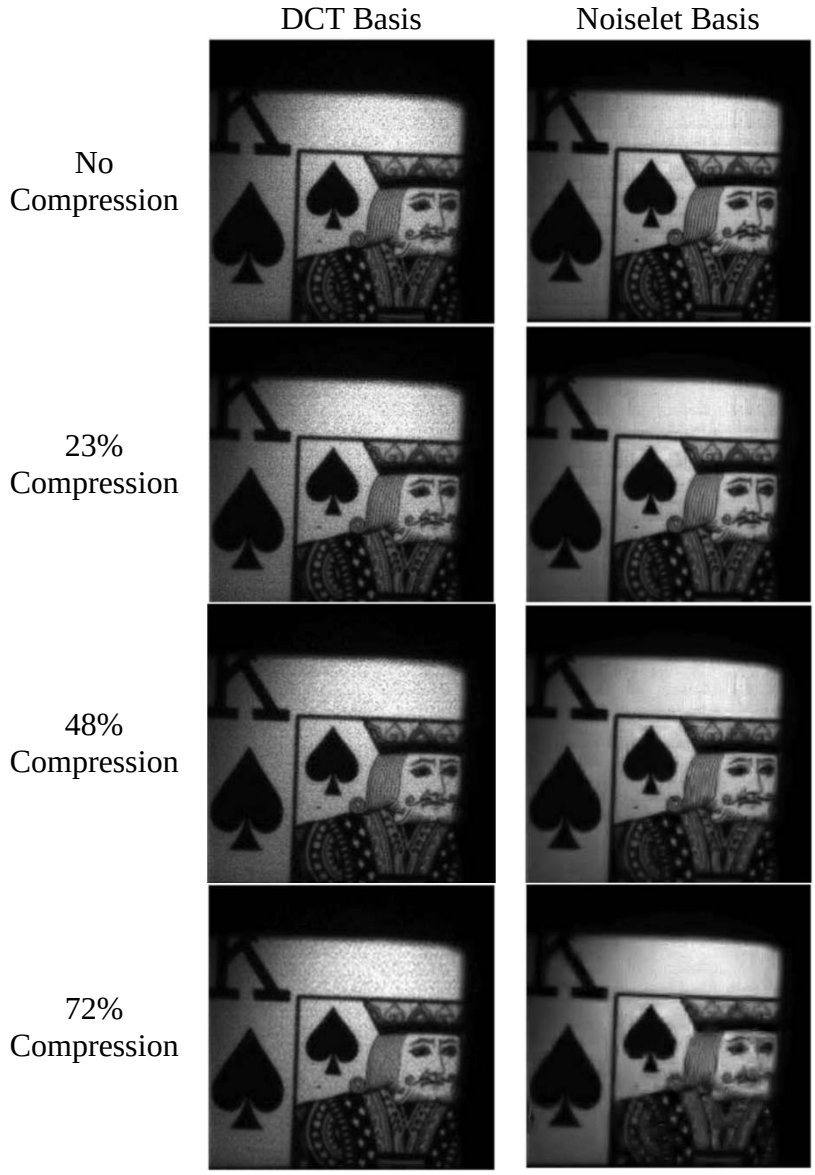

Figure 67: Reconstruction results with different compression ratio and bases for the separable-transform imager chip [163].

CHAPTER 5: COMPRESSIVE IMAGING SYSTEMS

As mentioned in the previous chapter we developed several compressive imaging systems in order to address some issues in the field of optical metrology. This chapter explains the architecture of the imaging systems and the results. We start by compressive imaging system for low light level conditions in which a DLP board is used to apply the random codes and a photomultiplier is used to collect the samples. The next system is transmissive compressive imaging system in which an LCD is used for manipulating the light according to the codes. High dynamic range compressive imaging system is the next implemented system, which two different techniques for high dynamic range imaging in the context of compressive imaging are demonstrated. The last system is a spectral compressive imaging system by employing a spectrometer instead of the photodiode.

5.1. Low Light Compressive Imaging

In conventional imaging, each pixel of camera acquires the data from corresponding point on the object. The incident light should be above a specific threshold level (which relates to the noise level) in order to have a meaningful data for the corresponding pixel. Therefore under low light conditions which there is not enough light, the captured image will be a dark image. In other words, no information will be acquired from the scene/object.

One way to overcome this problem is using single pixel compressive imaging technique. In compressive imaging, at each instant of data acquisition, light from half of the image area will be collected, on average. So, although light for one pixel is not enough for detector to reach above threshold, light from half of the total image would exceed the threshold. For example, suppose that the image is 100×100 pixels, the average light intensity per pixel under low light condition is 0.6 and the threshold is 1. This means that light for each pixel does not meet the threshold for most of the pixels. Considering compressive imaging, for each instance of data acquisition, the average light level is going to be $0.6 \times (100 \times 100/2) = 3000$ that exceeds the threshold level.

To have fairer comparison, the total data acquisition time should be considered, too. Considering the same scenario above, assume that the compression ratio is 4; it means that for reconstructing the image we need to acquire $100 \times 100/4 = 2500$ data. Assume that the total acquisition time is 1 second. This means that in compressive imaging, on average, we have $1/2500 = 0.0004$ second which leads to light intensity of $0.6/2500 = 0.00024$ per pixel. As we mentioned, at each instance of data acquisition, light intensity of half of the pixels will be collected, on average. Therefore the level of light at each instance of data acquisition would be $(100 \times 100/2) \times 0.00024 = 1.2$ which is above threshold. This means that with the same acquisition time, compressive imaging is the winner, again.

Another advantage of single pixel compressive sampling is that it uses one detector instead of array of detectors. This means that, in case of low light imaging, we can use a very sensitive detector that might not be available in the form of detector array. For

example, using an array of 100×100 photomultiplier is not a reasonable configuration, but using one photomultiplier would be a reasonable choice.

In the following we describe the experiment for low light imaging using compressive sampling.

5.1.1. Experiment

Figure 68 shows the setup for low light compressive imaging. It consists of an LED as light source, a Digital Micromirror Device (DMD) to multiply the random codes with incoming light pattern. The DMD is a unique device that consists of an array of microscopic, electrostatically activated micro-mirrors, with each mirror rotating about a hinge programmable in one of two states (+12 and -12 degrees from horizontal), so that light falling on DMD can be reflected in two directions depending on mirror orientation. The DMD equipment used is a Texas Instruments (TI) Discovery 4000 kit, consisting of a 0.7" XGA DMD with size 1024×768 pixels. A photomultiplier (PMT) and a DAQ board were used to acquire data. The LED light source was placed in front of a lens and adjusted to illuminate the object. The objects are two transparencies with a letter "A" printed on uniformly, and letters "AXB" printed on, which has a radial gradient of intensity. The incoming light after passing through the object is divided into two, using a beamsplitter. One of the outputs of beamsplitter was used to capture the image using a conventional camera and the other output was used for compressive imaging. A lens images the object on both camera and DMD which were placed equidistance. The object is imaged on DMD in order to be multiplied by the random codes. The reflected light is

collected using a lens set (an eye piece) and acquired by the PMT. PMT is a compact head-on photomultiplier PMT H7828 from Hamamatsu[20].

The PMT is a large area detector (15mm diameter) with very low level dark noise (200 photon count /sec). The output of PMT was read by a DAQ board, which is National Instrument USB Data Acquisition Board NI USB-6210[21].

Since the experiment is for low light imaging and PMT is very sensitive to light, the experiment was done in a dark environment to reduce the effect of ambient light that interfere with the experiment. Also the setup was covered by a black housing.

The light intensity of LED was set at different levels to compare the results of conventional and compressive imaging. The level of light intensity was changed by changing the current of LED.

The codes that were used in our experiment are scrambled Hadamard Codes [131]. The length of each code was 128×128, which is the same as the number of pixels of the image. The codes were first generated offline and saved on the computer. Then during the experiment the generated codes were buffered and loaded on DMD using a MATLAB interface. Codes consist of a series of zeros and ones. If one is assigned to a pixel, the corresponding micromirror on the DMD is rotated in a way that reflects light toward PMT and therefore the light from corresponding pixel will be collected by PMT. If zero is assigned to a pixel, on the other hand, the corresponding micromirror is rotated in the opposite direction and reflects light to an absorber, which absorbs lights in order to reduce the noise level of the imaging system.

[20] http://sales.hamamatsu.com/en/products/electron-tube-division/detectors/photomultiplier-modules/part-h7828.php
[21] http://sine.ni.com/nips/cds/view/p/lang/en/nid/203223

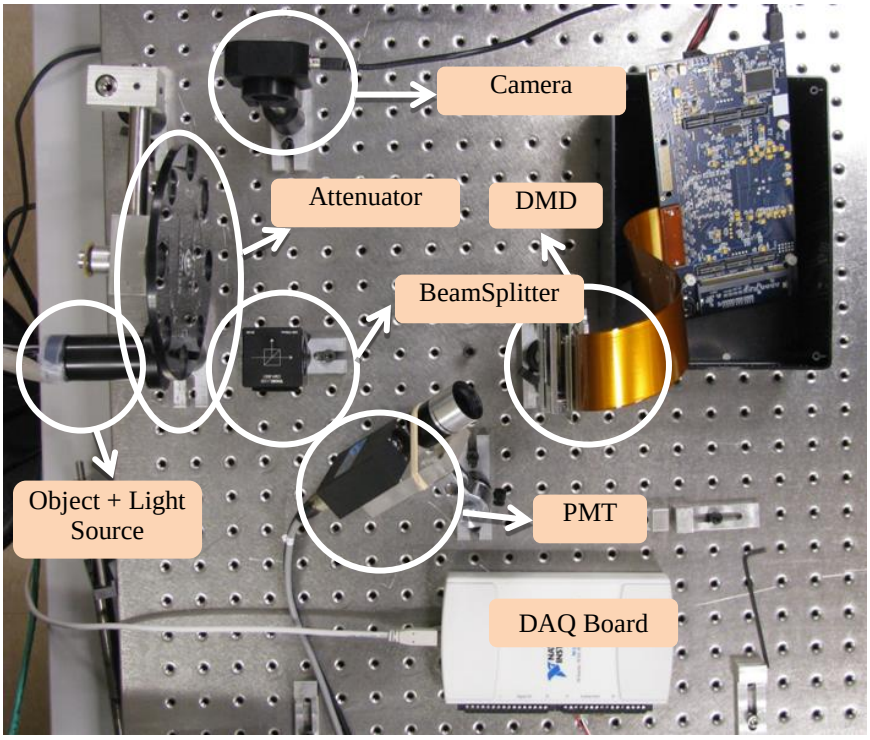

Figure 68: Setup for low light level compressive imaging

To determine bias value caused by the background light, a voltage measurement with DMD loaded with a black image (all *zeros* code) was taken. This bias value was deducted from each measured voltage in the above experiment to remove background. Another measurement was taken with DMD loaded with white image (all *ones* code), in order to determine mean intensity. Both these values were used to modify the data with scrambled Hadamard codes.

After obtaining voltage measurements generated by each code, the NESTA algorithm [149] was applied to the collected data to reconstruct images at various light intensity settings.

5.1.2. Results

The object was a character "A" printed on a transparency and illuminated from the back. The codes, as mentioned, are 128×128 scrambled Hadamard codes. Normal

intensity, low intensity and very low intensity refer to the relative illumination of the object. In a normal condition camera was set to gain of one and exposure time of 300ms. In low intensity and very low intensity camera is set to the highest gain level (128) and the highest exposure time (560 ms).

Figure 69 shows the results of experiment under normal, low light and very low light conditions. Under normal light intensity, image from camera and reconstructed images using compressive imaging both have acceptable qualities and show edges and tone of the object.

Under low light intensity captured image with the camera just shows a ghost of the object, while reconstructed image with compressive imaging technique is better representative of the object, it shows clearly the edges of the right side of the object and less clear the left side of the object.

Under very low light conditions, captured image with camera is a dark image and does not contain any information from the object. The reconstructed image with compressive imaging shows the object. Again the right side of the object is clearer than the left side of the object.

Under low and very low light conditions, the amount of light is not enough for camera to capture a recognizable image from the object. The compressive imaging setup collects the light from all over the object and by using the photomultiplier, the small amount of collected photons are multiplied to result in an image with recognizable object. The quality of the reconstructed image can be further improved by reducing the ambient noise. Even small number of unwanted photons can results in a noise level at the output of photomultiplier, which degrades the quality of reconstructed image.

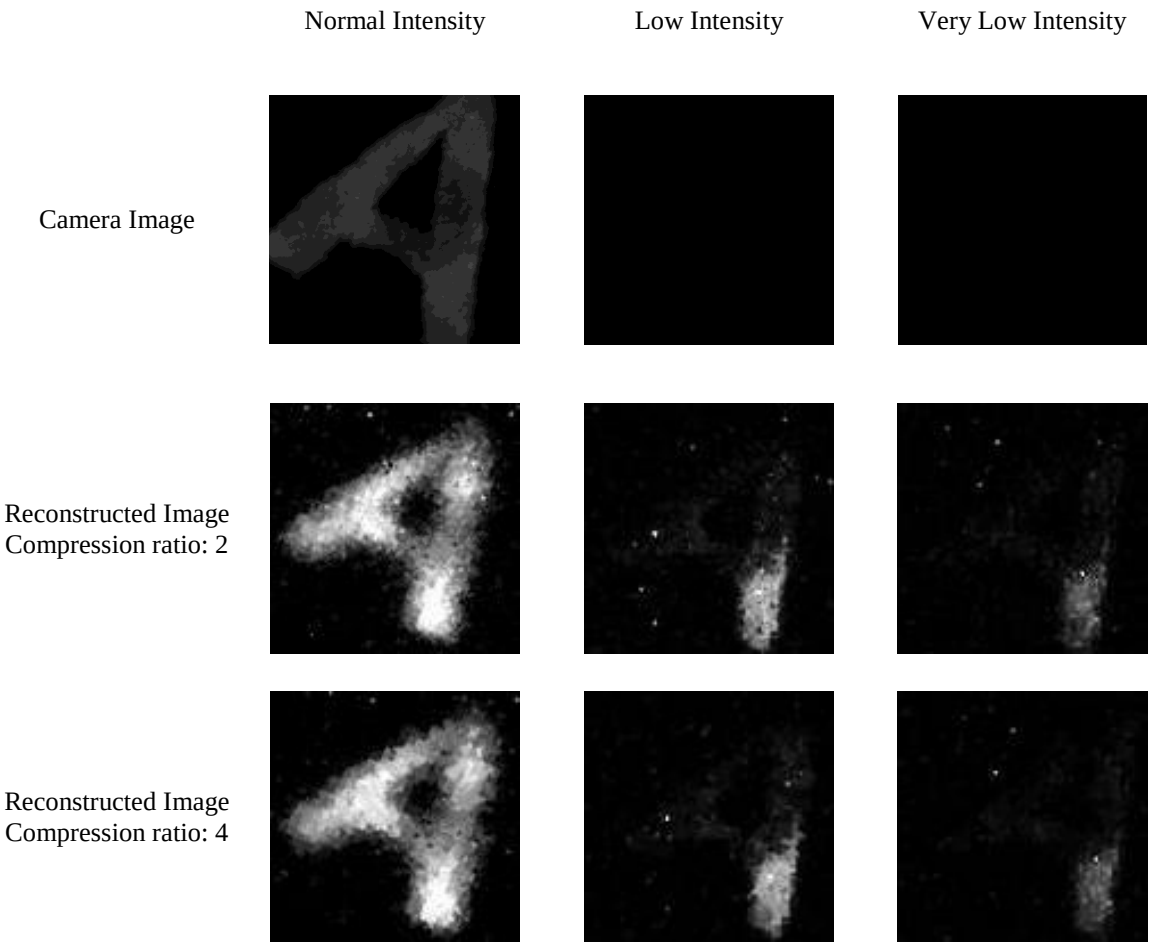

Figure 69: Results of low light compressive imaging

5.2. Transmissive Compressive Imaging

The compressive imaging in transmissive mode has the benefit of easy optical alignment. Figure 70 shows the schematic of a transmissive compressive imaging system. The object in this configuration was a transparent object and therefore it needed to be illuminated from the back. The object was imaged on the SLM using a lens system. The purpose of the SLM is to modulate (multiply with codes) the imaged object. The coded object was focused on a single detector that collected the light. The output of the detector, which is a number (voltage value) was saved for image reconstruction.

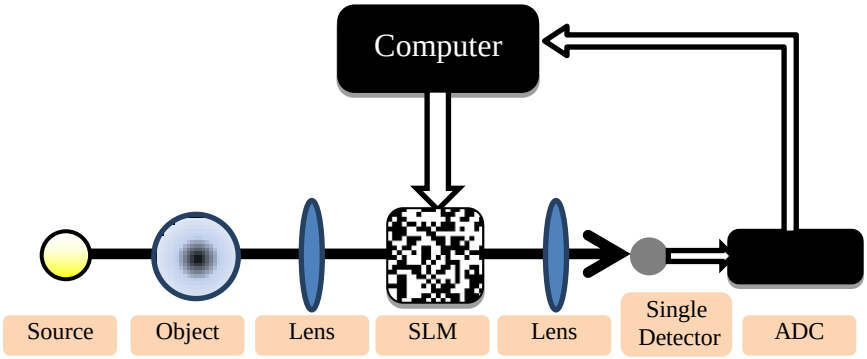

Figure 70: Schematic of a transmissive compressive imaging system

5.2.1. Experiment

Figure 71 shows the implemented transmissive compressive imaging system incorporated into a microscope. An LCD was placed where the image of the object is usually formed. For a one-to-one comparison, a conventional camera captures the imaged object. The imaged object on the LCD was then multiplied by several random codes. The codes were applied as the values of each pixel of the LCD. The codes that we have used are binary codes (scrambled Hadamard codes). Value one means that the corresponding pixel passes the light and value of zero means that the corresponding pixel blocks the light. A photodiode with large area was placed right after the LCD to capture the light passing the LCD. The output of photodetector was amplified and was converted to a digital number using a DAQ board. The stored values and their corresponding codes were used to reconstruct the image.

The LCD, having a maximum resolution of 800 × 600 pixels (active area: 11.2 mm × 8.4 mm = 94.08 mm^2), was taken from an Epson® PowerLite S5 projector. The central part of LCD (512 x 512 pixels) was used to apply the random codes. The photodiode (Si) is a Thorlabs FDS1010 (active area: 9.7 mm × 9.7 mm = 94.09 mm^2). The active areas of

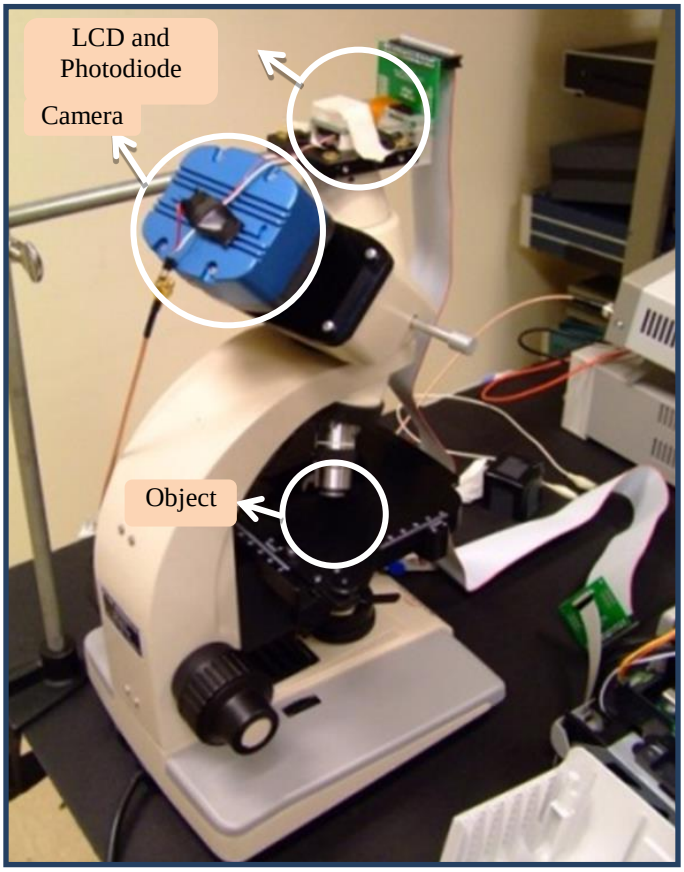

Figure 71: Transmissive compressive imaging system

LCD and photodiode confirms the suitability of the LCD and the chosen photodiode to be used together to spatially encode and measure the light, respectively.

5.2.2. Results

One of the scenes acquired with our imaging system in transmission mode is represented in Figure 72. Since the conventional camera sensor size (1/2” CCD) was smaller than the LCD size, we had to stitch 4 separate pictures taken with the conventional camera in order to get an image containing the single-pixel camera field of view. For the case of the singe-pixel camera, ideally, its field of view would correspond to the size of the LCD. In particular, the actual field of view was defined by a 512 × 512 pixels region centered on the LCD active region.

Figure 72: Object is a printed “on” letters. The region inside the box is the part that is sampled and reconstructed using transmissive compressive imaging system.

The results presented in Figure 73 correspond to reconstructions of the scene contained within the blue square of Figure 72. From the analysis of these results, it is clear that the quality of the reconstructed images increases with the growth of the number of measurements used for reconstruction. This fact is supported by the PSNR (Peak Signal-to-Noise Ratio) values presented for each of the reconstructed images relatively to the image of the same size reconstructed using maximum samples possible.

The transmissive compressive imaging has the disadvantage of lower signal to noise ratio when it is compared to the compressive imaging systems employ DMD. The reason

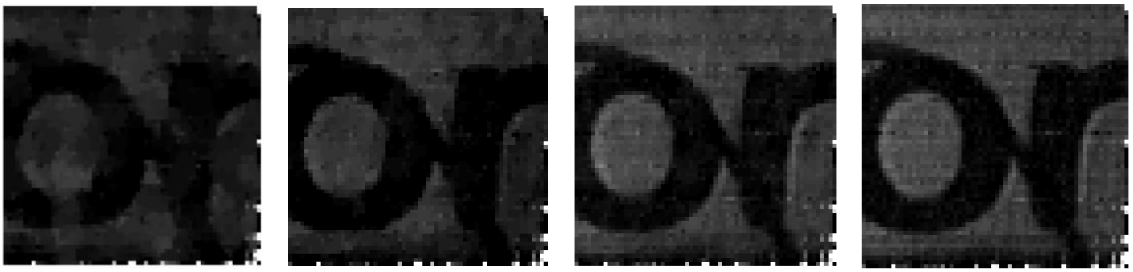

(a) (b) (c) (d)

Figure 73: Reconstruction of image with the resolusion of 64×64 pixels with (a): compression ratio of 4 ($\frac{64\times64}{4} = 1024$ samples) and PSNR = 20.27 dB, (b): compression ratio of 2 ($64 \times \frac{64}{24} = 2048$ samples) and PSNR = 22.63 dB, (c): compression ratio of 1.33 ($64 \times 64 \times \frac{3}{4} = 3072$ samples)) and PSNR = 32.44 dB, and (d): compression ratio of 1 ($64 \times 64 = 4096$ samples). All PSNR are calculated with respect to (d).

is that the LCD does not block the light completely when the corresponding pixel is zero. Therefore there is always some background noise. The LCD also does not black the near infrared light that was present in our light source which again adds to the background noise.

5.3. High Dynamic Range Compressive Imaging

One of the limitations of imaging systems is their dynamic range. Scenes in real world usually have broader range of intensity variation than conventional cameras could accommodate. Therefore, full representation of a scene that has regions with both very high and very low radiances is not possible with conventional cameras. High Dynamic Range Imaging (HDRI) addresses this issue [164], [165], [166].

Applications of combining high dynamic range imaging and compressive imaging include scenarios where we have high contrast ratio scenes and/or objects, radiation wavelength is out of the range of the wavelengths that conventional cameras are sensitive to, and in situations where speed of capturing image is important.

In the next section first high dynamic range imaging will be explained and then combination of high dynamic range imaging and compressive imaging will be demonstrated with two different methods.

5.3.1. High Dynamic Range Imaging

Many objects and scenes exhibit a broad range of brightness. This might be because of the range of colors, different reflection or transmission coefficient, illumination pattern, etc. In a typical digital camera, the value for each color (red, green and blue) is stored using 8 bits; assuming that minimum intensity is equal to one and maximum intensity equals to 255, the dynamic range of camera is about 48 dB for each color. To

capture a scene that requires a dynamic range of more than 48 dB for each color, there is a need for a new imaging technique. One of the most popular methods is to capture images of the same scene with different exposure times/gains and then combine the resulting images to construct an image with HDR [164], [165].

One of the first works in this area has been done by Mann [167], [168], who proposed an algorithm to combine different images of the same scene captured with different exposure times, to construct an image with HDR. The proposed combination algorithm is based on a certainty function, which is the derivative of the camera's response function. Another work in this field was reported by Madden [169] where, once again, multiple images of a scene are captured with a CCD for different exposure times. The exposure time was changed such that at minimum exposure time there was no saturated pixel and at maximum exposure time some pixels become saturated. By examining each pixel at different exposure times we realize that pixels might be saturated at long exposure time and their values become the maximum allowable; remain dark due to either short exposure time or simply lack of any light; or would take values below saturation and above noise level. To construct the final HDR image, the value for each pixel of HDR image is chosen from the image that its corresponding pixel value is below saturation and most precise due to its minimum quantization error. Figure 74.a shows four images taken at different exposure time (from 4μsec to 32msec) and Figure 74.b shows the combined HDR image. As it is seen the combined image has the details of both images with low exposure time and high exposure time.

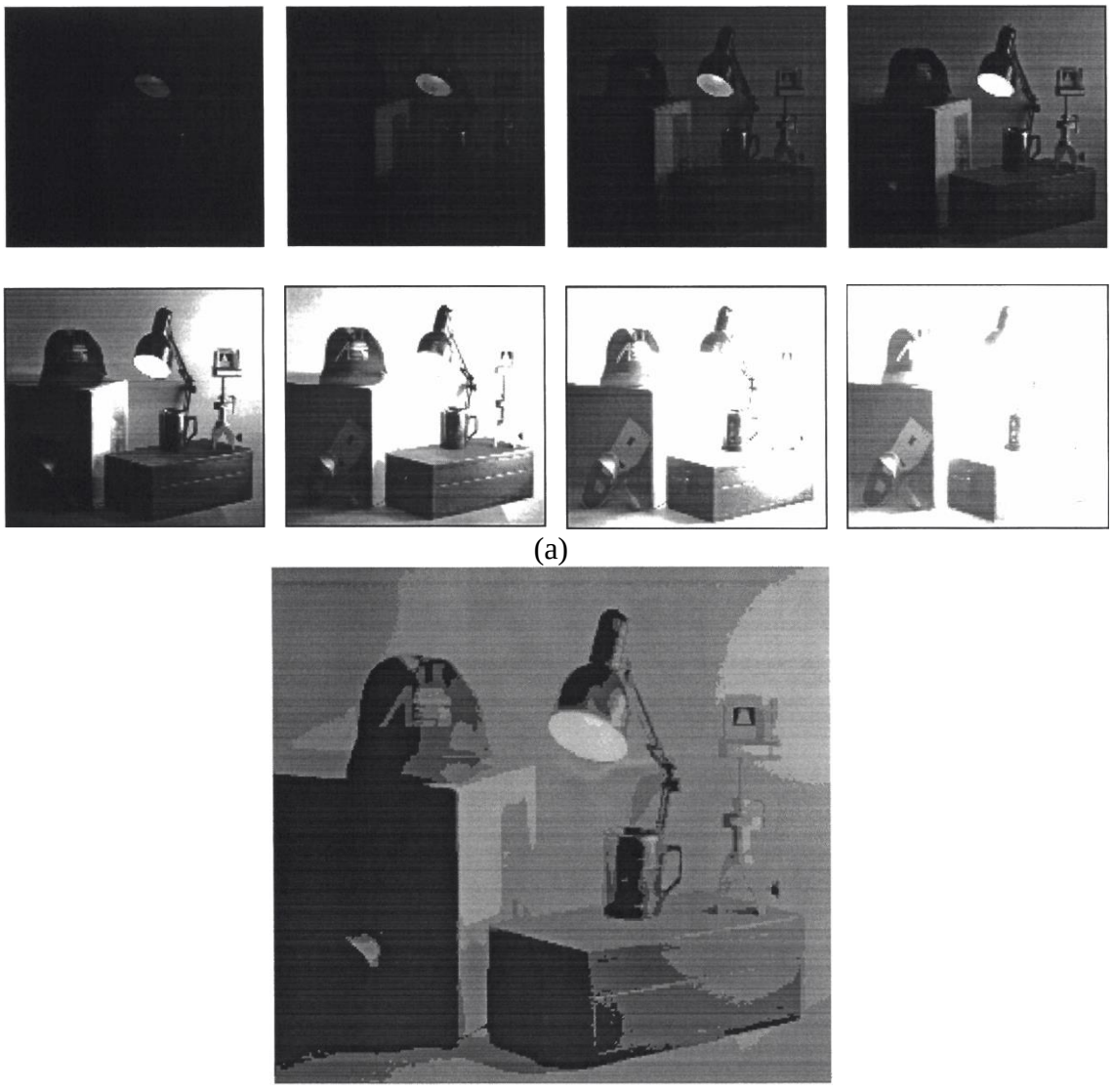

Figure 74: High dynamic range imaging technique; (a): Images taken at different exposure time and (b): Composite image [169].

Yamada et al. [170] worked on dynamic range extension of TV cameras for vehicles. They used the same principle of getting several images with different exposure times and combine them into one enhanced image with high dynamic range. Figure 75.a shows the block diagram of their developed system. Figure 75.b shows the image of a tunnel exit captured by a conventional camera and Figure 75.c is captured by their HDR imaging

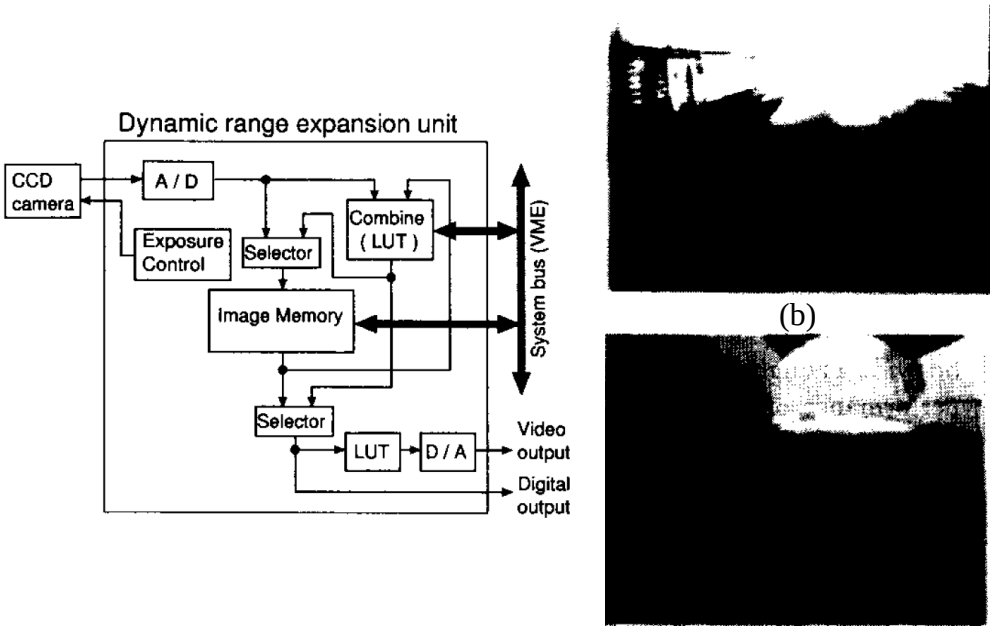

Figure 75: HDR imaging system developed by Yamada et.al. [170]. (a): Block diagram of developed vision sensor system, (b): image of tunnel exit taken with a conventional camera and (c): the same scene taken with the developed HDR imaging system.

system. As the figure shows, the HDR image shows the details of the tunnel exit where the image of conventional camera is saturated.

There are also some works on extending the dynamic range of color images. Moriwaki [171] used the same principle of combining images with different exposure times and constructing an adaptive exposure color image. It was shown that the constructed image has better accuracy in applications like color discrimination. A work reported by Debevec and Malik [164] uses images with different exposure times to find the response function of the imaging process up to a scale factor and then use this response function to construct HDR images. Figure 76 shows the images taken from inside a church with different exposure time (from 1ms to 30 sec). The images are used to calculate the response curve for each color (red, green and blue). The curves are shown in Figure 77. From the response curve a high dynamic range image is calculated and the

Figure 76: images taken from a church with different exposure time (from 1 ms to 30 sec.) [164].

tone mapped image is demonstrated in Figure 78.b. Comparing that image with the image from a conventional camera (Figure 78.a) shows that the HDR image shows more details both in the dark area and bright areas.

Mitsunaga and Nayar [172] used images obtained with different exposure times to calculate the response time of the imaging system. The ratio of exposure time only needs to be known to accurately recover the response function.

Another technique for improving dynamic range of an image is to change the exposure time or intensity of each pixel individually. Nayar and Mitsunaga [166] proposed an imaging system where neighboring pixels have different exposure times.

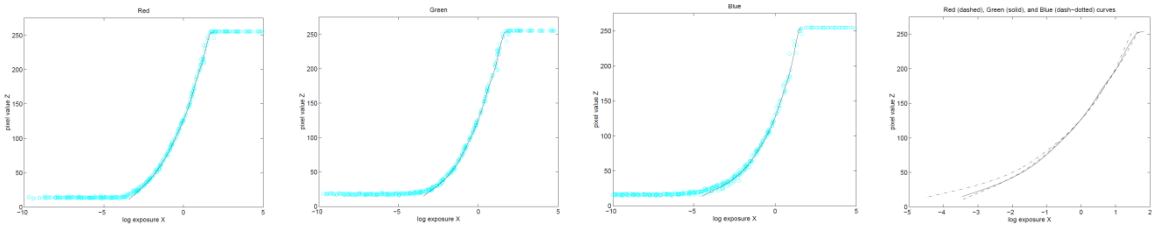

(a) (b) (c) (d)

Figure 77: Response curve calculated for the imaging system that has taken images in Figure 76; (a): red channel response curve, (b): green channel response curve, (b): blue channel response curve, (b): all three curves in a single diagram [164].

(a) (b)

Figure 78: (a): Photograph taken with conventional camera and (b): Tone mapped high dynamic range image [164].

Their system was implemented using a mask with different transparencies in front of the detector. Therefore with a cost of decrease in spatial resolution a high dynamic range image can be calculated with a single shot with that spatially varying pixel exposure imaging system. Figure 79.a-d show four images that are taken with different exposure times. As it is seen the scene has wide dynamic range of intensity. Figure 79.e shows the image that is taken using the proposed imaging system and Figure 79.f shows the computed image. As it is shown the computed image shows the details of both dark and bright regions of the scene.

Mannami et al. [173] proposed HDRI by means of a reflective liquid crystal light modulator. They used an LCoS (Liquid Crystal on Silicon) as a spatial light modulator in front of a camera to spatially modulate the intensity of each pixel. Figure 80.a shows the

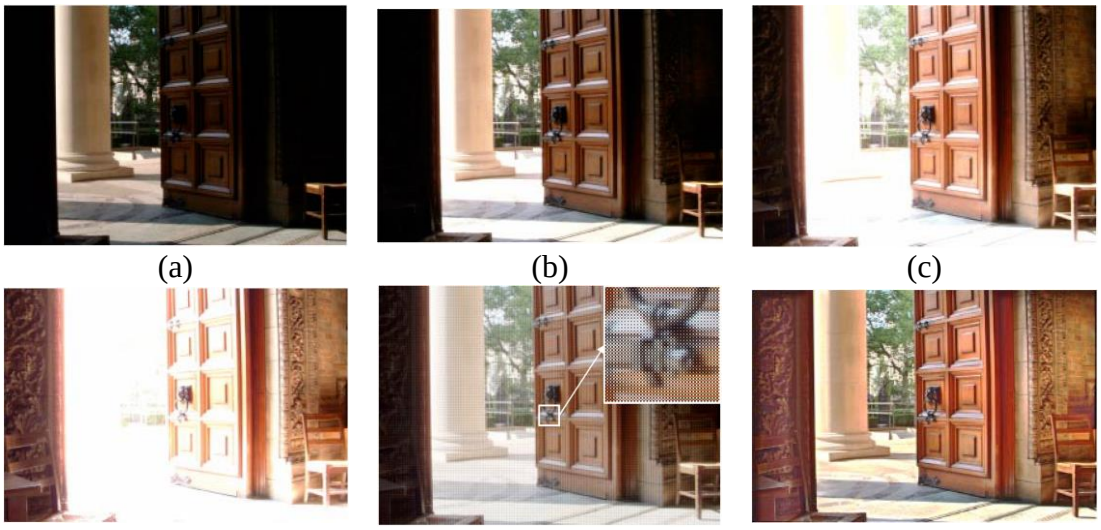

Figure 79: Results of spatially varying pixel exposure imaging system: (a)-(d) are images taken at exposure time 1T, 4T, 16T and 64T, correspondingly; (e): image taken with spatially varying pixel exposure imaging system and (f): computed image from image taken with spatially varying pixel exposure imaging system [166].

schematic of the imaging system. The incident light first illuminate the LCoS where it can be controlled at pixel level and then the manipulated light is captured by the camera. One of the issues here, to obtain good results, is geometric alignment between the pixels of camera and LCoS. They used homography for geometric calibration. Also, an off-line calibration was conducted to infer the radiometric properties of the system. At each step they changed the values of the LCoS pixels in a way that the values of corresponding camera pixels became equal to an optimum value. This optimum value is the value that corresponds to optimum radiance. Figure 80.b shows an image that is taken when the radiance control is off (LCoS does not manipulate the incident light). As it is seen there is a large contrast between black and white (possibly saturated) regions. To decrease the radiance in the white region, LCoS reduces the radiance in the bright region which results in lowering the contrast (Figure 80.c).

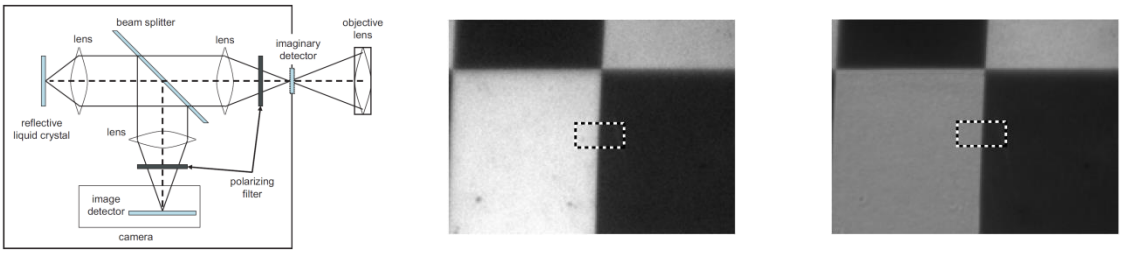

(a) (b) (c)

Figure 80: Results of HDR imaging system using LCoS proposed by Mannami [173]; (a): Schematic of the proposed imaging system, (b): image before controlling the radiance of light and (c): image after controlling the radiance using LCoS.

Adeyemi et al. [174] used a Digital Micromirror Device (DMD) to acquire an HDR in a microscopy system. Figure 81.a shows the schematic of the HDR imaging system. They also used the geometrical calibration for corresponding pixels of camera and DMD. Also, DMD is characterized for its reflected power vs. the digital values of DMD pixels. Figure 81.b-f shows the images that are taken successively in order to adjust the incoming radiance in order to remove the regions with saturation. As it is seen after capturing five images there is no saturation region in the final image (Figure 81.f). They reported that

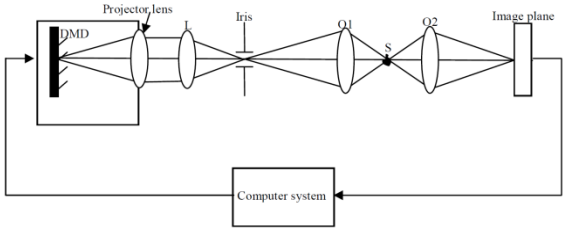

(a)

(b) (c) (d) (e) (f)

Figure 81: HDR imaging system using DMD; (a): Schematic of the HDR imaging system, (b): First captured image shows saturation in regions 1-4. (c): After adjusting the DMD, the image shows that the saturation in region 1 is no longer exist, but still there is saturation in regions 2-4. (d): captured image after second adjustment with saturations in region 4. (e): Fourth captured image with saturation in region 4 removed and (f): The last captured image [174].

with their system, in principle, they can improve dynamic range of an image by a factor of 573, although their experimental results show improvement of dynamic range only by a factor of 5.

Commercially, there are some imaging systems that directly capture HDR images including viper filmstream, SMal, Pixim and SpheronVR [165]. These cameras record the HDR images in one shot. Fujifilm also has introduced point and shoot cameras that capture HDR cameras using two images with different exposure times [175].

5.3.2. High Dynamic Range Compressive Imaging (HDRCI): First Method

In the previous section the advantages and techniques for HDR imaging and compressive imaging were explained. So, if these two techniques can be combined together in one single system we will have an imaging system that can increase the dynamic range of an image and can do the imaging faster and/or in wavelengths where conventional cameras do not work. For example, in fluorescence imaging there is a demand for a high dynamic range camera in the infrared region of the spectrum [176] at which cameras are expensive; therefore HDRCI is a solution for this type of imaging.

The HDRCI is a programmable imaging system [177]; it can control the radiometric properties of the system and uses one detector with a single pixel to obtain data and post processing to construct the image. Figure 82 shows a schematic of the proposed system. Object is illuminated by a light source and imaged by an optical system on a Spatial Light Modulator (SLM). SLM can be in reflective or transmissive configuration. The SLM acts as spatial intensity filter (second block of Figure 82.a) to change the intensity of different parts of image independently (HDR part). SLM is also used as a device to multiply different codes (third block of Figure 82.a) with the image formed on the SLM (CS part);

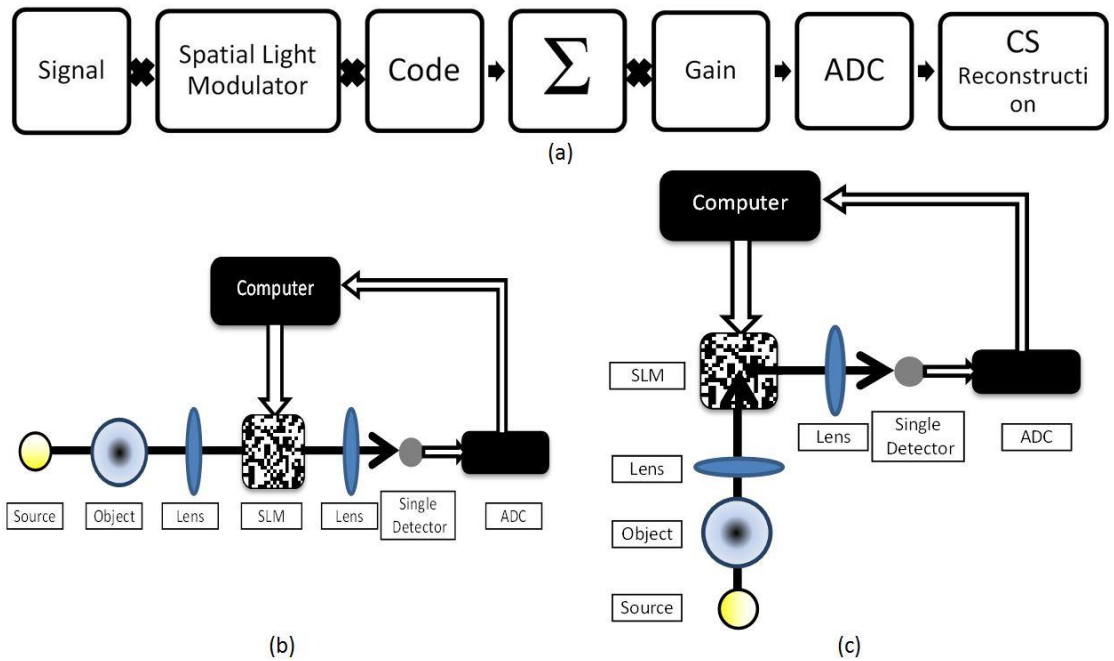

Figure 82: Schematic of HDRCI system as (a) block diagram (b) transmissive and (c) reflective configurations.

i.e. it samples the image using sampling functions/vectors, which are referred as codes. For active illumination technique that was used in the experiment, SLM is part of light source, i.e. change of intensity of different parts of image and multiplication of codes is done in light source and therefore the projected light is manipulated before illuminating the object. After applying sufficient number of codes and acquiring corresponding data, the acquire data is used to reconstruct the image.

One issue in HDRCI is defining a meaningful parameter that is a measure of the dynamic range of the final image. For conventional imaging, dynamic range is defined as the ratio of maximum intensity and minimum intensity. For a digital camera, dynamic range is limited by noise including quantization noise, shot noise, read-out noise, etc. In HDRCI, the noise of acquired data is not the final image noise, but the pixels' values and therefore image noise are calculated from acquired samples through an optimization

algorithm. Therefore, we need a new definition for minimum level of intensity other than noise. Obviously, our definition for the minimum level of intensity should be based on noise level of the system calculated for the reconstructed image. To practically measure that noise level, the HDRCI system will be run without input; namely a black object is used as input and the reconstructed signal will be considered as output noise. The standard deviation of this output noise is considered as the noise level or minimum intensity; i.e. this is the threshold in which every signal below that is considered as noise and its corresponding pixel is considered a dark pixel[22].

Based on this definition, the aim of HDRCI system is to bring pixels of image above minimum level of intensity (excluding dark pixels), while avoiding saturation for pixels with high intensity. In other words, HDRCI captures information from wider range of intensity levels than a CS imaging system and this means higher dynamic range.

As it was mentioned before, in conventional imaging, image with high dynamic range could be obtained if exposure times for all pixels or a set of pixels are changed. One of the basic differences between conventional imaging and HDRCI is the fact that the exposure time for HDRCI does not apply to a single pixel, but to an ensemble of pixels. Therefore a parameter equivalent to exposure time has to be defined for HDRCI.

This parameter can be defined as a combination of ADC (Analogue to Digital Convertor) gain level and a mask to select an ensemble of pixels. In other words, for changing the exposure time, first we block/unblock a group of pixels and increase/decrease the gain of ADC. Therefore in analogy to conventional HDR imaging,

[22] Note that the proposed technique to measure noise level does not consider the signal noise, i.e. the noise that comes from the light source itself, but the definition of minimum intensity which corresponds to the noise level is not limited to only measurement noise and can include all other noises including signal noise.

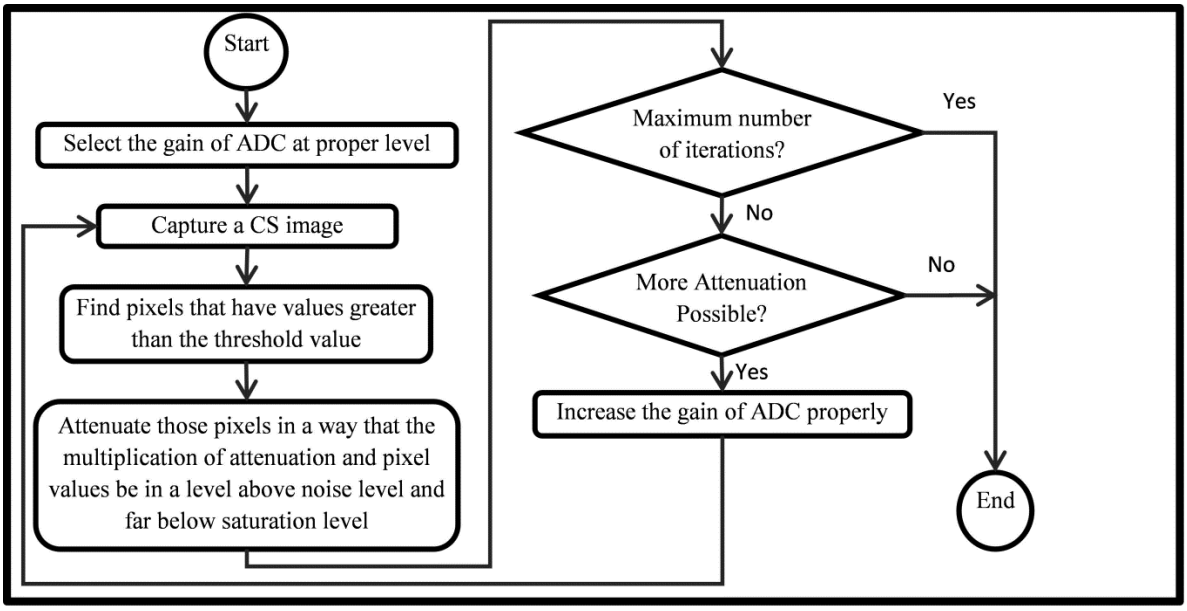

Figure 83: Flowchart of high dynamic range compressive imaging algorithm

We introduce the following algorithm for HDRCI (Flowchart of the algorithm is given in Figure 83): First, we choose the gain of ADC at a proper level. The proper level at this step can be defined as a level at which the number of saturated samples is some small percentage of total samples. When this is between 10 to 30 percent the performance is satisfactory [178]. Second, an image using compressive imaging technique is constructed. Pixels that have values greater than a threshold value are identified. This threshold value can be defined based on the histogram of the reconstructed image or based on some other statistics of the reconstructed image. Next, the identified pixels with values greater than the threshold are attenuated in a way that their values reach above the noise level and far below saturation. This level depends on the number of steps the algorithm will iterate and the amount of increase in the ADC gain. For example, suppose that the number of iterations for the algorithm is 2; and each pixel of the attenuator has 8 bits. Therefore, in average, for each iteration 4 bits can be used, and this equals to an

attenuation factor of 2^4=16. Hence, a pixel with maximum intensity (or saturated pixel), can be reduced by a factor of 16 relative to the highest possible level (saturation level). The level of ADC gain will be determined accordingly, based on the percentage of attenuation for the whole image. For instance, if the average attenuation of image intensity is 80 percent (this means attenuation factor of $\frac{1}{1-\frac{80}{100}} = 5\,\frac{1}{1-\frac{80}{100}} = 5$), then the gain of ADC will be increased by a factor of 5. As the gain of ADC changes, the noise level will also change and this will affect the noise level of quantized samples. This can be avoided if we suppose that the dominant noise of quantized samples is the noise of the ADC for all gain levels and therefore increasing the gain of ADC does not change the noise level significantly. This is an acceptable assumption for implemented system[23].

With this scenario, the pixels with lower intensity have better chance to participate in each sample of CS imaging and therefore better chance to rise above noise level after reconstruction. Since the resultant images at different exposure times (or different gain) are the same as images acquired in HDR imaging, the same technique for combining and constructing final HDR image in conventional HDR imaging can be used in HDRCI technique. Namely, first the final captured image is divided by SLM pixel values (each pixel of image is divided by value of corresponding pixel on SLM) to form a high dynamic range image and then the HDR image is tone mapped in order to show the resultant image on 8-bit display (low dynamic range displays). In this work, we used MATLAB for tone mapping.

---

[23] For implemented system the NEP of photodiode is $5.5 \times 10^{-14}\, W/\sqrt{Hz}$, the average responsivity of photodiode is approximately 0.5 and the Bandwidth of system is less than 40KHz. Therefore the maximum noise current equals $5.5 \times 10^{-14}\sqrt{40 \times 10^3} \times 0.5 = 5 \times 10^{-12}\, A$. The gain factors that are used before sampling by ADC are $10^5\, V/A$, $10^6\, V/A$ and $10^7\, V/A$ which result in noise voltages of $0.55\, \mu V$, $5.5\, \mu V$ and $55\, \mu V$. Since the sensitivity of the ADC is $97.6\, \mu V$ at maximum voltage range, the dominant noise is ADC noise at all gain levels.

5.3.2.1. Experiment and Results

The experimental setup (Figure 84) is an active illumination CS single-pixel imaging based system [179]. In active illumination CS single-pixel imaging, the codes are multiplied by the projected light pattern therefore object is illuminated by a pattern with corresponding codes. In other words, codes used for compressive imaging are applied to light source, before object being illuminated. Therefore, a projector can be used to project patterned light and act as the combined light source, lens and SLM. In the setup, a video projector with 1280×800 maximum resolution (Epson® model EB-W7) was used to function as light source, projection lens and SLM. The lens for collecting the reflected light is 8 mm focal length Computar® lens with focus distance ranging from 30 cm to infinity. The detector is a large area (75.4 mm^2 - Ø9.8 mm) silicon photodiode with variable gain amplifier and ADC is a 16 bits data acquisition board with up to 250kS/s (National Instruments™ PCI-6221). The amplified photodetector has an eight-position rotary switch, which allows the user to vary the gain in 10 dB steps.

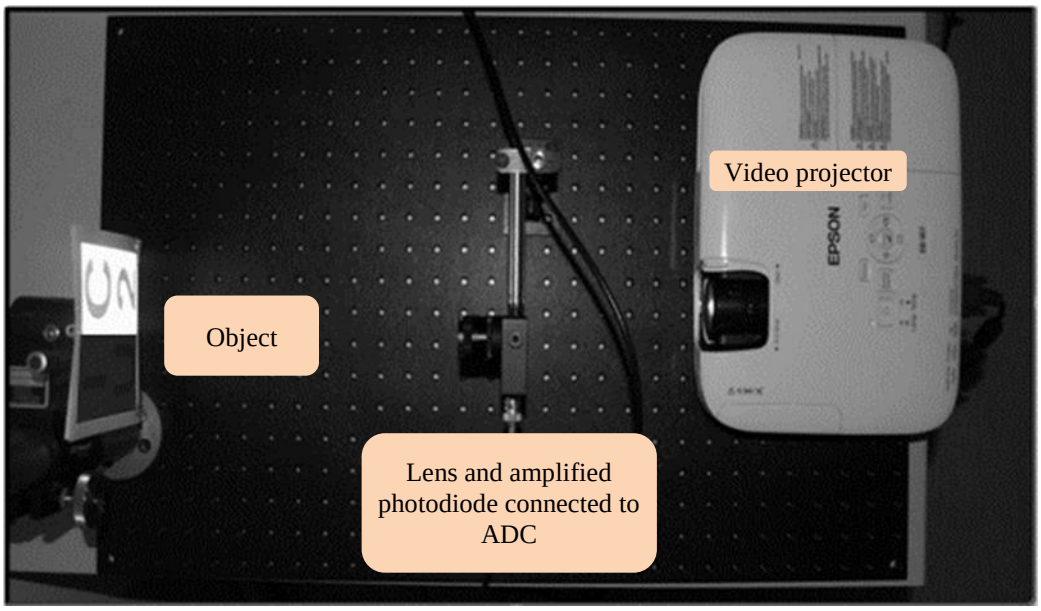

Figure 84: Experimental setup for HDRCI: first method

In these experiments, a synthetic scene was created consisting of some characters printed in black on a piece of white paper (Figure 85). On the left half of the scene, the background was printed with a dark gray tone, mimicking a shadow or a region with reduced illumination, thus causing that portion of the image to have low contrast. Therefore, the benefit of using a high dynamic range imaging system in such a scenario can be demonstrated.

At each step, a code is projected on the object using projector, and the reflected light is collected and amplified using photodetector and digitized using a DAQ board.

The codes that were used for compressive imaging were permuted Hadamard codes which are binary random codes. The reconstruction for compressive imaging was done, by NESTA algorithm [149]. Reconstruction was done using TV minimization option of NESTA algorithm. For each reconstruction, one fourth of samples were used. The number of samples was chosen experimentally; with lower number of samples the quality of reconstructed image degrades; although the characters are recognizable. A

Figure 85: Images acquired with different exposure times demonstrating the difficulty of simultaneously acquiring both halves of the image in a perceptible manner. (a) Left half with black characters on a dark gray background, and (b) right half with black characters on a white background.

comprehensive discussion on theoretical limits of number of samples is provided by Akcakaya and Tarokh [180].

Figure 85 shows some examples to demonstrate how difficult it is to acquire an image of the entire object with high contrast ratio using a conventional camera. Figure 85.a is an image taken with long exposure time, where left side of the object has been properly imaged while the right side is almost saturated. Figure 85.b shows an image taken with short exposure time, where the right side is properly imaged and the left side is too dark and information is lost.

The synthetic scene was imaged to acquire HDR image using compressive imaging technique. Figure 86 shows the results of applying the algorithm after two consecutive reconstructions. Figure 86.a is the first reconstructed image; the right half of the image has higher radiance and therefore it can be visible after reconstruction (similar to Figure 85.b). However, the left side of the image cannot be seen due to poor radiance of the object at this side. Figure 86.b shows the reconstructed image after applying the

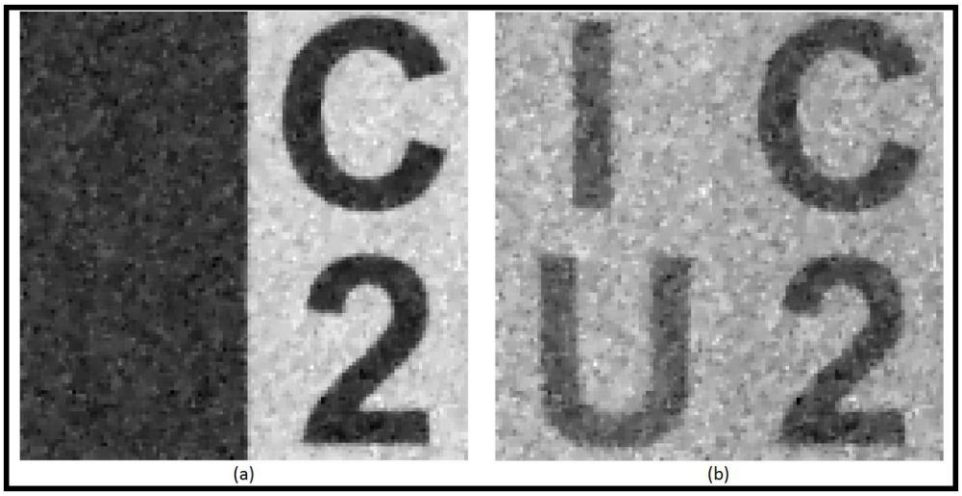

Figure 86: Results of HDRCI: (a) first reconstructed image; (b) second reconstructed image after applying the algorithm.

algorithm; we need to change the illumination pattern in a way to increase the value for pixels on the dark side of the scene (left side of Figure 86.a) and simultaneously avoid saturating the bright side of the scene (right side of Figure 86.a). This is accomplished by multiplying each code with a mask (Figure 87.b) that reduces the radiance of right side of scene by a factor of 3 and increasing the gain of amplifier by a factor of 2. Therefore dynamic range of image will have threefold enhancement compared to image without increasing the dynamic range. As it can be seen in Figure 86.b, the left half of the image is now visible while the right part of the image is not saturated. Therefore, by using the proposed algorithm it is possible to increase the pixel values correspond to regions of the object with very low light level without compromising the quality of the image corresponding to bright regions, hence increasing the dynamic range of the imaging system.

Figure 87 shows the HDR image (Figure 87c) formed from final image (Figure 87a) and mask (Figure 87b). To obtain the HDR image, first, final image is divided by mask values, pixel by pixel; tone mapping then is used in order to display the calculated HDR image in 8-bit format.

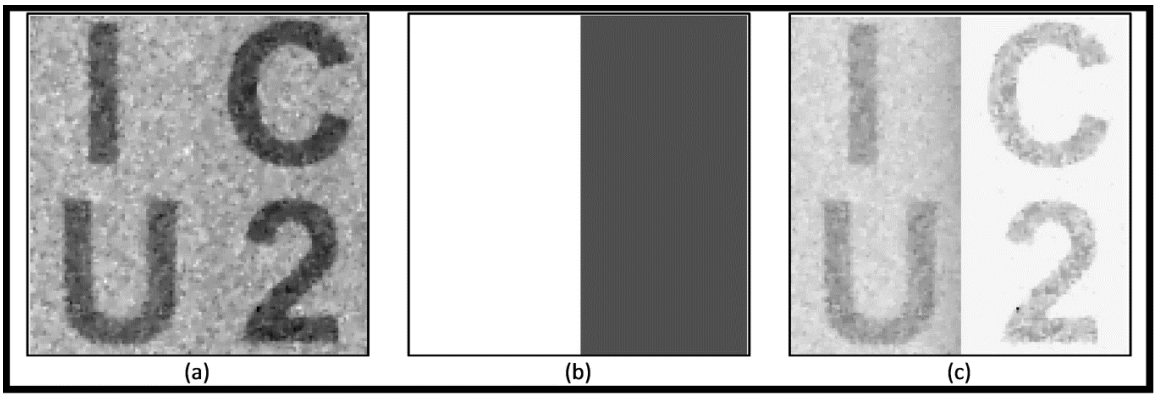

Figure 87: The HDR image obtained by the proposed algorithm : (a) final image (second reconstructed image); (b) mask; (c) HDR image; both bright and dark regions are visible in HDR image.

By increasing the number of iterations a better result could be obtained. But the bottleneck for increasing the dynamic range of the image is the pixel depth (number of bits per pixel) of SLM and the total noise level of the system. Therefore, using a SLM with higher pixel depth and a system with lower noise can improve the performance of HDRCI system.

In our setup, the increase in dynamic range of the image is limited by the dynamic range of projector. Figure 88 shows the intensity range of the projector as projects a series of gray scale images ranges from darkest image (an image with pixel values of 1) to the brightest image (image with pixel values of 255). The dynamic range of projector is about 55, which is about 17dB. Therefore, theoretically, the dynamic range image enhancement can be as high as 17dB by using this setup.

5.3.3. High Dynamic Range Compressive Imaging: Second Method

As mentioned in previous sections, there are two main techniques in HDR imaging. In the first technique, we change the incident radiance of each pixel, independently, using a

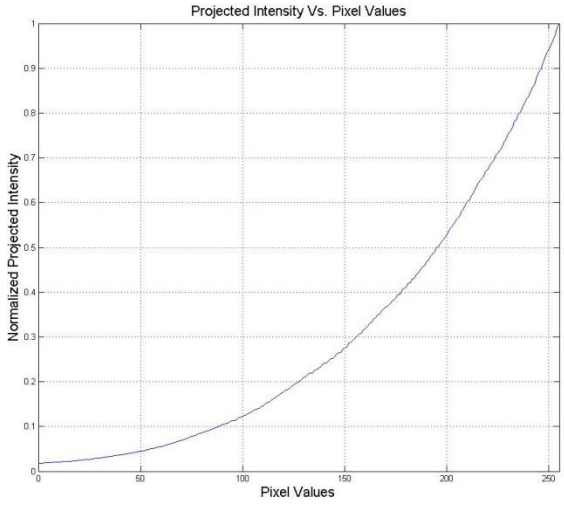

Figure 88: Normalized projected intensity captured by the detector versus the image with pixel values varies from 1 to 255.

spatial light modulator. In the second technique, a series of images with different exposure times are acquired and the HDR image will be constructed using these images.

In previous section we explained the combination of compressive imaging and the former technique of HDR imaging. In this section, combination of compressive imaging and second method for HDR imaging is introduced and demonstrated.

In HDR imaging with different exposure times, a series of images with different exposure time are taken; then the acquired images are combined in order to construct an HDR image [168]. Changing exposure time in compressive imaging technique has different effect from what does in conventional imaging. In compressive imaging, changing the exposure time, does affect all samples and, consequently, all pixels in reconstructed image. Therefore, in compressive sampling method, exposure time cannot be changed as jn conventional imaging and a parameter equivalent to exposure time has to be defined. Equivalent exposure time can be defined as combination of masking some regions/pixels and changing the radiance, the integration time of the single detector (e.g. photo-diode), or the gain of acquisition device. In other words, for changing the exposure time, some regions/pixels are blocked/unblocked and the second parameter, which is radiance from object, integration time of detector, and/or gain of acquisition device, is increased/decreased.

The flowchart of Figure 89 depicts the basic concept of high dynamic range compressive imaging. First, an image is acquired using compressive imaging technique; then regions/pixels with relatively high intensity are identified. Those regions/pixels are the regions/pixels that most likely will be saturated when the equivalent exposure time will be increased and as a result no information can be extracted from those

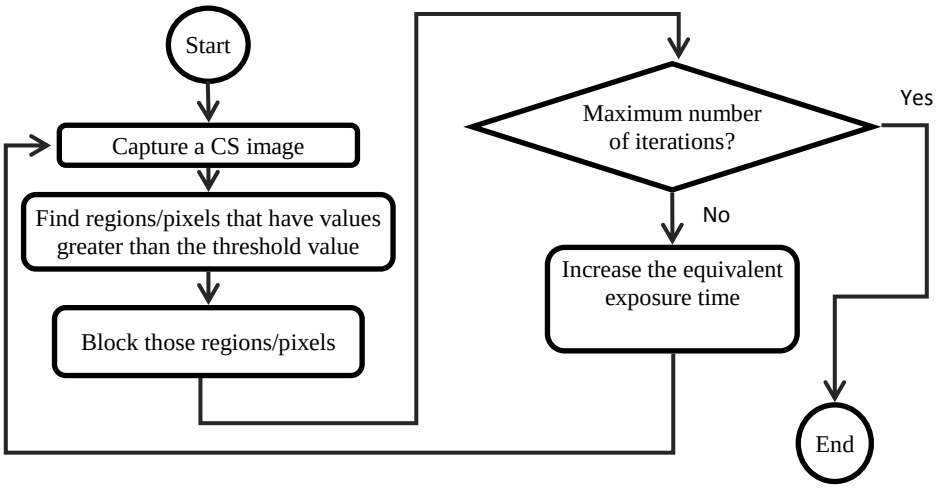

Figure 89: Flowchart of high dynamic range compressive imaging (HDRCI) procedure

regions/pixels. Therefore, if those regions/pixels be blocked, no information will be lost at higher equivalent exposure times. Thus the regions/pixels with relatively high intensity will be identified and a mask corresponding to the identified regions/pixels is created. All the codes for acquiring the next image, via compressive imaging technique, are multiplied with the mask in order to block regions/pixels with high intensity. Since the mask used in this technique is binary, if codes are chosen to be binary too, then combination of the mask and code will be binary. This speeds up the process of imaging for SLM that has only two states and for non-binary codes/masks needs more than one frame per code.

The masked codes are applied with higher equivalent exposure time and next image will be acquired. This procedure is repeated until sufficient images are acquired. Then the acquired images are combined (e.g. using data fusion algorithms) to construct an HDR image.

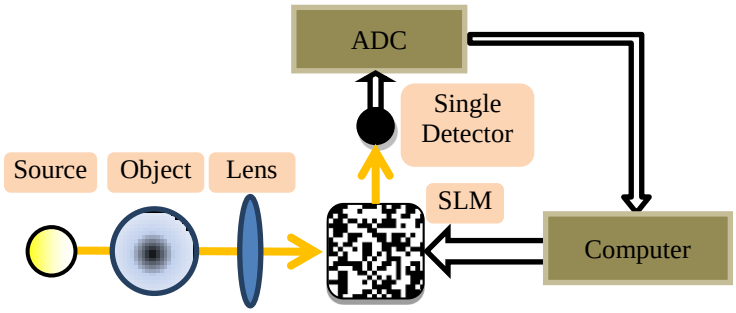

Figure 90: Schematic of the high dynamic range compressive imaging

An HDRCI system brings more pixels above minimum level of intensity and makes them visible (excluding dark pixels of object/scene) compared to a compressive imaging system. Therefore, an HDRCI system increases the dynamic range of the final image.

Figure 90 shows the schematic of the high dynamic range compressive imaging. As it is seen in this figure the system has the same blocks and configuration as the previous one; the object is imaged on the spatial light modulator (SLM). SLM is used to multiply the codes with the imaged object and also serves as mask for HDR imaging part. The reflected light from SLM is captured by a single detector and acquired by an analog to digital convertor (ADC). Both SLM and ADC are controlled and synchronized by the computer.

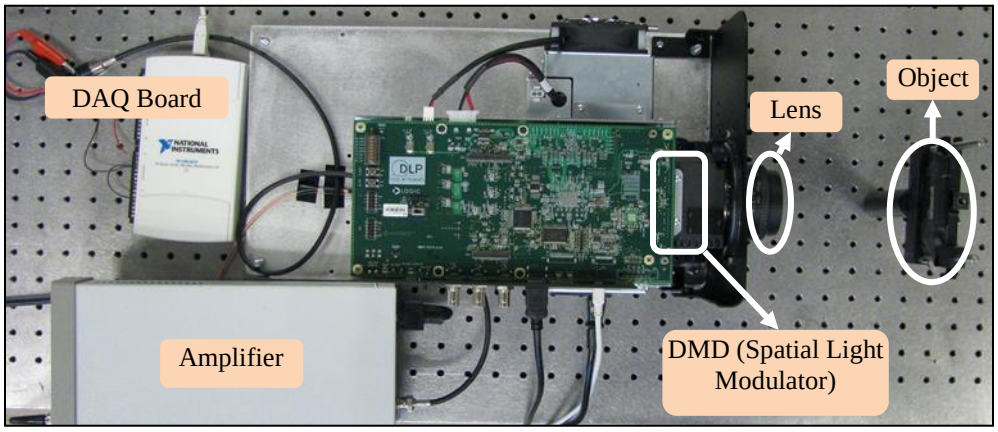

Figure 91: Experimental setup for high dynamic range compressive imaging

5.3.3.1. Experiment and Results

Figure 91 shows the implemented setup for high dynamic range compressive imaging. A DLP LightCommander™ development kit is used as SLM. DLP LightCommander™ development kit is DMD-based and is used for structured light projection. This kit is used in reverse to serve as both SLM in compressive imaging and mask in HDR imaging. The light source of DLP LightCommander™ development kit was removed and a large photodiode (FDS1010 from THORLABS™) is used to capture the light. The output of photodiode is amplified, using PDA220C amplifier from THORLABS™, and sampled using a DAQ board (USB-6210 from National Instrument). A MATLAB™ GUI was developed to control devices, acquire data and reconstruct the image.

Figure 92 shows the object. As it is seen, this object has a bright and a dark region and with conventional imaging a part of image is missed. Therefore we need to use an HDR imaging technique to see both dark and bright parts of the object.

The object was imaged at two different exposure times with compressive imaging technique. Figure 93 shows the reconstructed image at two exposure times. Figure 93.a is

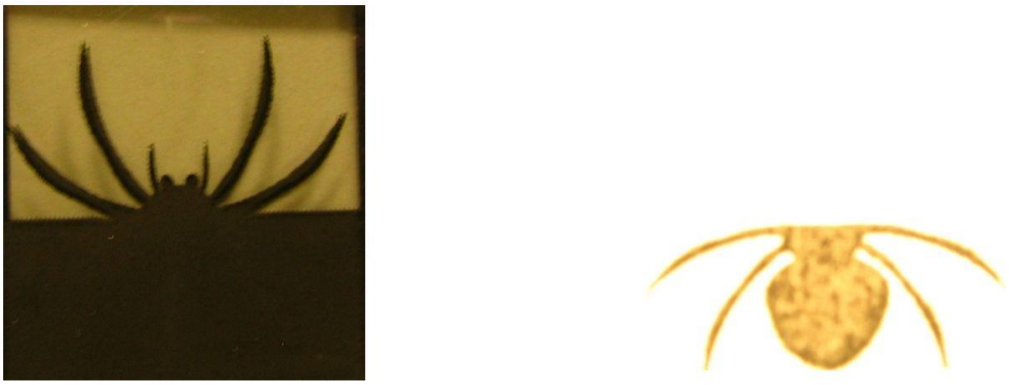

(a) (b)

Figure 92: Image of the object with (a) low exposure time and (b) high exposure time

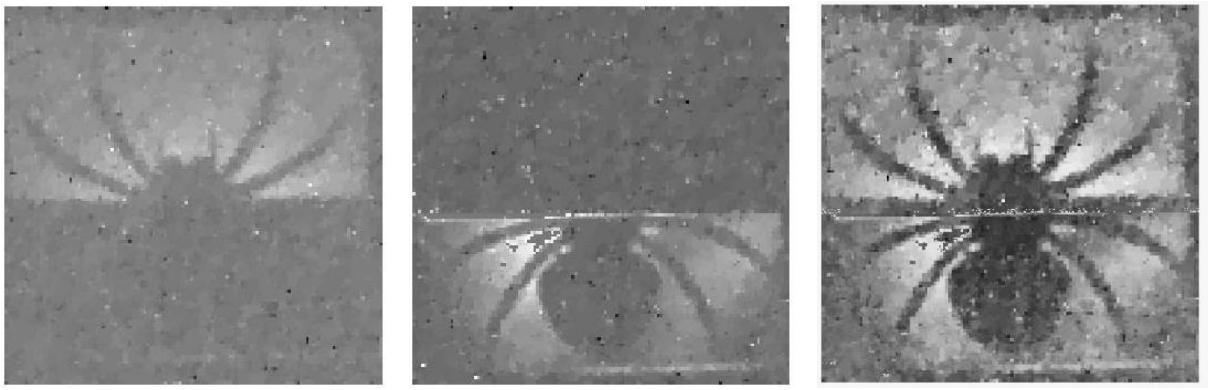

(a) (b) (c)

Figure 93: HDRCI results (a): reconstructed image without any mask. (b): second reconstructed image with a mask on top of the image and increased equivalent exposure time. (c): final image by combining images (a) and (b)

taken when the exposure time is low and therefore the top of the image is visible while the bottom of the image is dark. At the next step we apply a mask that blocks the top part of the object, which is the region with relatively high intensity, and increase the equivalent exposure time by increasing the irradiance and gain of the DAQ board. Figure 93b shows the reconstructed image at this step. As it is shown, the top part of image is almost dark and the details of the lower part of the object are visible.

As mentioned before, to combine images at different equivalent exposure times, one might use a data fusion algorithm. Since, in this special case, we only have two images for two exposure times, we used a simple algorithm to combine the first and the second reconstructed images (by avoiding most dark regions to contribute in final combined image) and calculate the final HDR image. Figure 93c shows the combined HDR image using compressive imaging technique that is rendered using MATLAB^{TM}.

Our experimental result shows that HDRCI system is capable of constructing images with large intensity contrast and can improve the visibility of the image therefore it can be used in applications that require HDR imaging including some biological imaging. To

further improve the quality and dynamic range of the final image the noise level should be decreased and number of different images with different exposure times should be increased.

5.4. Hyperspectral Compressive Imaging

Spectral imaging has application in several fields like remote sensing [181] and food industry [182]. In the spectral imaging, the spectral data of the image forms a cube in which width and height of the cube represent the spatial coordinates and different slides along the depth of the cube represent the content of the object/scene at a specific wavelength. Since the spectral data is usually very huge, the compressive imaging would be a smart solution to reduce the number of the acquired data or speed up the process of acquisition.

Spectral compressive imaging reconstructs the spectral cube from samples of the object/scene acquired in a compressive imaging fashion. There are different architectures that can realize the spectral compressive imaging.

One of the first works in this field has been done by Gehm et.al. [183]. They proposed a single shot spectral compressive imaging based on dispersive elements. Figure 94 shows the schematic of the system; it composed of two 4-f system in a way that the second 4-f system cancel out the dispersion introduced by the first 4-f system. The coding aperture that is put between two 4-f systems and causes that in the plane of coding aperture the spectral and spatial information be mixed. The next 4-f system then transforms the spatial modulation of coding aperture into spatial and spectral modulation while reversing the effect of first 4-f system.

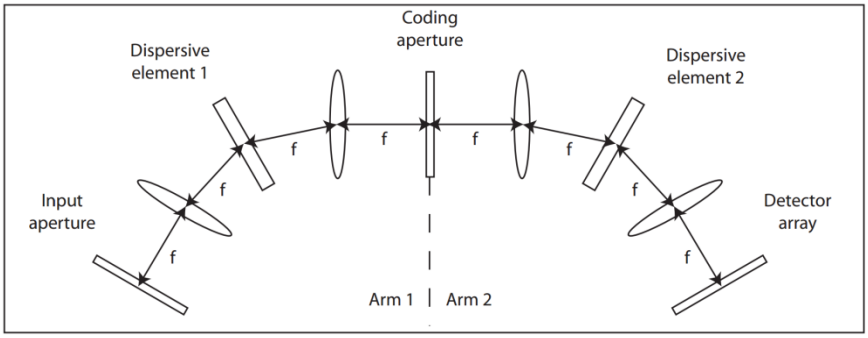

Figure 94: Schematic of dual disperser single shot compressive spectral imager [183]

Another spectral compressive sampling system with one dispersive element was introduces by Wagadarikar et.al. [184]. As it is seen in Figure 95, they have used one dispersive element (instead of two) and a coded aperture before dispersive element. Figure 96 shows the results of their experiment with a scene consisting of a Ping-Pong ball illuminated by a 543 nm green laser and a white light source filtered by a 560 nm narrowband filter; and a red Ping-Pong ball illuminated by a white light source. As it is seen in Figure 96.b the green ball appears in spectral images with lower wavelength where the red ball appears in spectral images with higher wavelengths.

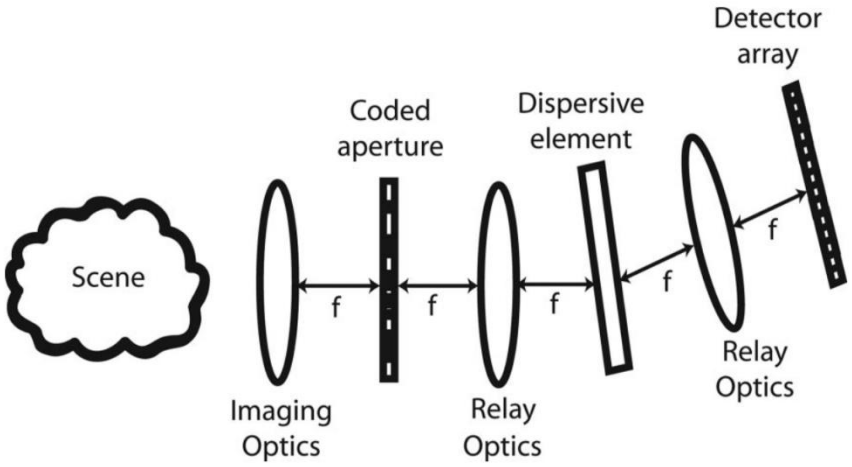

Figure 95: Schematic of single disperser snapshot compressive spectral imager [184]

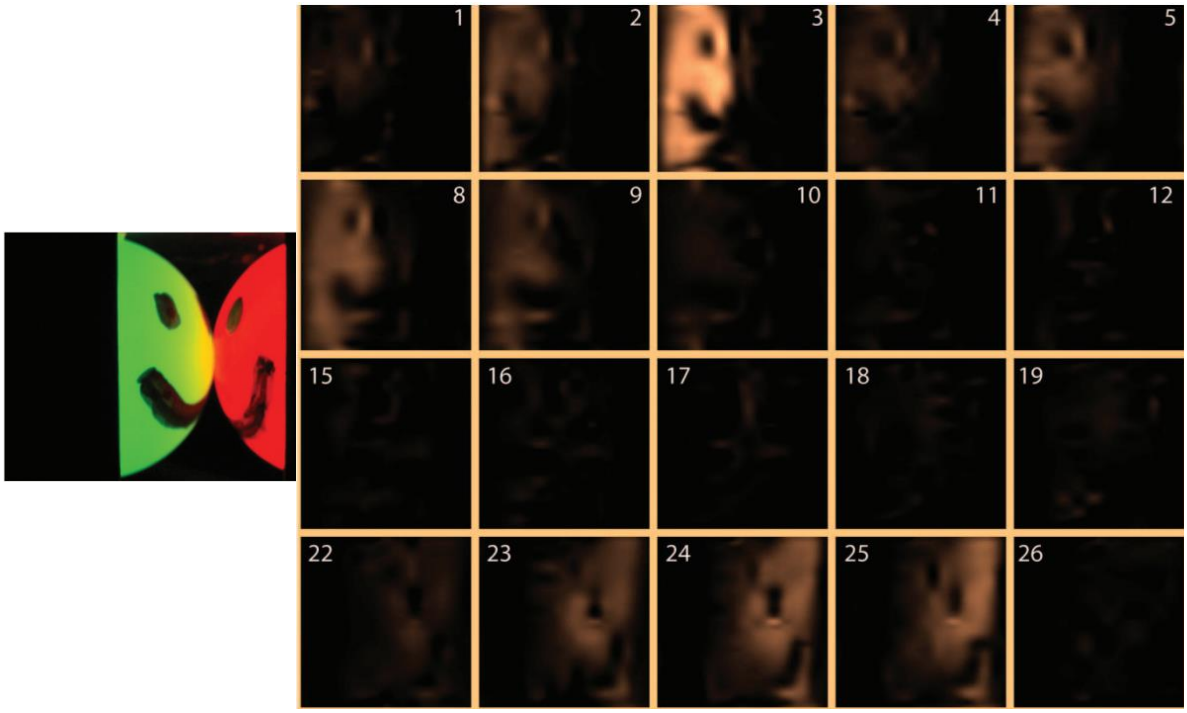

(a) (b)

Figure 96: Results of spectral compressive imaging with the of single disperser snapshot compressive spectral imager (a): scene consisting of a Ping-Pong ball illuminated by a 543 nm green laser and a white light source filtered by a 560 nm narrowband filter; and a red Ping-Pong ball illuminated by a white light source and (b): Spectral images at 28 channels between 540 nm and 640 nm. The green ball appears in the channels with lower wavelengths (3-8) while the red ball appears in the channels with higher wavelengths (23-25) Wagadarikar, John, Willett, & Brady, 2008).

Another approach to spectral compressive imaging is to use a spectrometer instead of a detector in compressive imaging architecture; therefore for each sample, instead of a value that represent the collective intensity in all wavelengths, the spectral content will be acquired. After acquiring enough samples, the data cube will be reconstructed. The data cube can be reconstructed as a whole or one slice for each wavelength at a time. Using this technique, one can reconstruct spectral images with better spectral resolution since the spectral resolution is limited only by resolution of the spectrometer.

Sun and Kelly [185] proposed a compressive sensing hyperspectral imager based on the above idea. They replaced the detector with a spectrometer (QE65000 by Ocean

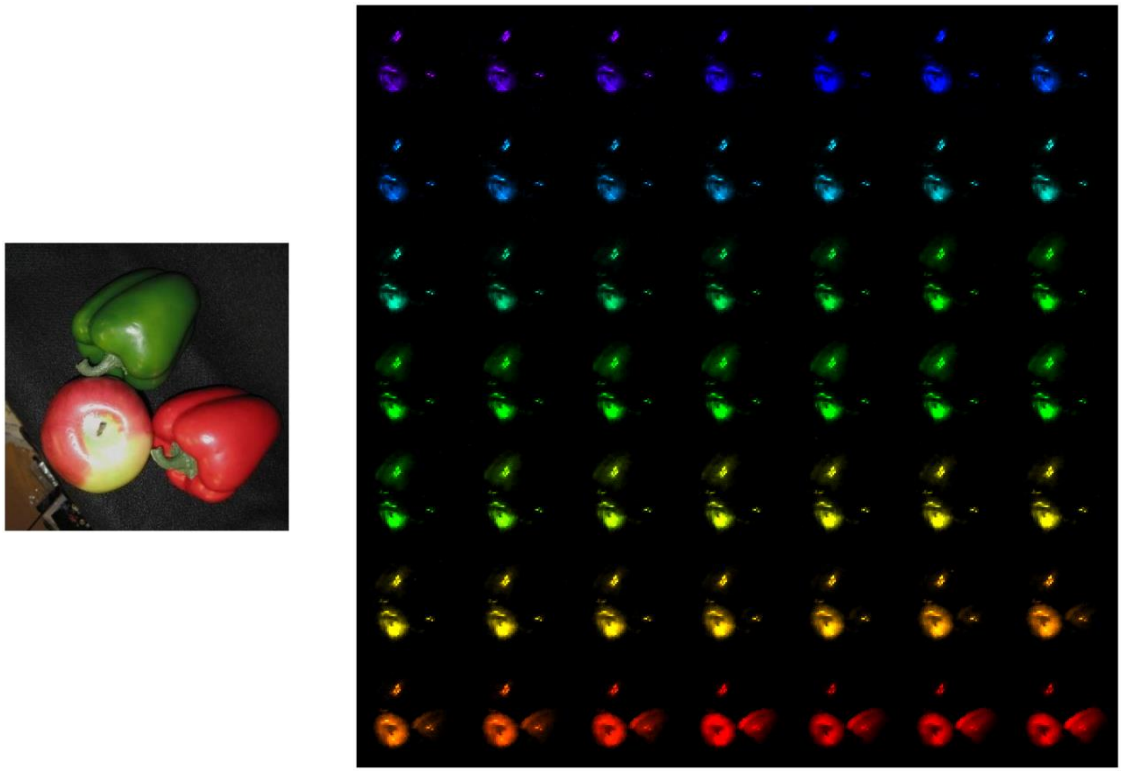

(a) (b)

Figure 97: Results of hyperspectral compressive imager; (a): object and (b): spectral images at wavelength range of 445-640nm.

Optics with a resolution of 0.8 nm) in a compressive imaging system. Figure 97 shows the results of spectral imaging for 49 spectral channels from 445nm to 640nm. The compression ratio is 10 and the spectrum resolution is 4nm.

5.4.1. Experiment

We implemented a spectral compressive imaging system based on the second approach. Figure 98 shows the schematics of the spectral compressive imaging system. A DLP projector was used to implement the SLM for applying the random codes. The DLP projector is Infocus LP120 video projector (Figure 99). We used the DLP projector in reserve; i.e. we gather the light from the object that sits in front of the projector; removed the light source of the projector; and replaced it with a spectrometer. The light reflected

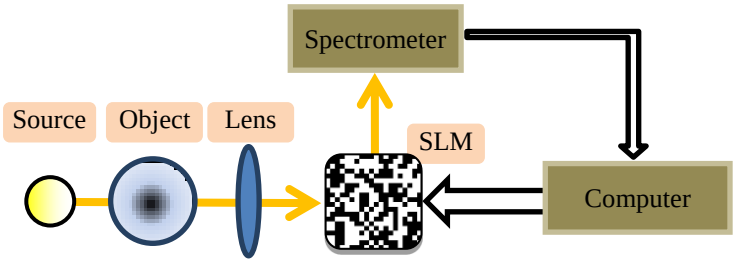

Figure 98: Schematic of Hyperspectral compressive imaging

from object first concentrated using a tapered glass and then is launched into the optical fiber, connected to the spectrometer, using the objective lens. The spectrometer is USB2000+[24] from Ocean Optics with 2048 pixels and range of $200 - 1100$ nm. The tapered glass made from clear fused quartz; the diameter of larger side is 20mm and the diameter of smaller side is 4mm. The objective lens has the magnification of 20x. The data that was acquired from the system had poor signal to noise ratio and therefore we were not able to reconstruct a proper spectral image. The source of the noise includes the

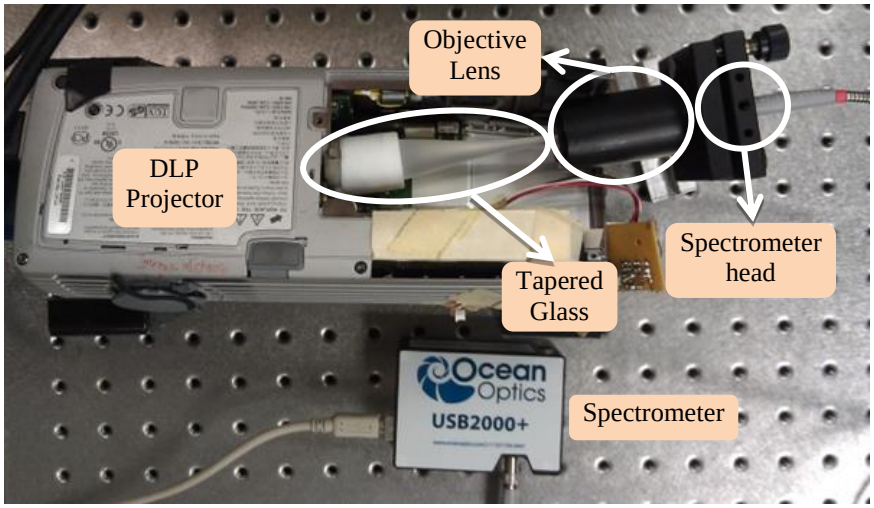

Figure 99: Spectral compressive imaging system. The light source of Infocus LP120 projector was removed and the spectrometer is placed in front of light source. The light enters the spectrometer through a tapered glass, objective lens and an optical fiber.

[24] http://www.oceanoptics.com/products/usb2000+.asp

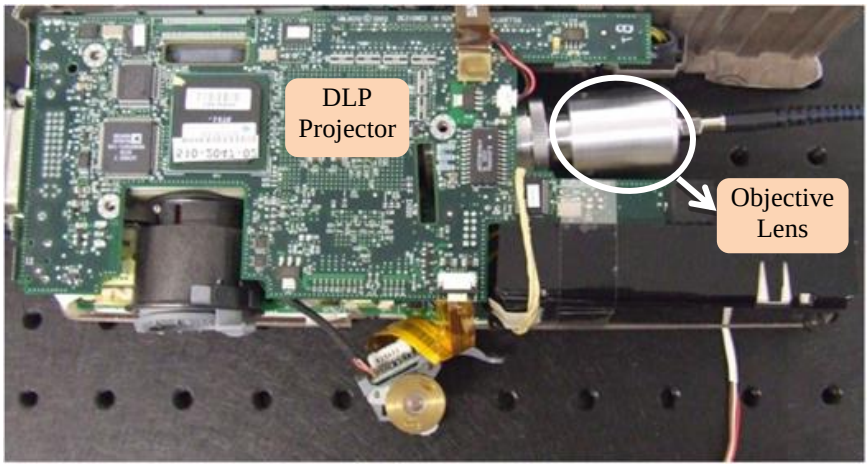

Figure 100: Hyperspectral compressive imaging system with 10x objective lens.

ambient noise (our experiment was conducted in the lab close to electrical room and mechanical room) and noise of spectrometer itself. Therefore the experiment was conducted in our partner lab in Porto University. Figure 100 shows the implemented system. The spectrometer that was used in the experiment is AQ6317B from ANDO with the resolution of 0.01nm.

The scene is a vertical line illuminated by a red HeNe laser (632.8 nm). The scene was sampled compressively; each sample acquired using the spectrometer in wavelength range of 632.61nm to 633.11nm with the steps of 0.01nm. Then the spectral images are reconstructed using NESTA algorithm for each wavelength.

5.4.2. Results

Figure 101 shows the reconstructed spectral images at wavelengths 632.7nm and 632.80nm. As it is seen the laser vertical line appears at 632.80nm and it is not present at spectral image corresponds to the wavelength 632.79nm. The spatial resolution of the images is 64×64 pixels and the spectral resolution is 10pm which is limited by the resolution of the spectrometer.

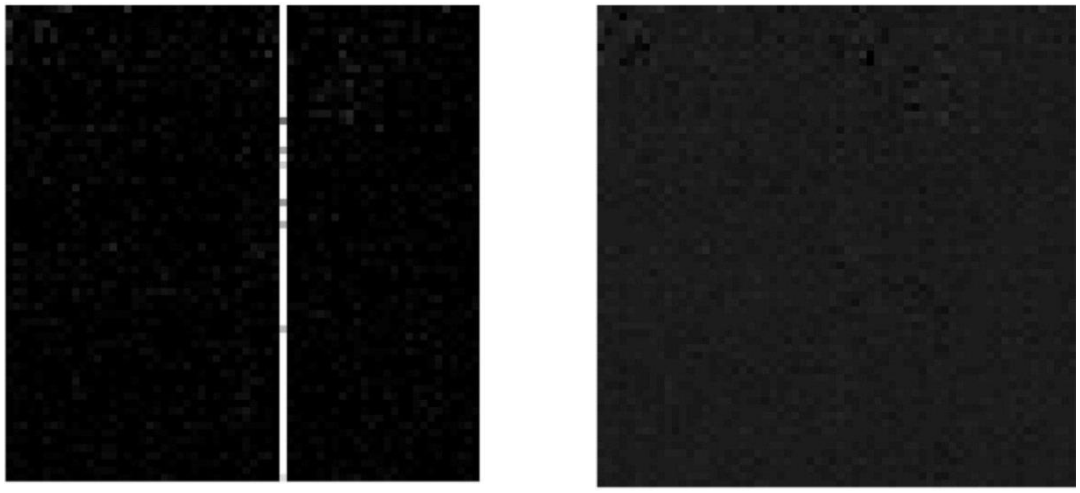

(a) (b)

Figure 101: Spectral images of a at wavelength (a): 632.80nm and (b): 632.79nm

To reconstruct the spectrum of the laser, the data from the pixel corresponds to the laser line was reconstructed and compared to the spectrum of the laser acquired directly with the spectrometer. Figure 102 shows the spectrum of the laser from the spectrometer (red line) and also the reconstructed spectrometer (black line). As it is seen the reconstructed spectrum is consistent with the spectrum acquired by the spectrometer.

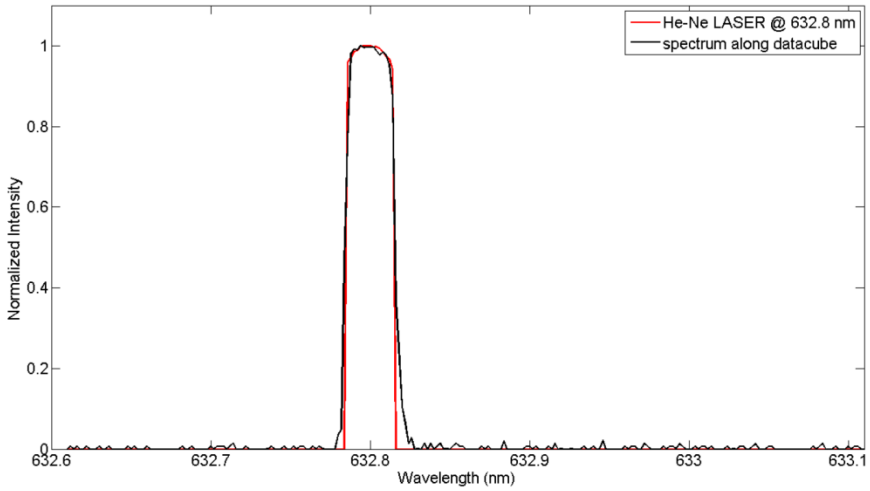

Figure 102: Spectrum of a red HeNe laser (632.8 nm) from the spectrometer (red line) and reconstructed from data cube (black line)

Figure 103.a shows the second scene that has been imaged spectrally. The scene is composed of 15 red LED with central wavelength of 628.1 nm and the bandwidth of 20 nm. To show that the spatial resoltuon can be increased independent of spectral resolution, the spatial resolution was increased to 512×512. Figure 103.b-c show the reconstructed images at 628.10 nm with compression ratio of 80% and 60%. As it is seen the reconstructed images show the red LEDs. The ghost images at reconstructed images are the result of reconstruction algorithm that appear in the reconstructed images.

5.5. Conclusion

In this chapter we presented several compressive imaging systems. Each system is developed is respond to a demand in the field of metrology. The results of the implemented systems are promising and shows that the compressive imaging technique has the capability of overcome some issues and restrictions that we encounter in metrology.

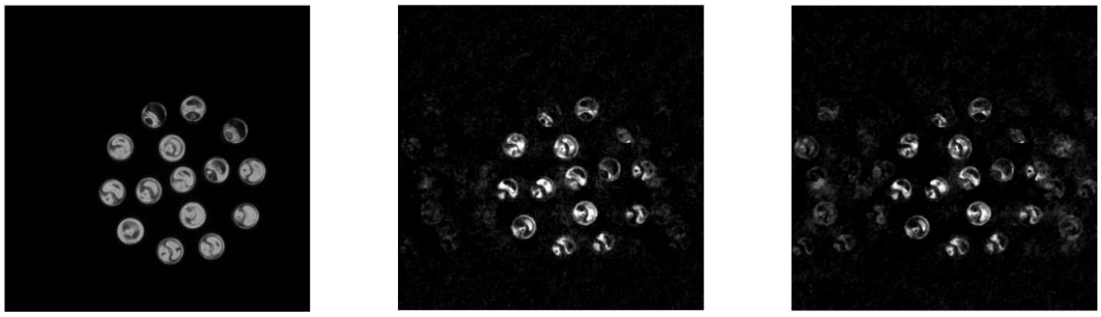

(a) (b) (c)

Figure 103: Hyperspecral compressive imaging of 15 red LEDs with cental wavelength of 628.1 nm and bandwidth of 20 nm. The spatial resolution is 512x512. (a): The scene taken with a conventional camera, (b): the reconstructed spectral image with the compression ratio of 80% and (c): the reconstructed spectral image with the compression ratio of 60% both at 628.10 nm.

The low light compressive imaging system can be used in a situation that the signal to noise ratio is an important factor; using a large and sensitive detector can improve the overall performance of the imaging system.

The transmissive compressive imaging system has the advantage of easy and simple alignment. Since an LCD is used in transmissive compressive imaging system and each LCD is tuned for a specific wavelength, better performance can be achieved in situation that the light source is narrowband and the LCD is tuned for that specific wavelength.

The high dynamic range compressive imaging system is a novel computational imaging system that benefits from the advantages of both compressive imaging and high dynamic range imaging techniques. The architecture of this system is the same as compressive imaging system; the only difference is the ability to change the amplification (either to amplify the light source or the gain of the ADC or detector) and the rest of the change lies on software. High dynamic range compressive imaging system can be used in situations that the scene/object has a wide range of intensity.

Spectral compressive imaging system was the last system that was demonstrated. The spectral compressive imaging system enables us to reduce the number of measurements and speed up the process of measurement. Since most of the natural scenes and object are compressible both in spatial and spectral domains, the data cube of a spectral measurement can be compressed very efficiently. This means that the data cube is very sparse and therefore can be samples in compressive fashion very efficiently.

CHAPTER 6: CONCLUSION AND FUTURE WORK

In this research effort we have tried to address some problems we encountered in the field of metrology. The first issue was the well-known problem of resolution versus dynamic range; there is always a compromise between these two parameters. We have developed a new multi-scale measurement system, which benefits from techniques with different measurement scales. We faced with many challenges along the path of the development of this system, but finally both hardware and software were developed successfully and the system was characterized. Our measurement system includes a fringe projection system which does the coarse measurement (form of the object) and a laser interferometer measuring features of the object. We developed several prototypes and at each step the system was fully characterized and was lessons were used in the design of next prototype. Some optical arrangements of the system were simulated and optimized in Zemax in order to improve the overall system performance.

Both moiré and laser interferometer were simulated with MATLAB and simulated fringe pattern were calculated. We used this simulated fringe patterns to validate and evaluate our proposed algorithm for stitching data from moiré system and laser interferometer.

The core of our algorithm for stitching data is the image registration technique. Our algorithm was implemented in MATLAB and the results showed pixel level resolution for stitching algorithm.

A software to analyze fringe patterns was also developed. Fourier analysis was used for phase wrapping step and quality guided technique was used for phase unwrapping.

An error analysis was performed to characterize the system. The relative error for both moiré and laser interferometer are within 5% of equivalent wavelength for moiré system and 1% of wavelength for laser interferometer at different zoom levels.

There are different paths that can be taken to advance dual moiré laser interferometer system. From the hardware point of view, one can consider combining other measurement instruments and/or combining more than two instruments to further extend the range of measurement and resolution. Another way that can be followed is to improve the resolution of the current hardware (moiré and laser interferometer); this includes using two wavelength laser interferometry, changing the configuration of moiré system (e.g. the angle between camera and projection arms, light source), improving and redesigning the optical elements used in the system and stabilizing the whole system in order to increase the quality of acquired fringe patterns.

The system software could be further improved in the future. Since our focus was not on fringe pattern analysis, we did not explore that thoroughly. One can develop more efficient fringe pattern analysis software; the development and improvement can be done in the pre-processing step (e.g. filtering, smoothing), processing (phase wrapping and phase unwrapping techniques), and/or post-processing. Usually, for each fringe pattern type and signal to noise ratio level, there is one method of phase extraction that gives the best results. Exploring adaptive fringe pattern analysis for different measurement systems with fringe pattern as output would be another topic for future research.

The data stitching algorithm and software could be further improved by exploring the data fusion techniques that suit the data from moiré and laser interferometers. This is the area that can improve the overall performance of the system if the proper data fusion technique is applied.

The compressive imaging systems were the topic of the second part of our research. Compressive imaging is a branch of compressive sampling, which is a novel approach and has been finding plenty of applications in many areas including communication, computer science, biology, etc. Single pixel compressive imaging uses a single detector instead of array of detectors and reconstructs a complete image after several measurements. Using single detector instead of an array of detectors has several benefits including higher signal to noise ratio and capability of imaging in wavelength ranges that there is no camera or array detector; but single detectors are available.

In this field we examined single pixel compressive imaging for different situations including low light imaging, high dynamic range imaging and hyperspectral imaging.

The low light compressive imaging system can be used in situations where the signal to noise ratio is an important factor; using a large and sensitive detector can improve the overall performance of the imaging system.

The transmissive compressive imaging system has the advantage of easy and simple alignment. Since an LCD is used in transmissive compressive imaging system and each LCD is tuned for a specific wavelength, better performance can be achieved in situation that the light source is narrowband and the LCD is tuned for that specific wavelength.

The high dynamic range compressive imaging system is a novel computational imaging system that benefits from the advantages of both compressive imaging and high

dynamic range imaging techniques. The architecture of this system is the same as compressive imaging system; the only difference is the ability to change the amplification (either to amplify the light source or the gain of the ADC or detector) and the rest of the change lies on software. High dynamic range compressive imaging system can be used in situations that the scene/object has a wide range of intensity.

Spectral compressive imaging system was the last system that was demonstrated. The spectral compressive imaging system enables us to reduce the number of measurements and speed up the process of measurement. Since most natural scenes and objects are compressible both in spatial and spectral domains, the data cube of a spectral measurement can be compressed very efficiently. This means that the data cube is very sparse and therefore can be samples in compressive fashion very efficiently.

The compressive imaging techniques are relatively new and growing area of research. One of the topics that can be followed as a future research is the code design for compressive imaging systems. Although there are some codes that can non-adaptively be used in many compressive imaging systems, design of a specific and adaptive codes can improve the performance of the imaging system; as considering the structure of a signal/image can improve the performance of the compressive sampling techniques [186], the design of a code that matches the structure of the image is capable of improving the performance of the compressive imaging system. One other aspect that can be considered in the design of a measurement code for compressive sampling/imaging systems is the average value of each code. Most of the employed codes in compressive sampling/imaging have zero mean value; this means that the values of samples are usually within a very small range and a small amount of measurement noise can corrupt

the reconstructed signal/image quality. Measurement codes with nonzero mean value (e.g. imbalanced number of one and minus one for a binary code, asymmetric probability distribution for non-binary codes) can increase the range of values of the samples and makes it more robust to the measurement noise.

Theoretical analysis of the high dynamic range compressive imaging system is another possible research topic. Analysis of the HDRCI system would give more insight to improving the algorithm and efficiently increasing the dynamic range of the system. A work is being conducted for comparison of different HDRCI systems and specifying the best strategy for each situation. For example, in situation that the speed is an important factor, using a binary mask instead of gray-scale mask can speed up the acquisition process; on the other hand, gray-scale masks result in better quality HDR images in general.

REFERENCES

[1] R. Leach, *Optical Measurement of Surface Topography*, First. Springer-Verlag, 2011.

[2] K. Patorski and M. Kujawinska, *Handbook of the Moiré Fringe Technique*. Elsevier Science, 1993, p. 432.

[3] K. J. Gasvik, *Optical Metrology*, Third. John Wiley & Sons, 2002.

[4] D. Malacara, *Optical Shop Testing*, Third. John Wiley & Sons, 2007, pp. 756–807.

[5] W. H. H. Steel, "Interferometry," Second., Cambridge University Press, 1983, p. 308.

[6] P. Hariharan, *Optical Interferometry, 2e*. Academic Press, 1986.

[7] M. Webster, "Moire." .

[8] C. A. Sciammarella, "The Moiré Method: A Review," *Experimental Mechanics*, vol. 22, no. 11, pp. 418–433, 1982.

[9] C. A. Walker, "A historical review of moiré interferometry," *Experimental Mechanics*, vol. 34, no. 4, pp. 281–299, 1994.

[10] F.-P. Chiang, "Moiré methods of strain analysis," *Experimental Mechanics*, vol. 19, no. 8, pp. 290–308, Aug. 1979.

[11] J. A. N. Buytaert and J. J. J. Dirckx, "Moiré profilometry using liquid crystals for projection and demodulation," *Opt. Express*, vol. 16, no. 1, pp. 179–193, Jan. 2008.

[12] L. H. Jin, Y. Otani, and T. Yoshizawa, "Shadow moiré profilometry by frequency sweeping," *Optical Engineering*, vol. 40, no. 7, p. 1383, 2001.

[13] Y. Y. Hung, C. Y. Liang, J. D. Hovanesian, and A. J. Durelli, "Time-averaged shadow-moiré method for studying vibrations.," *Applied optics*, vol. 16, no. 6, pp. 1717–9, Jun. 1977.

[14] J. J. J. Dirckx, W. F. Decraemer, and J. L. Janssens, "Real-time shadow moire vibration measurement: method featuring simple setup, high sensitivity, and exact calibration," *Applied Optics*, vol. 25, no. 20, p. 3785, Oct. 1986.

[15] K.-S. Chen, C.-C. Chuang, and I.-K. Lin, "Full-field wafer level thin film stress measurement by phase-stepping shadow Moire/spl acute/," *Components and Packaging Technologies, IEEE Transactions on*, vol. 27, no. 3, pp. 594–601, 2004.

[16] P. A. A. Magalhaes Jr, P. S. Neto, and C. S. de Barcellos, “Analysis of Shadow Moire Technique With Phase Shifting Using Generalisation of Carre Method,” *Strain*, vol. 47, pp. e555–e571, Jun. 2011.

[17] H. Takasaki, “Moiré topography.,” *Applied optics*, vol. 12, no. 4, pp. 845–50, Apr. 1973.

[18] L. Pirodda, “Shadow And Projection Moire Techniques For Absolute Or Relative Mapping Of Surface Shapes,” *Optical Engineering*, vol. 21, no. 4, p. 214640, Aug. 1982.

[19] P. Hopstone, A. Katz, and J. Politch, “Infrastructure of time-averaged projection moire fringes in vibration analysis.,” *Applied optics*, vol. 28, no. 24, pp. 5305–11, Dec. 1989.

[20] K. Patorski, M. B. Rafalowski, M. Kujawinska, D. Zawieska, and J. Nowotny, “Computer-aided postural deformity studies using moiré and grid projection methods,” in *International Conference on Interferometry ’94*, 1994, pp. 442–448.

[21] A. Boccaccio, C. Casavola, L. Lamberti, and C. Pappalettere, “Experimental Analysis of Foam Sandwich Panels with Projection Moiré,” in *Proceedings of the 2011 Annual Conference on Experimental and Applied Mechanics*, 2011, pp. 249–256.

[22] F. P. Chiang and C. J. Lin, “Time-average reflection-moiré method for vibration analysis of plates.,” *Applied optics*, vol. 18, no. 9, pp. 1424–7, May 1979.

[23] R. Ritter, “Reflection Moire Methods For Plate Bending Studies,” *Optical Engineering*, vol. 21, no. 4, p. 214663, Aug. 1982.

[24] A. Asundi, “Novel techniques in reflection moiré,” *Experimental Mechanics*, vol. 34, no. 3, pp. 230–242, Sep. 1994.

[25] S. H. Rowe and W. T. Welford, “Surface topography of non-optical surfaces by projected interference fringes,” *Nature*, vol. 216, pp. 786–787, Nov. 1967.

[26] P. S. Huang, “Color-encoded digital fringe projection technique for high-speed three-dimensional surface contouring,” *Optical Engineering*, vol. 38, no. 6, p. 1065, Jun. 1999.

[27] C. Quan, X. Y. He, C. F. Wang, C. J. Tay, and H. M. Shang, “Shape measurement of small objects using LCD fringe projection with phase shifting,” *Optics Communications*, vol. 189, no. 1–3, pp. 21–29, Mar. 2001.

[28] S. Zhang, “Recent progresses on real-time 3D shape measurement using digital fringe projection techniques,” *Optics and Lasers in Engineering*, vol. 48, no. 2, pp. 149–158, Feb. 2010.

[29] T. Young, “The Bakerian Lecture: Experiments and Calculations Relative to Physical Optics,” *Philosophical Transactions of the Royal Society of London*, vol. 94, pp. 1–16, 1804.

[30] A. A. Michelson, “On the Relative Motion of the Earth and the Luminiferous Ether,” *American Journal of Science*, vol. 34, pp. 333–345, 1887.

[31] L. Mandel and E. Wolf, *Optical Coherence and Quantum Optics*. Cambridge University Press, 1995, p. 1192.

[32] E. Wolf, *Introduction to the Theory of Coherence and Polarization of Light*. Cambridge University Press, 2007, p. 236.

[33] T. Li, A. Wang, K. Murphy, and R. Claus, “White-light scanning fiber Michelson interferometer for absolute position-distance measurement,” *Optics Letters*, vol. 20, no. 7, p. 785, Apr. 1995.

[34] K. McKenzie, D. Shaddock, D. McClelland, B. Buchler, and P. Lam, “Experimental Demonstration of a Squeezing-Enhanced Power-Recycled Michelson Interferometer for Gravitational Wave Detection,” *Physical Review Letters*, vol. 88, no. 23, May 2002.

[35] A. Becker, W. Köhler, and B. Müller, “A Scanning Michelson Interferometer for the Measurement of the Concentration and Temperature Derivative of the Refractive Index of Liquids,” *Berichte der Bunsengesellschaft für physikalische Chemie*, vol. 99, no. 4, pp. 600–608, Apr. 1995.

[36] Z. Tian, S. S.-H. Yam, and H.-P. Loock, “Refractive index sensor based on an abrupt taper Michelson interferometer in a single-mode fiber,” *Optics Letters*, vol. 33, no. 10, p. 1105, May 2008.

[37] J. Lawall and E. Kessler, “Michelson interferometry with 10 pm accuracy,” *Review of Scientific Instruments*, vol. 71, no. 7, p. 2669, Jul. 2000.

[38] J. Rard and D. Miller, “The mutual diffusion coefficients of NaCl− H 2 O and CaCl 2− H 2 O at 25° C from Rayleigh interferometry,” *Journal of Solution Chemistry*, 1979.

[39] O. Annunziata, D. Buzatu, and J. Albright, “Protein diffusion coefficients determined by macroscopic-gradient Rayleigh interferometry and dynamic light scattering,” *Langmuir*, 2005.

[40] H. Zhang and O. Annunziata, “Effect of macromolecular polydispersity on diffusion coefficients measured by Rayleigh interferometry.,” *The journal of physical chemistry. B*, vol. 112, no. 12, pp. 3633–43, Mar. 2008.

[41] O. Annunziata and A. Vergara, “Quaternary Diffusion Coefficients in a Protein− Polymer− Salt− Water System Determined by Rayleigh Interferometry,” *The Journal of …*, 2009.

[42] M. I. Lapsley, I.-K. Chiang, Y. B. Zheng, X. Ding, X. Mao, and T. J. Huang, “A single-layer, planar, optofluidic Mach-Zehnder interferometer for label-free detection.,” *Lab on a chip*, vol. 11, no. 10, pp. 1795–800, May 2011.

[43] Z. Qi, N. Matsuda, and K. Itoh, “A design for improving the sensitivity of a Mach–Zehnder interferometer to chemical and biological measurands,” *Sensors and Actuators B: …*, 2002.

[44] B. Sepúlveda and J. del Río, “Optical biosensor microsystems based on the integration of highly sensitive Mach–Zehnder interferometer devices,” *Journal of optics A: …*, 2006.

[45] Z. Tian, S. S. S.-H. Yam, J. Barnes, W. Bock, P. Greig, J. M. Fraser, H.-P. Loock, and R. D. Oleschuk, “Refractive Index Sensing With Mach–Zehnder Interferometer Based on Concatenating Two Single-Mode Fiber Tapers,” *IEEE Photonics Technology Letters*, vol. 20, no. 8, pp. 626–628, Apr. 2008.

[46] J. Blake, P. Tantaswadi, and R. T. de Carvalho, “In-line Sagnac interferometer current sensor,” *IEEE Transactions on Power Delivery*, vol. 11, no. 1, pp. 116–121, 1996.

[47] A. N. Starodumov, L. A. Zenteno, D. Monzon, and E. De La Rosa, “Fiber Sagnac interferometer temperature sensor,” *Applied Physics Letters*, vol. 70, no. 1, p. 19, Jan. 1997.

[48] X. Dong, H. Y. Tam, and P. Shum, “Temperature-insensitive strain sensor with polarization-maintaining photonic crystal fiber based Sagnac interferometer,” *Applied Physics Letters*, vol. 90, no. 15, p. 151113, Apr. 2007.

[49] K.-X. Sun, M. Fejer, E. Gustafson, and R. Byer, “Sagnac Interferometer for Gravitational-Wave Detection,” *Physical Review Letters*, vol. 76, no. 17, pp. 3053–3056, Apr. 1996.

[50] M. Jinno and T. Matsumoto, “Nonlinear Sagnac interferometer switch and its applications,” *IEEE Journal of Quantum Electronics*, vol. 28, no. 4, pp. 875–882, Apr. 1992.

[51] D. A. Jackson, A. Dandridge, and S. K. Sheem, “Measurement of small phase shifts using a single-mode optical-fiber interferometer,” *Optics Letters*, vol. 5, no. 4, p. 139, Apr. 1980.

[52] D. A. Jackson, R. Priest, A. Dandridge, and A. B. Tveten, “Elimination of drift in a single-mode optical fiber interferometer using a piezoelectrically stretched coiled fiber,” *Applied Optics*, vol. 19, no. 17, p. 2926, Sep. 1980.

[53] B. Lee, “Review of the present status of optical fiber sensors,” *Optical Fiber Technology*, vol. 9, no. 2, pp. 57–79, 2003.

[54] F. Ruan, “A precision fiber optic displacement sensor based on reciprocal interferometry,” *Optics Communications*, vol. 176, no. 1–3, pp. 105–112, Mar. 2000.

[55] J. Zhang, J. Yang, W. Sun, W. Jin, L. Yuan, and G. D. Peng, “Composite cavity based fiber optic Fabry–Perot strain sensors demodulated by an unbalanced fiber optic Michelson interferometer with an electrical scanning mirror,” *Measurement Science and Technology*, vol. 19, no. 8, p. 085305, 2008.

[56] L. H. Chen, T. Li, C. C. Chan, R. Menon, P. Balamurali, M. Shaillender, B. Neu, X. M. Ang, P. Zu, W. C. Wong, and K. C. Leong, “Chitosan based fiber-optic Fabry–Perot humidity sensor,” *Sensors and Actuators B: Chemical*, vol. 169, no. null, pp. 167–172, Jul. 2012.

[57] F. Farahi, D. J. Webb, J. D. C. Jones, and D. A. Jackson, “Simultaneous measurement of temperature and strain: cross-sensitivity considerations,” *Journal of Lightwave Technology*, vol. 8, no. 2, pp. 138–142, 1990.

[58] E. Udd, “Review of multi-parameter fiber grating sensors,” *Proceedings of SPIE*, vol. 6770, pp. 677002–677002–10, 2007.

[59] P. O. Varman, “A moiré system for producing numerical data of the profile of a turbine blade using a computer and video store,” *Optics and Lasers in Engineering*, vol. 5, no. 1, pp. 41–58, Jan. 1984.

[60] W. R. J. Funnell, “Image processing applied to the interactive analysis of interferometric fringes,” *Applied Optics*, vol. 20, no. 18, p. 3245, Sep. 1981.

[61] T. YATAGAI, S. INABA, H. NAKANO, and M. SUZUKI, “Automatic flatness tester for very large scale integrated circuit wafers,” *Optical engineering*, vol. 23, no. 4, pp. 401–405.

[62] D. W. Robinson, “Automatic fringe analysis with a computer image-processing system,” *Applied Optics*, vol. 22, no. 14, p. 2169, Jul. 1983.

[63] S. J. Marshall, R. C. Rixon, M. M. Caulfield, and P. M. MacKenzie, “The application of automatic fringe analysis in fracture mechanics,” *Optics and Lasers in Engineering*, vol. 7, no. 3, pp. 175–193, Jan. 1986.

[64] A. Choudry, “Digital holographic interferometry of convective heat transport,” *Applied Optics*, vol. 20, no. 7, p. 1240, Apr. 1981.

[65] H. E. Cline, W. E. Lorensen, and A. S. Holik, “Automatic moire contouring,” *Applied Optics*, vol. 23, no. 10, p. 1454, May 1984.

[66] O. KAFRI and B. ASHKENAZI, “Line thinning algorithm for nearly straight moire fringes,” *Optical engineering*, vol. 25, no. 3, pp. 495–498.

[67] J. Budziński, “SNOP: a method for skeletonization of a fringe pattern along the fringe direction,” *Applied Optics*, vol. 31, no. 16, p. 3109, Jun. 1992.

[68] F. Becker, “Automatic evaluation of interferograms,” National Aeronautics and Space Administration,, Washington, D.C. :, 1982.

[69] M. Takeda and K. Mutoh, “Fourier transform profilometry for the automatic measurement of 3-D object shapes.,” *Applied optics*, vol. 22, no. 24, p. 3977, Dec. 1983.

[70] J. Zhong and J. Weng, “Spatial Carrier-Fringe Pattern Analysis by Means of Wavelet Transform: Wavelet Transform Profilometry,” *Applied Optics*, vol. 43, no. 26, p. 4993, Sep. 2004.

[71] J. Zhong and J. Weng, “Phase retrieval of optical fringe patterns from the ridge of a wavelet transform,” *Optics Letters*, vol. 30, no. 19, p. 2560, Oct. 2005.

[72] M. A. Gdeisat, D. R. Burton, and M. J. Lalor, “Spatial carrier fringe pattern demodulation by use of a two-dimensional continuous wavelet transform,” *Applied Optics*, vol. 45, no. 34, p. 8722, Dec. 2006.

[73] Z. Wang, J. Ma, and M. Vo, “Recent progress in two-dimensional continuous wavelet transform technique for fringe pattern analysis,” *Optics and Lasers in Engineering*, vol. 50, no. 8, pp. 1052–1058, Aug. 2012.

[74] Q. Kemao, “Windowed Fourier transform for fringe pattern analysis: addendum.,” *Applied optics*, vol. 43, no. 17, pp. 3472–3, Jun. 2004.

[75] Q. Kemao, H. Wang, and W. Gao, “Windowed Fourier transform for fringe pattern analysis: theoretical analyses,” *Applied Optics*, vol. 47, no. 29, p. 5408, Oct. 2008.

[76] L. Huang, Q. Kemao, B. Pan, and A. K. Asundi, “Comparison of Fourier transform, windowed Fourier transform, and wavelet transform methods for phase extraction from a single fringe pattern in fringe projection profilometry,” *Optics and Lasers in Engineering*, vol. 48, no. 2, pp. 141–148, Feb. 2010.

[77] K. Itoh, “Analysis of the phase unwrapping algorithm,” *Applied Optics*, vol. 21, no. 14, p. 2470, Jul. 1982.

[78] D. C. Ghiglia and M. D. Pritt, *Two-dimensional phase unwrapping: theory, algorithms, and software*. New York: Wiley, 1998.

[79] M. D. Pritt and J. S. Shipman, "Least-squares two-dimensional phase unwrapping using FFT's," *IEEE Transactions on Geoscience and Remote Sensing*, vol. 32, no. 3, pp. 706–708, May 1994.

[80] M. Pritt, "Phase unwrapping by means of multigrid techniques for interferometric SAR," *Geoscience and Remote Sensing, IEEE Transactions …*, 1996.

[81] D. C. Ghiglia and L. A. Romero, "Minimum L^p-norm two-dimensional phase unwrapping," *Journal of the Optical Society of America A*, vol. 13, no. 10, p. 1999, Oct. 1996.

[82] R. M. Goldstein, H. A. Zebker, and C. L. Werner, "Satellite radar interferometry: Two-dimensional phase unwrapping," *Radio Science*, vol. 23, no. 4, p. 713, 1988.

[83] D. J. Bone, "Fourier fringe analysis: the two-dimensional phase unwrapping problem," *Applied Optics*, vol. 30, no. 25, p. 3627, Sep. 1991.

[84] T. J. Flynn, "Consistent 2-D phase unwrapping guided by a quality map," in *IGARSS '96. 1996 International Geoscience and Remote Sensing Symposium*, 1996, vol. 4, pp. 2057–2059.

[85] J. Strand and T. Taxt, "Performance Evaluation of Two-Dimensional Phase Unwrapping Algorithms," *Applied Optics*, vol. 38, no. 20, p. 4333, Jul. 1999.

[86] Q. Kemao, "Two-dimensional windowed Fourier transform for fringe pattern analysis: Principles, applications and implementations," *Optics and Lasers in Engineering*, vol. 45, no. 2, pp. 304–317, Feb. 2007.

[87] T. R. Crimmins, "Geometric filter for speckle reduction," *Applied Optics*, vol. 24, no. 10, p. 1438, May 1985.

[88] L. Wang, T. Tschudi, T. Halldórsson, and P. R. Pétursson, "Speckle Reduction in Laser Projection Systems by Diffractive Optical Elements," *Applied Optics*, vol. 37, no. 10, p. 1770, Apr. 1998.

[89] M. Bashkansky and J. Reintjes, "Statistics and reduction of speckle in optical coherence tomography," *Optics Letters*, vol. 25, no. 8, p. 545, Apr. 2000.

[90] J. I. Trisnadi, "Speckle contrast reduction in laser projection displays," pp. 131–137, Apr. 2002.

[91] A. A. Goshtasby, *2-D and 3-D Image Registration: for Medical, Remote Sensing, and Industrial Applications*. Wiley-Interscience, 2005.

[92] J. Modersitzki, *Numerical Methods for Image Registration (Numerical Mathematics and Scientific Computation)*. Oxford University Press, USA, 2004, p. 216.

[93] P. Neelin, J. Crossman, D. . Hawkes, Y. Ma, and A. . Evans, "Validation of an mri/pet landmark registration method using 3d simulated pet images and point simulations," *Computerized Medical Imaging and Graphics*, vol. 17, no. 4–5, pp. 351–356, Jul. 1993.

[94] K. Strasters, J. Little, J. Buurman, D. G. Hill, and D. Hawkes, "Anatomical landmark image registration: Validation and comparison," in *CVRMed-MRCAS'97 SE - 17*, 1997, vol. 1205, pp. 161–170.

[95] K. Rohr, H. S. Stiehl, R. Sprengel, T. M. Buzug, J. Weese, and M. H. Kuhn, "Landmark-based elastic registration using approximating thin-plate splines.," *IEEE transactions on medical imaging*, vol. 20, no. 6, pp. 526–34, Jun. 2001.

[96] B. Fischer and J. Modersitzki, "Combination of automatic non-rigid and landmark based registration: the best of both worlds," in *Medical Imaging 2003*, 2003, pp. 1037–1048.

[97] N. M. Alpert, J. F. Bradshaw, D. Kennedy, and J. A. Correia, "The principal axes transformation--a method for image registration.," *Journal of nuclear medicine : official publication, Society of Nuclear Medicine*, vol. 31, no. 10, pp. 1717–22, Oct. 1990.

[98] A. P. Dhawan, L. K. Arata, A. V Levy, and J. Mantil, "Iterative Principal Axes Registration method for analysis of MR-PET brain images.," *IEEE transactions on bio-medical engineering*, vol. 42, no. 11, pp. 1079–87, Nov. 1995.

[99] H. Bülow, L. Dooley, and D. Wermser, "Application of principal axes for registration of NMR image sequences," *Pattern Recognition Letters*, vol. 21, no. 4, pp. 329–336, Apr. 2000.

[100] D. I. Barnea and H. F. Silverman, "A Class of Algorithms for Fast Digital Image Registration," *IEEE Transactions on Computers*, vol. C–21, no. 2, pp. 179–186, Feb. 1972.

[101] L. G. Brown, "A survey of image registration techniques," *ACM Computing Surveys*, vol. 24, no. 4, pp. 325–376, Dec. 1992.

[102] W. M. Wells, P. Viola, H. Atsumi, S. Nakajima, and R. Kikinis, "Multi-modal volume registration by maximization of mutual information," *Medical Image Analysis*, vol. 1, no. 1, pp. 35–51, Mar. 1996.

[103] P. Thévenaz, U. E. Ruttimann, and M. Unser, "A pyramid approach to subpixel registration based on intensity.," *IEEE transactions on image processing : a*

publication of the IEEE Signal Processing Society, vol. 7, no. 1, pp. 27–41, Jan. 1998.

[104] H. J. Johnson and G. E. Christensen, "Consistent landmark and intensity-based image registration.," *IEEE transactions on medical imaging*, vol. 21, no. 5, pp. 450–61, May 2002.

[105] G. K. Rohde, A. Aldroubi, and B. M. Dawant, "The adaptive bases algorithm for intensity-based nonrigid image registration.," *IEEE transactions on medical imaging*, vol. 22, no. 11, pp. 1470–9, Nov. 2003.

[106] F. Maes, A. Collignon, D. Vandermeulen, G. Marchal, and P. Suetens, "Multimodality image registration by maximization of mutual information.," *IEEE transactions on medical imaging*, vol. 16, no. 2, pp. 187–98, Apr. 1997.

[107] J. P. W. Pluim, J. B. A. Maintz, and M. A. Viergever, "Mutual-information-based registration of medical images: a survey.," *IEEE transactions on medical imaging*, vol. 22, no. 8, pp. 986–1004, Aug. 2003.

[108] G. P. Penney, J. Weese, J. A. Little, P. Desmedt, D. L. G. Hill, and D. J. Hawkes, "A comparison of similarity measures for use in 2-D-3-D medical image registration," *IEEE Transactions on Medical Imaging*, vol. 17, pp. 586–595, 1998.

[109] S. Periaswamy and H. Farid, "Medical image registration with partial data.," *Medical image analysis*, vol. 10, no. 3, pp. 452–64, Jun. 2006.

[110] J. Salvi, C. Matabosch, D. Fofi, and J. Forest, "A review of recent range image registration methods with accuracy evaluation," *Image and Vision Computing*, vol. 25, no. 5, pp. 578–596, May 2007.

[111] B. Zitová and J. Flusser, "Image registration methods: a survey," *Image and Vision Computing*, vol. 21, no. 11, pp. 977–1000, Oct. 2003.

[112] D. Purcell, A. Samara, A. Davies, and F. Farahi, "Systematic bias compensation for a moire fringe projection system," in *Optics & Photonics 2005*, 2005, pp. 587909–587909–8.

[113] E. Candès, "Compressive sampling," *Proceedings of the International Congressof Mathematicians, Madrid, Spain*, pp. 1433–1452, 2006.

[114] D. L. Donoho, "Compressed sensing," *IEEE Transactions on Information Theory*, vol. 52, no. 4, pp. 1289–1306, Apr. 2006.

[115] E. J. Candes and M. B. Wakin, "An Introduction To Compressive Sampling," *IEEE Signal Processing Magazine*, vol. 25, no. 2, pp. 21–30, Mar. 2008.

[116] G. Kutyniok, "Theory and Applications of Compressed Sensing," *arXiv:1203.3815v2*, no. July, p. 22, Mar. 2012.

[117] M. Duarte, M. Davenport, D. Takhar, J. Laska, T. Sun, K. Kelly, and R. Baraniuk, "Single-pixel imaging via compressive sampling," *IEEE Signal Processing Magazine*, vol. vol, pp. 25no2pp83–91, 2008.

[118] W. L. Chan, K. Charan, D. Takhar, K. F. Kelly, R. G. Baraniuk, and D. M. Mittleman, "A single-pixel terahertz imaging system based on compressed sensing," *Applied Physics Letters*, vol. 93, no. 12, p. 121105, 2008.

[119] Hong Jung and Jong Chul Ye, "Performance evaluation of accelerated functional MRI acquisition using compressed sensing," in *2009 IEEE International Symposium on Biomedical Imaging: From Nano to Macro*, 2009, pp. 702–705.

[120] C. R. Berger and P. Willett, "Sparse channel estimation for OFDM: Over-complete dictionaries and super-resolution," in *2009 IEEE 10th Workshop on Signal Processing Advances in Wireless Communications*, 2009, pp. 196–200.

[121] H. Zayyani, M. Babaie-Zadeh, and C. Jutten, "Compressed sensing Block MAP-LMS adaptive filter for sparse channel estimation and a Bayesian Cramer-Rao bound," in *2009 IEEE International Workshop on Machine Learning for Signal Processing*, 2009, pp. 1–6.

[122] J. Laska, S. Kirolos, Y. Massoud, R. Baraniuk, A. Gilbert, M. Iwen, and M. Strauss, "Random Sampling for Analog-to-Information Conversion of Wideband Signals," in *2006 IEEE Dallas/CAS Workshop on Design, Applications, Integration and Software*, 2006, pp. 119–122.

[123] J. A. Tropp, J. N. Laska, M. F. Duarte, J. K. Romberg, and R. G. Baraniuk, "Beyond Nyquist: Efficient Sampling of Sparse Bandlimited Signals," *IEEE Transactions on Information Theory*, vol. 56, no. 1, pp. 520–544, Jan. 2010.

[124] W. Dai, M. A. Sheikh, O. Milenkovic, and R. G. Baraniuk, "Compressive sensing DNA microarrays.," *EURASIP journal on bioinformatics & systems biology*, p. 162824, Jan. 2009.

[125] R. Venkataramani and Y. Bresler, "Optimal sub-Nyquist nonuniform sampling and reconstruction for multiband signals," *IEEE Transactions on Signal Processing*, vol. 49, no. 10, pp. 2301–2313, 2001.

[126] T. Ragheb, S. Kirolos, J. Laska, A. Gilbert, M. Strauss, R. Baraniuk, and Y. Massoud, "Implementation models for analog-to-information conversion via random sampling," in *2007 50th Midwest Symposium on Circuits and Systems*, 2007, pp. 325–328.

[127] H. Rauhut, "Random sampling of sparse trigonometric polynomials," *Applied and Computational Harmonic Analysis*, vol. 22, no. 1, pp. 16–42, Jan. 2007.

[128] E. J. Candes, J. Romberg, and T. Tao, "Robust uncertainty principles: Exact signal reconstruction from highly incomplete frequency information," *IEEE Transactions on Information Theory*, vol. 52, no. 2, pp. 489–509, Feb. 2006.

[129] E. Candès and J. Romberg, "Sparsity and incoherence in compressive sampling," *Inverse Problems*, vol. 23, no. 3, pp. 969–985, Jun. 2007.

[130] R. Coifman, F. Geshwind, and Y. Meyer, "Noiselets," *Applied and Computational Harmonic Analysis*, vol. 10, no. 1, pp. 27–44, Jan. 2001.

[131] L. Gan, T. T. Do, and T. D. Tran, "Fast compressive imaging using scrambled block Hadamard ensemble, preprint." 2008.

[132] S. Chen and D. L. Donoho, "Examples of basis pursuit," in *SPIE's 1995 International Symposium on Optical Science, Engineering, and Instrumentation*, 1995, pp. 564–574.

[133] S. S. Chen, D. L. Donoho, and M. a. Saunders, "Atomic Decomposition by Basis Pursuit," *SIAM Journal on Scientific Computing*, vol. 20, no. 1, pp. 33–61, Jan. 1998.

[134] F. Santosa and W. W. Symes, "Inversion of impedance profile from band-limited data," *Digest,International Geoscience and Remote Sensing Symposium*, 1983.

[135] D. L. Donoho and P. B. Stark, "Uncertainty Principles and Signal Recovery," *SIAM Journal on Applied Mathematics*, vol. 49, no. 3, p. 906, Jun. 1989.

[136] D. L. Donoho, "Optimally sparse representation in general (nonorthogonal) dictionaries via ell 1 minimization," *Proceedings of the National Academy of Sciences*, vol. 100, no. 5, pp. 2197–2202, Feb. 2003.

[137] J. A. Tropp, "Recovery of short, complex linear combinations via ℓ1 minimization," *IEEE Transactions on Information Theory*. 15-Apr-2005.

[138] S. Mallat and Z. Zhang, "Matching Pursuit in a time-frequency dictionary," *IEEE Transactions on Signal Processing*, vol. 41, no. {, p. 3415, 1993.

[139] W. Dai and O. Milenkovic, "Subspace Pursuit for Compressive Sensing Signal Reconstruction," *IEEE Transactions on Information Theory*, vol. 55, no. 5, pp. 2230–2249, May 2009.

[140] D. Needell and J. A. Tropp, "CoSaMP: Iterative signal recovery from incomplete and inaccurate samples," *Applied and Computational Harmonic Analysis*, vol. 26, no. 3, pp. 301–321, May 2009.

[141] L. I. Rudin, S. Osher, and E. Fatemi, “Nonlinear total variation based noise removal algorithms,” *Physica D: Nonlinear Phenomena*, vol. 60, no. 1–4, pp. 259–268, Nov. 1992.

[142] E. Candès, “New multiscale transforms, minimum total variation synthesis: applications to edge-preserving image reconstruction,” *Signal Processing*, vol. 82, no. 11, pp. 1519–1543, Nov. 2002.

[143] K. T. Block, M. Uecker, and J. Frahm, “Undersampled radial MRI with multiple coils. Iterative image reconstruction using a total variation constraint.,” *Magnetic resonance in medicine : official journal of the Society of Magnetic Resonance in Medicine / Society of Magnetic Resonance in Medicine*, vol. 57, no. 6, pp. 1086–98, Jun. 2007.

[144] Y. Hu and M. Jacob, “Higher degree total variation (HDTV) regularization for image recovery.,” *IEEE transactions on image processing : a publication of the IEEE Signal Processing Society*, vol. 21, no. 5, pp. 2559–71, May 2012.

[145] R. Chartrand, “Exact Reconstruction of Sparse Signals via Nonconvex Minimization,” *IEEE Signal Processing Letters*, vol. 14, no. 10, pp. 707–710, Oct. 2007.

[146] E. J. Candes and T. Tao, “Decoding by Linear Programming,” *IEEE Transactions on Information Theory*, vol. 51, no. 12, pp. 4203–4215, Dec. 2005.

[147] E. J. Candès, J. K. Romberg, and T. Tao, “Stable signal recovery from incomplete and inaccurate measurements,” *Communications on Pure and Applied Mathematics*, vol. 59, no. 8, pp. 1207–1223, Aug. 2006.

[148] J. Romberg, “Imaging via Compressive Sampling,” *IEEE Signal Processing Magazine*, vol. 25, no. 2, pp. 14–20, Mar. 2008.

[149] S. Becker, J. Bobin, and E. J. Candes, “NESTA: A Fast and Accurate First-Order Method for Sparse Recovery,” *SIAM Journal on Imaging Sciences*, vol. 4, no. 1, p. 1, Apr. 2011.

[150] Y. Nesterov, “Smooth minimization of non-smooth functions,” *Mathematical Programming*, vol. 103, no. 1, pp. 127–152, Dec. 2004.

[151] L. Jacques and P. Vandergheynst, “Compressed Sensing: ‘When Sparsity Meets Sampling’,” in in *Optical and Digital Image Processing: Fundamentals and Applications*, G. Cristobal, P. Schelkens, and H. Thienpont, Eds. Weinheim, Germany: Wiley-VCH Verlag GmbH & Co. KGaA, 2011.

[152] M. Lustig, J. M. Santos, J. Lee, D. L. Donoho, and J. M. Pauly, “Application of compressed sensing for rapid MR imaging,” *IN SPARS*, 2005.

[153] M. Lustig, M. Lustig, D. L. Donoho, and J. M. Pauly, "Rapid MR imaging with Compressed Sensing and randomly under-sampled 3DFT trajectories," *Proc 14th Ann Mtg ISMRM*, 2006.

[154] M. Lustig, D. Donoho, and J. M. Pauly, "Sparse MRI: The application of compressed sensing for rapid MR imaging.," *Magnetic resonance in medicine : official journal of the Society of Magnetic Resonance in Medicine / Society of Magnetic Resonance in Medicine*, vol. 58, no. 6, pp. 1182–95, Dec. 2007.

[155] M. Lustig, D. L. Donoho, J. M. Santos, and J. M. Pauly, "Compressed Sensing MRI," *IEEE Signal Processing Magazine*, vol. 25, no. 2, pp. 72–82, Mar. 2008.

[156] M. B. Wakin, J. N. Laska, M. F. Duarte, D. Baron, S. Sarvotham, D. Takhar, K. F. Kelly, R. G. Baraniuk, and A, "A New Compressive Imaging Camera Architecture using Optical-Domain Compression," in *2006 International Conference on Image Processing*, 2006, vol. 6065, pp. 1273–1276.

[157] R. M. Willett, R. F. Marcia, and J. M. Nichols, "Compressed sensing for practical optical imaging systems: a tutorial," *Optical engineering*, vol. 50, no. 7, 2011.

[158] L. Gan, "Block Compressed Sensing of Natural Images," in *2007 15th International Conference on Digital Signal Processing*, 2007, pp. 403–406.

[159] S. L. Shishkin, "Fast and Robust Compressive Sensing Method Using Mixed Hadamard Sensing Matrix," *IEEE Journal on Emerging and Selected Topics in Circuits and Systems*, vol. 2, no. 3, pp. 353–361, Sep. 2012.

[160] Y. Rivenson and A. Stern, "Compressed Imaging With a Separable Sensing Operator," *IEEE Signal Processing Letters*, vol. 16, no. 6, pp. 449–452, Jun. 2009.

[161] P. Nagesh, "Compressive imaging of color images," in *2009 IEEE International Conference on Acoustics, Speech and Signal Processing*, 2009, pp. 1261–1264.

[162] P. Zerom, K. W. C. Chan, J. C. Howell, and R. Boyd, "Compressive Quantum Ghost Imaging - OSA Technical Digest (CD)," in *International Conference on Quantum Information*, 2011, p. QTuF3.

[163] R. Robucci, J. D. Gray, J. Romberg, and P. Hasler, "Compressive Sensing on a CMOS Separable-Transform Image Sensor," *Proceedings of the IEEE*, vol. 98, no. 6, pp. 1089–1101, Jun. 2010.

[164] P. E. Debevec and J. Malik, "Recovering high dynamic range radiance maps from photographs," in *Proceedings of the 24th annual conference on Computer graphics and interactive techniques - SIGGRAPH '97*, 1997, pp. 369–378.

[165] E. Reinhard, G. Ward, S. Pattanaik, and P. Debevec, "High Dynamic Range Imaging: Acquisition, Display, and Image-Based Lighting," in in *High Dynamic*

Range Imaging: Acquisition, Display, and Image-Based Lighting (The Morgan Kaufmann Series in Computer Graphics), Morgan Kaufmann, 2005, pp. 159–164.

[166] S. K. S. K. Nayar and T. Mitsunaga, "High dynamic range imaging: Spatially varying pixel exposures," in *Proceedings IEEE Conference on Computer Vision and Pattern Recognition. CVPR 2000 (Cat. No.PR00662)*, 2000, vol. 1, pp. 472–479.

[167] S. Mann, "Compositing multiple pictures of the same scene," in *Proceedings of the 46th Annual IS&T Conference*, 1993, pp. 50–52.

[168] M. A. Picard, S. Mann, and R. W. Picard, "On Being `undigital' With Digital Cameras: Extending Dynamic Range By Combining Differently Exposed Pictures," in *PROCEEDINGS OF IS&T*, 1995, pp. 442 – 448.

[169] B. Madden, "Extended Intensity Range Imaging," 1993.

[170] K. Yamada, T. Nakano, S. Yamamoto, E. Akutsu, and I. Aoki, "Wide dynamic range vision sensor for vehicles," in *Proceedings of VNIS'94 - 1994 Vehicle Navigation and Information Systems Conference*, 1994, pp. 405–408.

[171] K. Moriwaki, "Adaptive exposure image input system for obtaining high-quality color information," *Systems and Computers in Japan*, vol. 25, no. 8, pp. 51–60, 1994.

[172] T. Mitsunaga and S. K. Nayar, "Radiometric self calibration," in *Proceedings. 1999 IEEE Computer Society Conference on Computer Vision and Pattern Recognition (Cat. No PR00149)*, 1999, vol. 1, pp. 374–380.

[173] H. Mannami, R. Sagawa, Y. Mukaigawa, T. Echigo, and Y. Yagi, "High Dynamic Range Camera using Reflective Liquid Crystal," in *2007 IEEE 11th International Conference on Computer Vision*, 2007, pp. 1–8.

[174] A. A. Adeyemi, N. Barakat, and T. E. Darcie, "Applications of digital micro-mirror devices to digital optical microscope dynamic range enhancement," *Optics Express*, vol. 17, no. 3, p. 1831, Jan. 2009.

[175] FujiFilm, "http://www.fujifilm.com/products/digital_cameras/f/finepix_f550exr/features/." .

[176] V. Ntziachristos, C. Bremer, and R. Weissleder, "Fluorescence imaging with near-infrared light: new technological advances that enable in vivo molecular imaging.," *European radiology*, vol. 13, no. 1, pp. 195–208, Jan. 2003.

[177] S. K. Nayar, "Computational Cameras: Redefining the Image," *Computer*, vol. 39, no. 8, pp. 30–38, Aug. 2006.

[178] J. N. Laska, P. T. Boufounos, M. A. Davenport, and R. G. Baraniuk, "Democracy in action: Quantization, saturation, and compressive sensing," *Applied and Computational Harmonic Analysis*, vol. 31, no. 3, pp. 429–443, Nov. 2011.

[179] F. Magalhães, F. M. Araújo, M. V. Correia, M. Abolbashari, and F. Farahi, "Active illumination single-pixel camera based on compressive sensing," *Applied Optics*, vol. 50, no. 4, p. 405, Jan. 2011.

[180] M. Akcakaya and V. Tarokh, "Shannon-Theoretic Limits on Noisy Compressive Sampling," *IEEE Transactions on Information Theory*, vol. 56, no. 1, pp. 492–504, Jan. 2010.

[181] G. A. Shaw and H. K. Burke, "Spectral imaging for remote sensing," *Lincoln Laboratory Journal*, vol. 14, no. 1, pp. 3–28, 2003.

[182] M. S. Kim, Y. R. Chen, P. M. Mehl, and others, "Hyperspectral reflectance and fluorescence imaging system for food quality and safety," *TRANSACTIONS-AMERICAN SOCIETY OF AGRICULTURAL ENGINEERS*, vol. 44, no. 3, pp. 721–730, 2001.

[183] M. E. Gehm, R. John, D. J. Brady, R. M. Willett, and T. J. Schulz, "Single-shot compressive spectral imaging with a dual-disperser architecture," *Optics Express*, vol. 15, no. 21, p. 14013, Oct. 2007.

[184] A. Wagadarikar, R. John, R. Willett, and D. Brady, "Single disperser design for coded aperture snapshot spectral imaging," *Applied Optics*, vol. 47, no. 10, p. B44, Feb. 2008.

[185] T. Sun and K. Kelly, "Compressive Sensing Hyperspectral Imager," in *Frontiers in Optics 2009/Laser Science XXV/Fall 2009 OSA Optics & Photonics Technical Digest*, 2009, p. CTuA5.

[186] R. G. Baraniuk, V. Cevher, M. F. Duarte, and C. Hegde, "Model-Based Compressive Sensing," *IEEE Transactions on Information Theory*, vol. 56, no. 4, pp. 1982–2001, Apr. 2010.